University of Glasgow

Zhang, Yong (2026) *Diagnostic of solar eruptive prominences.* PhD thesis.

https://theses.gla.ac.uk/86209/

Copyright and moral rights for this work are retained by the author

A copy can be downloaded for personal non-commercial research or study, without prior permission or charge

This work cannot be reproduced or quoted extensively from without first obtaining permission in writing from the author

The content must not be changed in any way or sold commercially in any format or medium without the formal permission of the author

When referring to this work, full bibliographic details including the author, title, awarding institution and date of the thesis must be given

Enlighten: Theses
https://theses.gla.ac.uk/
research-enlighten@glasgow.ac.uk

Diagnostic of solar eruptive prominences

Yong Zhang

Submitted in fulfilment of the requirements for the
Degree of Doctor of Philosophy

Astronomy and Astrophysics Group
School of Physics and Astronomy
University of Glasgow

February 2025

Abstract

Solar prominences are fundamental structures in solar and heliospheric physics whose complex thermodynamic states and dynamic evolution pose ongoing diagnostic challenges. The emergence of modern imaging and spectroscopic instruments now permits detailed multi-wavelength analyses of prominences, enabling improved constraints on temperature, density, and velocity and offering pathways to link observable signatures with underlying physical parameters.

This work focuses the diagnosis of eruptive prominences by integrating multi-instrument observations with modelling. We address key questions on plasma properties of eruptive prominences through case studies of two major events, employing novel techniques to explore parameter relationships. Using parameter ranges constrained by observations, we generate parameter maps of key parameters, demonstrating a pathway to more robust, quantitative prominence diagnostics.

In Chapter 1, we summarise prominence morphology, typical thermodynamic properties, and magnetic field structure. We outline theoretical aspects of prominence physics and radiative transfer, including the use of 1D non-local thermodynamic equilibrium (NLTE) modelling, and provide a detailed description of the principal observatories and imaging/spectroscopic channels exploited in the thesis (Solar Orbiter, STEREO, GONG).

In Chapter 2, we analyse the 2023 April 15 prominence eruption and introduce a novel method to estimate radial velocity from 2D image sequences. The method is demonstrated using coordinated SPICE, EUI, EUVI and ground-based Hα observations.

In Chapter 3, we use parallel coordinate visualisation to explore how plasma parameters, such as surface temperature, column mass and temperature gradient, influence the integrated intensities of the H Lyman β and Lyman γ lines in the 2023 April 15 prominence eruption event. We also combine the correlation coefficient and the elasticity coefficient, which highlights parameter sensitivities, to helps identify the most important parameters.

In Chapter 4, we introduce and apply a methodology to constraint parameter that combines NLTE modelling with observational constraints to produce spatially resolved parameter maps. Using SPICE full-disc mosaic observations from April 15, 2023 as the input of incident radiation, we construct maps of key parameters and then perform a comprehensive analysis of relations among parameters and spectral lines.

In Chapter 5, we perform an observational case study of the 2022 February 15 prominence

eruption. Using EUI/FSI 304 Å and EUVI-A 171/195 Å imaging, we characterise the morphology and temporal evolution of this prominence during the eruption, and apply filter-ratio techniques to estimate plasma temperatures. We also use parallel coordinate plots to analyse how plasma parameters affect properties of He II 304 Å line. We explore how collisional excitation and scattering play roles in the formation of He II 304 Å line.

In Chapter 6, we summarise the major results of the thesis and outline prospects for future work, including improvements to inversion strategies and the exploitation of forthcoming instrumentation.

Contents

Abstract **i**

Acknowledgements **xi**

Declaration **xii**

1 Introduction **1**

1.1 Description of Solar Prominences 1

1.1.1 Thermodynamic Properties and Plasma Diagnostics 3

1.1.2 Magnetic Field Structure 4

1.1.3 Classification and Morphological Diversity 6

1.1.4 Fine Structures 7

1.1.5 Dynamical behaviour 8

1.1.6 Eruptive Evolution and Associated Phenomena 9

1.1.7 Theoretical Models and Initiation Mechanisms 10

1.1.8 Interrelationship with Flares and Coronal Mass Ejections 10

1.2 Radiative Transfer 12

1.2.1 Basic Principles of Radiative Transfer 12

1.2.2 Statistical Equilibrium 13

1.2.3 Frequency Redistribution 15

1.2.4 Diagnostic Methods for Optically Thin Plasmas 15

1.2.5 The PRODOP Radiative Transfer Code 16

1.3 Instrumentation 18

1.3.1 Solar Orbiter 18

1.3.2 Solar Terrestrial Relations Observatory 20

1.3.3 GONG Hα Telescope 20

1.4 Concluding Remarks 20

2 Analysis of Lyman β and Lyman γ Lines **22**

2.1 Observations 24

2.1.1 Instrumentation 24

2.1.2 Observation . . . 25
2.1.3 Integrated Intensity . . . 29
2.1.4 Line Width . . . 34
2.1.5 Line Profile . . . 38
2.1.6 Fitting of Line Profile . . . 41
2.2 Radial velocity estimation . . . 43
2.2.1 Direction of the eruption . . . 43
2.2.2 Projection on 2D plane . . . 46
2.2.3 Calculation of radial velocity . . . 47
2.3 Concluding Remarks . . . 48

3 Non-LTE Analysis of Lyman β and Lyman γ Lines 50
3.1 Observations . . . 52
3.1.1 Instruments . . . 52
3.1.2 Observations . . . 53
3.2 Modelling . . . 53
3.2.1 Incident radiation . . . 54
3.2.2 Toolkit to interpret model results . . . 59
3.3 Results . . . 67
3.3.1 The Lyman β line . . . 70
3.3.2 The Lyman γ line . . . 71
3.3.3 Constraining parameters using SPICE data . . . 71
3.4 Discussion . . . 74
3.5 Concluding Remarks . . . 75

4 Prominence Plasma Parameters Maps 77
4.1 Observations . . . 80
4.2 Prominence model atmosphere . . . 80
4.3 Parameter maps . . . 89
4.4 Concluding Remarks . . . 92

5 Prominence parameters and He II 304 emission 94
5.1 Observations . . . 95
5.2 Filter-ratio analysis . . . 97
5.3 Results . . . 100
5.3.1 Intensity change of 304 Å line with altitude . . . 100
5.3.2 Analysis of parameters' effect by parallel coordinate plots . . . 104
5.3.3 Discussion . . . 108
5.4 Concluding Remarks . . . 112

6 Conclusions **114**

List of Tables

2.1 Summary of SPICE observational parameters in this study (pre-eruption vs. eruption) 25
2.2 Mean integrated intensities and mean line widths of the Lyman β and Lyman γ lines measured in the disc and prominence regions before and during the eruption. 31

3.1 Parameter ranges for different variables 69
3.2 Correlation and elasticity coefficients for Lyman β line properties 69
3.3 Correlation and elasticity coefficients for Lyman γ line properties 69

4.1 The parameter ranges for different variables. 82
4.2 Ranges of parameter maps provided by the best coefficient set 90

5.1 The observed intensity ratios of 195 Å/171 Å filters for five features along the eruptive prominence. 99
5.2 The parameter ranges for different variables. 103
5.3 The reference model parameters. 104
5.4 Correlation coefficients for He II 304 Å line properties 106

List of Figures

1.1 Filaments and prominences observed in Hα 2
1.2 SOHO/SUMER images of the 5 September 1996, prominence. 4
1.3 Schematic representations of general magnetic field of filament channels and the direction of magnetic field related to the chirality of filaments 5
1.4 A well formed bright coronal helmet streamer 6
1.5 A group of tornado-like prominences observed in the 171 Å 9
1.6 Dual-Filament CME initiation model 11
1.7 1D prominence slab vertically standing above the solar surface 13
1.8 The schematic of 1D prominence slab model 16
1.9 The full disc image of the Sun with the prominence eruption observed on 15 February 2022, by EUI/FSI 304 Å (Figure from Zhang et al (2026d, submitted)). 19

2.1 The positions of different spacecraft. 24
2.2 The SPICE observation of the integrated intensity of the Lyman β and Lyman γ lines taken from 07:03 - 08:09 UT, 15 April 2023. 26
2.3 The prominence at 05:52:57 UT, 15 April 2023, observed by EUI/HRI$_{\mathrm{EUV}}$ 17.4 nm 26
2.4 The LW channel observation of SPICE during pre-eruption phase at 07:37:39 UT 27
2.5 The spectrum of the LW channel during pre-eruption phase at the green cross and the red cross in Figure 2.2 27
2.6 Hα image of El Teide at 10:07 UT 28
2.7 The SPICE observation of the integrated intensity of the Lyman β from 08:13 - 11:58 UT, 15 April 2023. 28
2.8 The integrated intensity along the blue cut (x=5) and the green dashed cut (x=25) for Lyman β and Lyman γ lines during pre-eruption phase 29
2.9 The ratio of the integrated intensity of Lyman β and Lyman γ lines along the blue cut (x=5, left) and the green dashed cut (x=25, right) during pre-eruption phase (Figure from Zhang et al. (2026a)). 30
2.10 The integrated intensity along the blue cut in Figure 2.7 for Lyman β during eruption phase. 30

2.11 The average profiles of Lyman β and Lyman γ lines of Prominence Region during pre-eruption phase along the green dashed cut 34
2.12 The average profiles of Lyman β in the prominence region along the blue cuts during the pre-eruption phase and eruption phase. The shaded regions show the estimated profile uncertainties estimated by the standard deviation of the corona region intensity, while the dashed lines and horizontal lines indicate the line widths defined between CDF=0.12 and CDF=0.88. 35
2.13 The method of line width calculation 35
2.14 The line width of Lyman β and Lyman γ lines profiles during pre-eruption phase (Figure from Zhang et al. (2026a)). 39
2.15 The line width of Lyman β lines profiles during eruption phase 39
2.16 The Lyman β and Lyman γ lines spectra before the eruption from image of the detector for the exposures at the raster position x=5, 10, 15, 20, 25 during pre-eruption phase. 40
2.17 The Lyman β lines spectra during eruption from image of the detector for the exposures at the raster position x=80, 82, 84, 86, 88 during eruption phase. . . . 41
2.18 The Lyman β and Lyman γ lines profiles in the prominence region from SPICE observation before the eruption. 42
2.19 The Lyman β lines profiles in the prominence region from SPICE observation during the eruption. 43
2.20 The double Gaussian fitting of the He II line and the the Lyman β line. 44
2.21 The illustration of the coordinates and angles (Figure from Zhang et al. (2026a)) 45
2.22 Two cross-sections of the sphere. 45
2.23 Hα image of El Teide at 09:57 UT (left) and 10:17 UT (right), April 15, 2023. . 46
2.24 19.5 nm observation of EUVI-A at 10:05 UT (left) and 10:10 UT (right), April 15, 2023. 48

3.1 The SPICE observation of the integrated intensity of the Lyman β and Lyman γ lines 52
3.2 Centre-to-limb variation of the Lyman β intensity 55
3.3 Geometric configuration of the observed solar region. 56
3.4 The solar map of the integrated intensity of the H-Lyman β line by SPICE full disc mosaic observation on Nov 13-14, 2023 (Figure from Zhang et al. (2026b)). 58
3.5 The incident Lyman β line profile 59
3.6 The parallel coordinate plot of 4 parameters with the integrated intensity of the Hα line. 60
3.7 Integrated intensity vs. emission measure, temperature, pressure and slab thickness for the Hα line. 60

3.8 The parallel coordinate plot of 6 parameters with the integrated intensity of the Lyman β line (Figure from Zhang et al. (2026b)). 61
3.9 The parallel coordinate plot of 6 parameters with the collisional term εB_{ν_0} of the Lyman β line (Figure from Zhang et al. (2026b)). 61
3.10 The parallel coordinate plot of 6 parameters with the radiation term $(1-\varepsilon)\bar{J}$ of the Lyman β line (Figure from Zhang et al. (2026b)). 62
3.11 The parallel coordinate plot of 6 parameters with the optical thickness of the Lyman β line (Figure from Zhang et al. (2026b)). 62
3.12 The parallel coordinate plot of 6 parameters with the integrated intensity of the Lyman γ line (Figure from Zhang et al. (2026b)). 63
3.13 The parallel coordinate plot of 6 parameters with the collisional term εB_{ν_0} of the Lyman γ line (Figure from Zhang et al. (2026b)). 63
3.14 The parallel coordinate plot of 6 parameters with the radiation term $(1-\varepsilon)\bar{J}$ of the Lyman γ line (Figure from Zhang et al. (2026b)). 64
3.15 The parallel coordinate plot of 6 parameters with the optical thickness of the Lyman γ line (Figure from Zhang et al. (2026b)). 64
3.16 The probability distribution of the central pressure constrained by observation (Figure from Zhang et al. (2026b)). 72
3.17 The probability distribution of the central temperature constrained by observation (Figure from Zhang et al. (2026b)). 72
3.18 The probability distribution of the Lyman β line optical thickness constrained by observation (Figure from Zhang et al. (2026b)). 73
3.19 The probability distribution of the Lyman γ line optical thickness constrained by observation (Figure from Zhang et al. (2026b)). 73

4.1 The process to construct initial set of prominence models that are close to observations of the Lyman β and Lyman γ lines (Figure from Zhang et al (2026c, submitted)). 81
4.2 The 9-pixel intensity map of the Lyman β and the Lyman γ line in the prominence region 81
4.3 Comparison of best matched intensity map and observation for the red box region in Figure 3.1. 83
4.4 Temperature profiles of Model A and Model B and contribution functions of Model A for the Lyman β line and Model B for the Lyman γ line. 86
4.5 The lower-right panel of Figure 4.4 showing the details of the changes in the temperature profile (Figure from Zhang et al (2026c, submitted)). 88
4.6 The comparison of calculated intensity by the best coefficient set and observation for the red box region in Figure 3.1. 90

4.7 Parameter maps for the most important parameters in the Lyman β and Lyman γ line formation (Figure from Zhang et al (2026c, submitted)). 90
4.8 The electron density map and Hα intensity map as examples of other maps we can produce (Figure from Zhang et al (2026c, submitted)). 92

5.1 The full disc image of the Sun with the prominence eruption observed on February 15, 2022, using EUI/FSI 304 Åchannel (Figure from Zhang et al. (2026d, submitted)). 96
5.2 The prominence observed by EUVI-A in the 171 Å and 195 Å channels. 97
5.3 Left panel: The STEREO EUVI-A temperature response functions for the 171 Å, 195 Å and 284 Å channels. They are calculated using the effective area from SSW and the CHIANTI atomic database version 11.0.2. Right panel: The ratio of temperature response functions for the EUVI 195 Å and 171 Å channels. The two red dashed lines are the minimum and maximum ratios in Table 5.1 (Figure from Zhang et al. (2026d, submitted)). 99
5.4 Evolution of the prominence eruption as seen by FSI at 304 Å showing the two features being tracked (Figure from Zhang et al. (2026d, submitted)). 100
5.5 An example of the tracked feature in FSI 304 Å at 22:00 UT, Feb 15th, 2022. . 101
5.6 The change in the relative intensity for features 1 and 2 with altitude and points correspond to 200 random models. 103
5.7 The parallel coordinate plot of 6 parameters with the integrated intensity of 304 Å line (Figure from Zhang et al. (2026d, submitted)). 105
5.8 The parallel coordinate plot of 6 parameters with the optical thickness of 304 Å line (Figure from Zhang et al. (2026d, submitted)). 106
5.9 An example of the contribution function of 304 Å line along the slab. 107
5.10 An example of the source function of 304 Å line along the slab. 107
5.11 The parallel coordinate plot of 6 parameters with the collisional term of 304 Å line (Figure from Zhang et al. (2026d, submitted)). 108
5.12 The parallel coordinate plot of 6 parameters with the radiative term of 304 Å line (Figure from Zhang et al. (2026d, submitted)). 109
5.13 Integrated intensity of the He II 304 Å line as a function of radial velocity for 26 models. In this test, all model parameters were fixed to the median values of their adopted ranges, except for the radial velocity, which was varied from 0 to 2500 km s^{-1}. (Figure from Zhang et al. (2026d, submitted)). 111

Acknowledgements

I really enjoy the 4 years PhD life in Glasgow. It is an important goal for me to study abroad since my childhood. During these 4 years, I experience lives in UK and other European countries, which helps me understand more about the world and different cultures. I do research happily with my supervisor, Nicolas Labrosse, who is erudite and kind. We have many interesting discoveries these years, like the parallel coordinate plot and parameter maps, but those ideas usually are not fully shaped at the beginning. Nicolas would always give opinions to improve our methods and make results more understandable to readers. Therefore, my final papers are always much better original ones. I also thank Susanna Parenti and Therese Ann Kucera. They provided the valuable data of the first dedicated observation of an off-limb prominence, which is the foundation of 3 papers of mine. Their comments and good insights about SPICE observations help me a lot. I also thank Lyndsay Fletcher for her comments on some of my papers.

Moreover, I need to thank my girl friend, Tingting Sun, who is sunny and kind. I can feel our strong connections even we have a distance with thousands of miles. Daily video calls make me no longer feel lonely even I study abroad. As a former student in Physics, Tingting Sun and I got Master degrees at the same year but she is no longer doing research. It is still good to see that she can understand my research outcomes to some extent. I like the time to share my research with her.

The road of scientific research never stops. I will continue my research in China. Thanks for Professor Yang Wang, who is my supervisor during my Master degree study, his useful information and advices have let me find a post-doc fellowship successfully in Peking University. I have never been to the Peking University before but it is my dream university once upon a time. I believe I will also have a good experience there.

I also thank to Patrick Antolin, Declan Andrew Diver, and Craig Stark. Their comments during the viva improved the thesis a lot.

Declaration

With the exception of chapter 1 , which contains introductory material, all work in this thesis was carried out by the author unless otherwise explicitly stated.

Chapter 1

Introduction

1.1 Description of Solar Prominences

Solar prominences play an important role in the study of solar physics, with origins tracing back to the early observations of total solar eclipses. The work of J. Janssen and Sir Norman Lockyer in the late 19th century established the spectroscopic nature of these structures, identifying the dominant Hα emission at 6562.8 Å(Janssens, 1970; Lockyer, 1931). This breakthrough enabled systematic observation outside eclipses, a capability significantly advanced by Hale's invention of the spectrohelioscope in the 1920s (Hale, 1929). The fundamental equivalence between the bright limb features (prominences) and their dark counterparts observed against the solar disc (filaments) was subsequently recognized, establishing the dual nomenclature that persists in modern literature. In Figure 1.1, we can see observations of a prominence and a filament.

The advent of space-based observatories, particularly the *Solar and Heliospheric Observatory (SOHO)*, *Hinode*, *Solar Terrestrial Relations Observatory (STEREO)*, *Interface Region Imaging Spectrograph (IRIS)* and the *Solar Dynamics Observatory (SDO)*, has revolutionized prominence research by providing continuous, multi-wavelength observations. These have been complemented by ground-based facilities such as the Swedish Solar Telescope (SST), Daniel K. Inouye Solar Telescope (DKIST), Vacuum Tower Telescope (VTT), and radioheliographs including the Siberian Solar Radio Telescope (SSRT) and Nobeyama Radioheliograph (NoRH). This observational synergy has transformed our understanding from viewing prominences as static and cool features to recognizing them as complex, magnetically dominated plasma systems exhibiting intricate fine structure and rich dynamics (Vial, 2014). The present section aims to provide a comprehensive description of solar prominences, synthesizing insights from these diverse observational platforms to explain their thermodynamic properties, magnetic environment, structural characteristics, dynamical behaviour, and evolution during eruption.

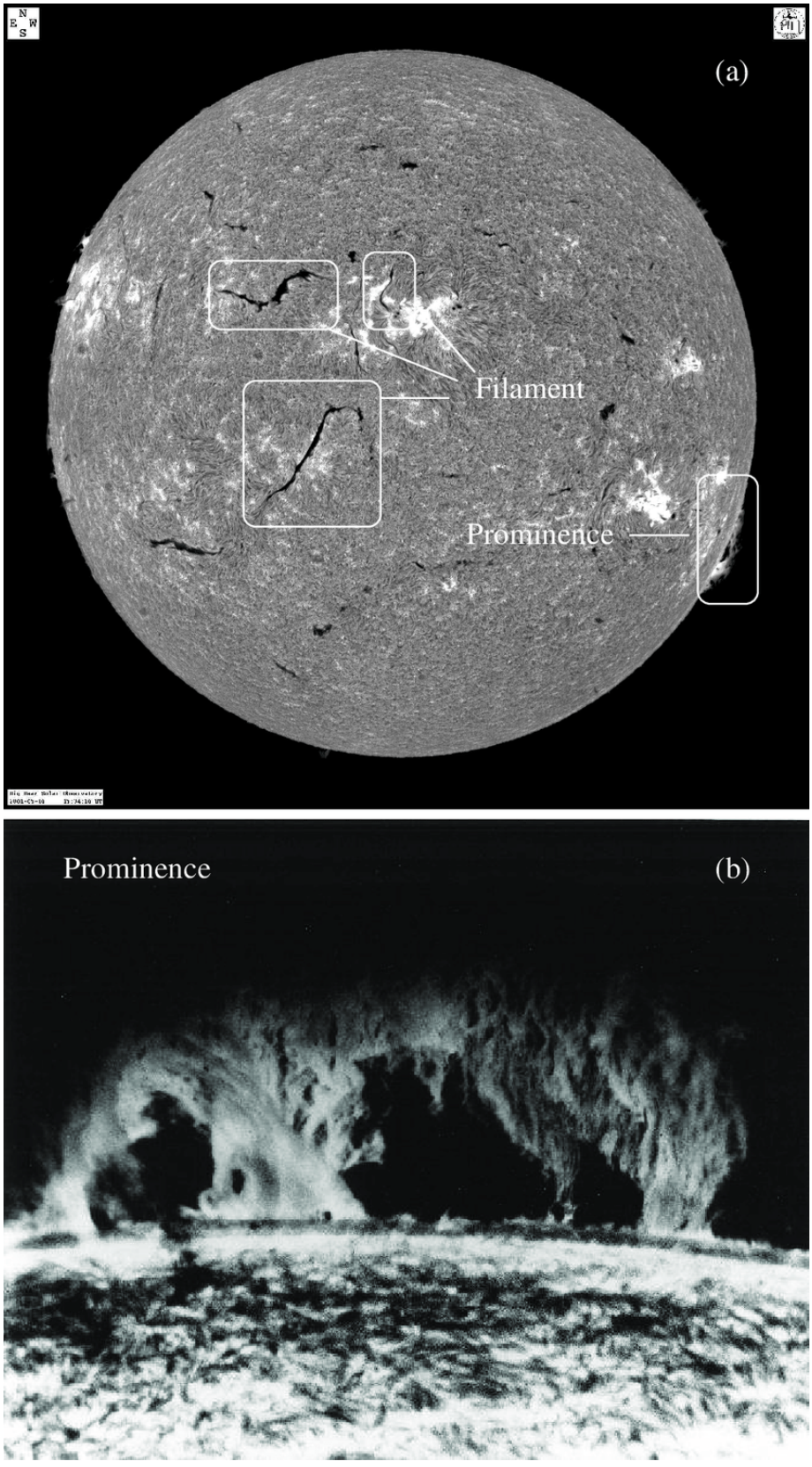

Figure 1.1: Filaments and prominences observed in Hα by Big Bear Solar Observatory (BBSO) (Fig.1-4 in Su (2007)).

1.1.1 Thermodynamic Properties and Plasma Diagnostics

Solar prominences represent one of the most extreme thermal contrasts in astrophysical plasmas, characterized by cool ($T \approx 5,000$–$10,000$ K), dense ($n_e \approx 10^{10}$–10^{11} cm^{-3}) material embedded within the million-degree solar corona. This configuration implies density and temperature contrasts of approximately two orders of magnitude. The plasma pressure within prominences ranges from 0.1 to 1 dyn cm^{-2}, achieving equilibrium through a balance with magnetic pressure forces (Engvold, 2014). The formation of this cool and dense material is commonly associated with thermal instability, in which enhanced radiative losses lead to catastrophic cooling and condensation of coronal plasma along magnetic field lines (Xia et al., 2011). This process provides an important mechanism for supplying prominence material, especially in magnetic dips where the condensed plasma can accumulate and remain supported.

Understanding the thermodynamic properties of prominences requires a multi-wavelength diagnostic approach, as their structure consists of a cool core embedded within a hotter prominence-corona transition region (PCTR) (Parenti, 2014a). The cool core is diagnosed using optically thick lines like Hα and the hydrogen Lyman continuum to derive parameters such as temperature, density, and ionization degree (Hirayama, 1985; Parenti, 2014a). In contrast, the PCTR is best observed via its optically thin extreme-ultraviolet (EUV) emission lines. By analysing a large set of these lines, as demonstrated in the spectral atlas by Parenti and Vial (2007), one can derive the differential emission measure (DEM) to quantify the distribution of plasma as a function of temperature.

In addition to the diagnostic techniques applied to the prominence core and PCTR, the interaction of prominences with coronal radiation provides another valuable probe of their physical properties. When observed against the solar limb, prominences can appear dark in coronal EUV lines and soft X-rays due to two distinct mechanisms: absorption of background coronal emission by hydrogen and helium continua, and emissivity blocking, where the cool prominence plasma occupies a volume that would otherwise emit coronal radiation (Anzer et al., 2007). By combining observations of the same prominence in spectral lines with different opacities, for instance, by using an EUV line below the H I Lyman limit (e.g., Mg X 625 Å) where absorption is significant, and another above it (e.g., Fe XII 1242 Å) where only blocking operates, one can disentangle these effects and derive optical thickness of the structure (Anzer et al., 2007). In Figure 1.2, we can see that there is a significant lowering of brightness at the location of the prominence in the upper panels.

Multi-frequency radio observations have also proven particularly valuable for diagnosing the thermal state of prominence plasma. The analysis by Grechnev et al. (2006), utilizing simultaneous data from SSRT (5.7 GHz) and NoRH (17 and 34 GHz), demonstrated that the dominant emission mechanism from the cool core is thermal bremsstrahlung. For typical quiescent filaments, the optical depth $\tau \gg 1$ at these frequencies, meaning the observed brightness temperature T_b provides a direct measure of the kinetic temperature T. Their study of three erup-

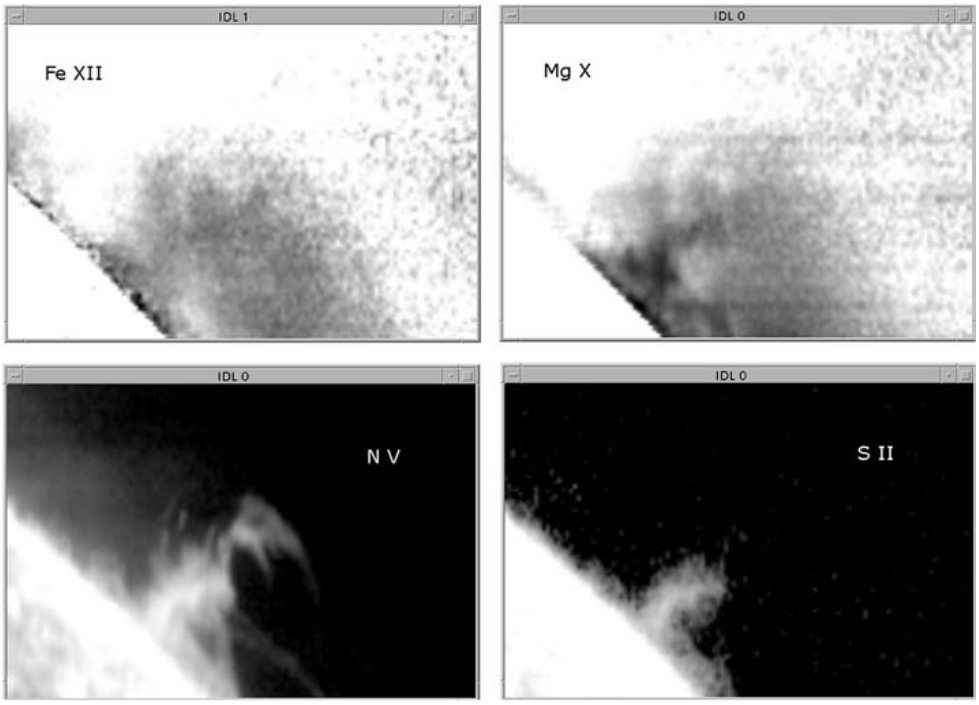

Figure 1.2: SOHO/SUMER images of the 5 September 1996, prominence. The rasters in four lines of Fe XII (1242 Å), Mg X (624 Å), N V (1238 Å), and S II (1250 Å) are shown. (Figure 1 in Anzer et al. (2007)).

tive events consistently revealed brightness temperatures in the range 5000–7000 K, providing compelling evidence that the main body of erupting prominences undergoes no significant heating during the initial phases of eruption. This finding has profound implications for models of coronal mass ejection (CME) initiation and energy transport.

1.1.2 Magnetic Field Structure

The magnetic field structure is a fundamental element of solar prominences, governing their formation, stability, and ultimate eruption. Direct measurements via the Zeeman and Hanlé effects reveal field strengths typically ranging from 3 to 30 G in quiescent prominences (Leroy, 1989), with active region prominences often exhibiting stronger fields. The corresponding plasma β (ratio of gas to magnetic pressure) falls within the range 0.01 to 1, implying magnetic forces as the dominant part in prominence support and confinement.

Prominences exhibit a precise topological relationship with the underlying photospheric magnetic field, forming above polarity inversion lines (PILs) that show boundaries between regions of opposite magnetic polarity. The larger scale magnetic environment is characterized by the filament channel, an elongated corridor in the chromosphere and low corona where the magnetic field is mainly horizontal and aligned parallel to the PIL (Gaizauskas, 1998). Observational signatures of this configuration include the systematic alignment of chromospheric fibrils along the channel and their anti-parallel streaming on either side of the PIL, reflecting the

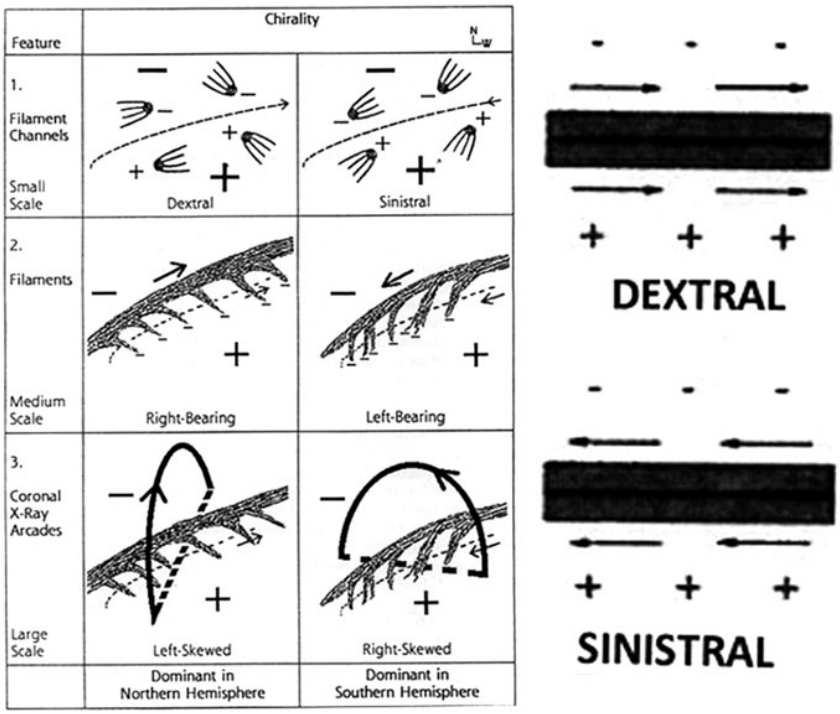

Figure 1.3: The left panel is schematic representations of general magnetic field of filament channels (Figure 1 in Martin (1998)). The right panel shows the direction of magnetic field related to the chirality of a dextral and a sinistral filament (Figure 5 in Mackay et al. (2010)).

presence of magnetic shear (Smith, 1968; Foukal, 1971).

A fundamental property of filament channels is their chirality, or magnetic handedness. As shown in Figure 1.3, a channel is classified as dextral if, when viewed from the positive polarity side, the axial magnetic field points to the right; it is sinistral if it points left (Mackay et al., 2010). This schematic description mainly refers to the axial component of the field. In reality, filament magnetic fields are not purely axial, but are generally sheared or twisted, which can provide magnetic dips and support for the cool prominence plasma. This chirality manifests consistently across spatial scales, from the pattern of chromospheric fibrils to the orientation of the filament spine and its barbs. The observation of a strong hemispheric pattern (with dextral channels always dominating the northern hemisphere and sinistral channels always dominating the southern hemisphere) provides crucial evidence linking prominence formation to global solar processes, likely involving the influence of Coriolis forces on emerging magnetic flux or large-scale photospheric flows (Martin, 1998).

The coronal volume surrounding many prominences, particularly quiescent ones, often exhibits reduced emission in white-light and EUV observations, forming structures known as coronal cavities (Fuller et al., 2008). These tunnel-like features extend along the filament channel and typically form the base of helmet streamers which necessarily consist of oppositely directed magnetic fields. Figure 1.4 shows a bright helmet streamer extended from the northeast limb and a low density cavity with the helmet base. Spectroscopic observations indicate that cavities

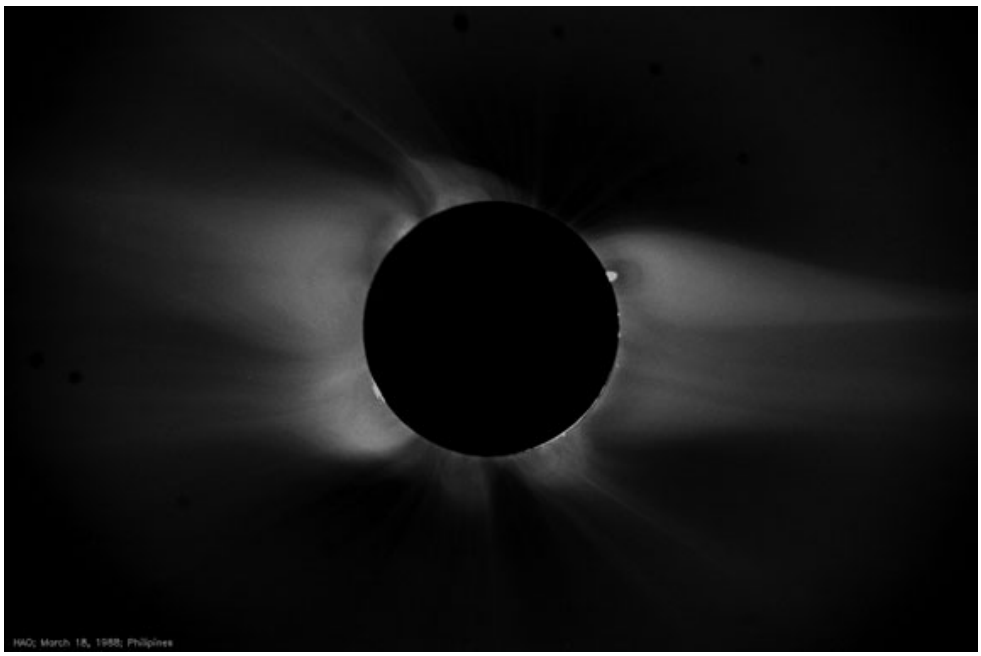

Figure 1.4: A well formed bright coronal helmet streamer extended from the northeast limb (Fig.2.7. in (Engvold, 2014)). There is a low density cavity at the helmet base.

are not vacuous but contain plasma at coronal temperatures ($\sim$ 1.6 MK) with densities approximately 30% lower than the surrounding streamer (Dudík et al., 2012; Fuller et al., 2008). The detection of large-scale swirling motions within cavities supports the interpretation that they represent the manifestation of a helically twisted magnetic flux rope enveloping the prominence (Okamoto et al., 2010; Habbal et al., 2010; Liu et al., 2012a; Kucera et al., 2012). Thus, the cavity embodies the coronal volume occupied by the prominence's magnetic support system, offering critical insights into the three-dimensional magnetic topology.

1.1.3 Classification and Morphological Diversity

The morphological and dynamical diversity of solar prominences has inspired numerous classification schemes throughout the history of solar physics. Early systems, such as those proposed by Secchi and Pettit, were predominantly descriptive, cataloguing shapes like "hedgerows", "trees", and "suspended clouds" (Pettit, 1932).Subsequent schemes by Menzel and Evans, de Jager, and Zirin introduced classifications based on apparent flow patterns, location, and association with solar activity (Menzel and Evans, 1953; De Jager, 2012; Zirin, 1966, 1988).

Quiescent prominences represent the most stable and long-lived class, with characteristic lifetimes ranging from several days to months. These structures typically form in high-latitude filament channels, often within the polar crown that migrates in response to the solar cycle. They are distinguished by their large spatial scales, often extending hundreds of megameters in length and reaching heights of 30–50 Mm. Their classic "hedgerow" morphology consists of multiple vertical, palisade-like structures with well-developed lateral extensions known as barbs.

Active region prominences, in contrast, are intimately associated with sunspot groups and the intense magnetic fields of active regions. They exhibit shorter lifetimes (hours to days), simpler morphologies characterized by thin, straight spines with minimal barb development, and higher levels of small-scale dynamics. Their evolution is tightly coupled to the rapidly changing magnetic configuration of the active region.

Intermediate prominences occupy the magnetic interface between active regions and the quiet Sun, or form within decaying active region complexes. They display hybrid characteristics, often combining the long, slender spine of an active region prominence with the more developed barb structure typical of quiescent prominences. Their lifetimes and activity levels are correspondingly intermediate between the other two classes (Engvold, 2014).

Beyond the three schemes, there are also some phenomena which are close to prominences. Coronal cloud prominences, also known as "coronal spiders" or "funnel prominences," represent large volumes of cool material suspended high in the corona without an obvious association with PILs (Liu et al., 2012b). Their formation is thought to result from in-situ radiative cooling instabilities. Coronal rain refers to the downward streaming of cool, condensed plasma along curved trajectories, commonly observed in active region loops as a consequence of thermal non-equilibrium (Schrijver, 2001).

An alternative classification framework proposed by Tang (1987) and expanded by Mackay et al. (2008) focuses on the relationship between the filament and underlying photospheric magnetic flux distribution. This scheme distinguishes between filaments forming above internal PILs within single bipoles, those forming on external PILs between separate bipoles, hybrid forms spanning both internal and external PILs, and those forming in diffuse, decayed magnetic flux. This approach directly links classification to the magnetic origins of the filament channel, providing valuable insights into formation mechanisms.

1.1.4 Fine Structures

High-resolution observations from ground-based telescopes like the SST and space instruments such as Hinode/SOT have revealed that solar prominences are composed of intricate fine-scale structures (Berger et al., 2008). The fundamental building blocks are thread-like features with widths often approaching the instrumental resolution limit of approximately 100 km, suggesting that true physical scales may be even smaller. This fine structure has profound implications for interpreting observations and constructing theoretical models.

A typical filament usually comprises three principal components. The spine constitutes the uppermost, horizontally oriented main body that aligns with the filament channel. In quiescent prominences, the spine may appear faint in Hα but prominent in the He II 304 Å line, a difference attributed to increased hydrogen ionization with height. The spine is not a entity but rather a bundle of numerous thin, predominantly horizontal threads. Barbs represent lateral structures that diverge from the spine and extend downward toward the chromosphere, giving many fila-

ments a comb-like appearance when viewed from above (Lin et al., 2008). High-resolution observations demonstrate that barbs themselves consist of dense packs of highly inclined threads, with their feet often rooted in or near concentrations of minority polarity magnetic flux at supergranulation boundaries. The extreme ends of filaments represent terminal sections that curve downward to the chromosphere, similar in nature to large barbs (Martin et al., 2008).

The existence of such fine structure brings consideration of the volume filling factor f, the fraction of a given resolution element actually occupied by the cool, dense plasma. Diagnostics based on UV and EUV line emissions suggest filling factors as low as 10^{-3} to 10^{-2} (Mariska et al., 1979; Widing et al., 1986; Cirigliano et al., 2004). This indicates that prominences are not smooth, uniformly filled volumes but rather tenuous ensembles of ultra-thin, dense threads embedded within a more transparent, hotter plasma. Reconciling this fine structure with requirements for thermal insulation, mass support against gravity, and continuous mass replenishment remains a central challenge in prominence physics.

1.1.5 Dynamical behaviour

Solar prominences are not only static structures. They exhibit a series of dynamical behaviours. One of the most remarkable behaviours is the ubiquitous presence of counterstreaming plasma flows observed along adjacent threads within the same prominence (Lin et al., 2003). Typical flow speeds range from 10 to 20 km s^{-1} in Hα observations (Zirker et al., 1998), while recent studies combining high-resolution EUV imagers have detected similar anti-parallel motions at speeds up to 70–80 km s^{-1} (Kucera, 2015). These flows are universally interpreted as field-aligned motions, providing an important diagnostic of the local magnetic field geometry. The persistence of counterstreaming implies continuous mass exchange, requiring mechanisms for plasma injection and drainage that can sustain the prominence over its observed lifetime.

Prominences also serve as natural resonators for magnetohydrodynamic waves, exhibiting oscillatory motions with periods spanning from tens of seconds to several hours (Molowny-Horas et al., 1999; Banerjee et al., 2007; Engvold, 2007). These oscillations are typically categorized by period: short-period ($P < 10$ min) oscillations often appear localized to individual threads with small velocity amplitudes; intermediate-period ($10 < P < 40$ min) oscillations; and long-period ($P > 40$ min) oscillations that can involve large prominence sections with substantial velocity amplitudes (Lin et al., 2003). The oscillations amplitudes decrease with time, with damping times typically 1–3 times the oscillation period (Oliver and Ballester, 2002). The study of these wave phenomena, known as prominence seismology, provides a powerful tool for inferring internal physical parameters such as magnetic field strength, density stratification, and the degree of plasma ionization (Lin, 2011).

Additional dynamic features include prominence plumes (mushroom caps) shaped structures observed in quiescent prominences with rise speeds of 20–30 km s^{-1} (Berger et al., 2010). These are thought to result from Rayleigh-Taylor instabilities at the prominence-corona inter-

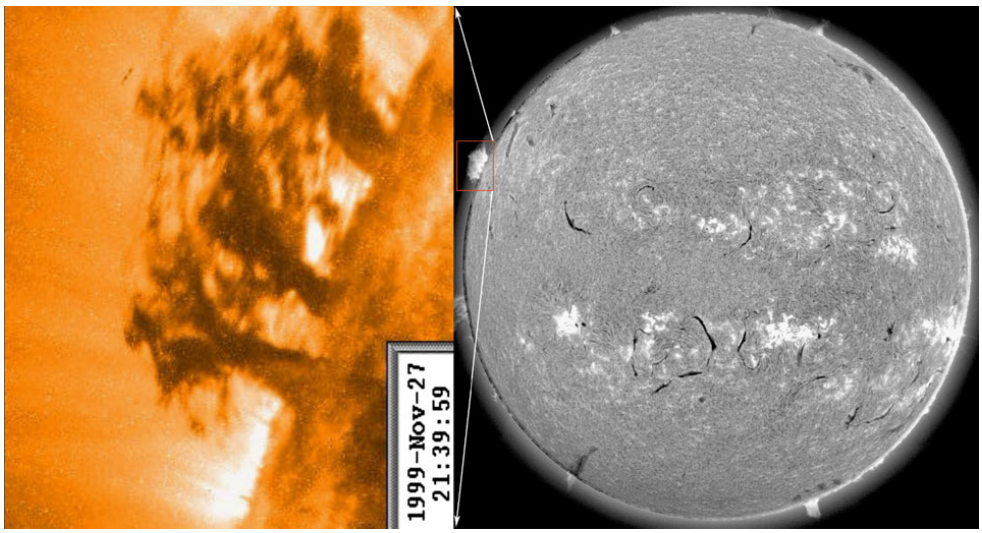

Figure 1.5: A group of tornado-like prominences observed in the 171 Å by Transition Region and Coronal Explorer (TRACE) in the left panel. The right panel shows the location of prominences on the limb by Hα(Figure 1 in (Panasenco et al., 2014)).

face. Tornado-like structures (Figure 1.5), appearing as vertical pillars in limb prominences with apparent rotational motions, have attracted considerable attention, though recent analyses suggest their twisted appearance may result from a combination of counterstreaming and oscillatory motions rather than true vortical flows (Panasenco et al., 2014). Minifilaments (small-scale analogues of large filaments) provide simplified systems for studying formation and eruption processes (Denker and Tritschler, 2009).

1.1.6 Eruptive Evolution and Associated Phenomena

The eruption of a solar prominence represents an event in solar activity, often constituting of a coronal mass ejection and frequently accompanied by solar flares. Multi-wavelength studies have delineated a characteristic three-stage kinematic evolution. The pre-eruptive activation phase involves a gradual, quasi-static ascent at speeds typically below 1 km s^{-1}, persisting for hours before the main eruption (Sterling and Moore, 2004; Isobe et al., 2007). During this phase, the prominence may exhibit increased absorption or emission, activation of barb structures, and the onset of large amplitude oscillations (Engvold et al., 2001; Démoulin and Vial, 1992).

This initial stage transitions into a phase of rapid acceleration, where the prominence undergoes strong upward acceleration reaching values of tens to hundreds of m s^{-2}. Velocity increases rapidly to hundreds of km s^{-1} (Sterling and Moore, 2004; Isobe et al., 2007). The onset of this explosive phase often coincides temporally with the beginning of flare brightening in microwaves and EUV emissions. Observations by Grechnev et al. (2006) demonstrate that during this stage, the filament's structure undergoes significant transformation: barb structures detach from the photosphere, and a helical flux rope configuration often becomes apparent in EUV imagery.

Following this acceleration phase, the eruptive prominence enters a stage of free expansion or propagation, where it moves outward at nearly constant speed. In this stage, different components of the CME (including the frontal structure, cavity, and core) frequently exhibit self-similar expansion, maintaining their relative shapes while scaling in size (Uralov et al., 2005).

1.1.7 Theoretical Models and Initiation Mechanisms

The physical mechanisms that trigger the transition from stable equilibrium to eruptive instability is a central theoretical challenge in prominence research. Observations from multi-wavelength studies have been interpreted within various conceptual frameworks. The dual-filament initiation model, as discussed by Uralov et al. (2002), provides one such framework derived from analysis of specific eruptive events. As shown in Figure 1.6, this model assumes that many erupting filaments originate as two segments connected by a coronal backbone magnetic field. Eruption initiates through a sequence involving: primary magnetic reconnection at the interaction region between segments, which increases magnetic tension and provides initial lift; detachment and reconnection of filament barbs, facilitating the formation of a twisted flux rope and releasing additional energy; and finally, if the combined upward forces suffice, reconnection in the overlying coronal field that severs the final magnetic constraints, allowing explosive eruption.

This model incorporates elements from several established theoretical models. The initial phase shares characteristics with Tether-Cutting models (Moore et al., 2001). The barb detachment and flux rope formation phase comes from models of flux rope emergence or instability (Forbes and Isenberg, 1991; Amari et al., 2000). The final overlying field reconnection in dual-filament initiation model is similar as the Breakout model, where reconnection at a null point above the core field removes the overlying magnetic confinement (Antiochos et al., 1999).

Gradual magnetic flux cancellation at the polarity inversion line may also slowly erode stabilizing magnetic gradients and trigger the eruption (Grechnev et al., 2006). The relative importance of these mechanisms likely varies with the magnetic environment, explaining the diversity observed in pre-eruptive signatures and eruption characteristics.

1.1.8 Interrelationship with Flares and Coronal Mass Ejections

The relationship between prominence eruptions, solar flares, and coronal mass ejections represents a fundamental aspect of solar activity physics. "flare-associated" and "filament-eruption-associated" CMEs are regarded as two different kinds of processes before. But by contemporary understanding, supported by multi-wavelength observations, these are different manifestations of the same underlying magnetic instability, with observational differences arising primarily from the magnetic environment.

The multi-wavelength perspective clarifies the roles of various observed features within the

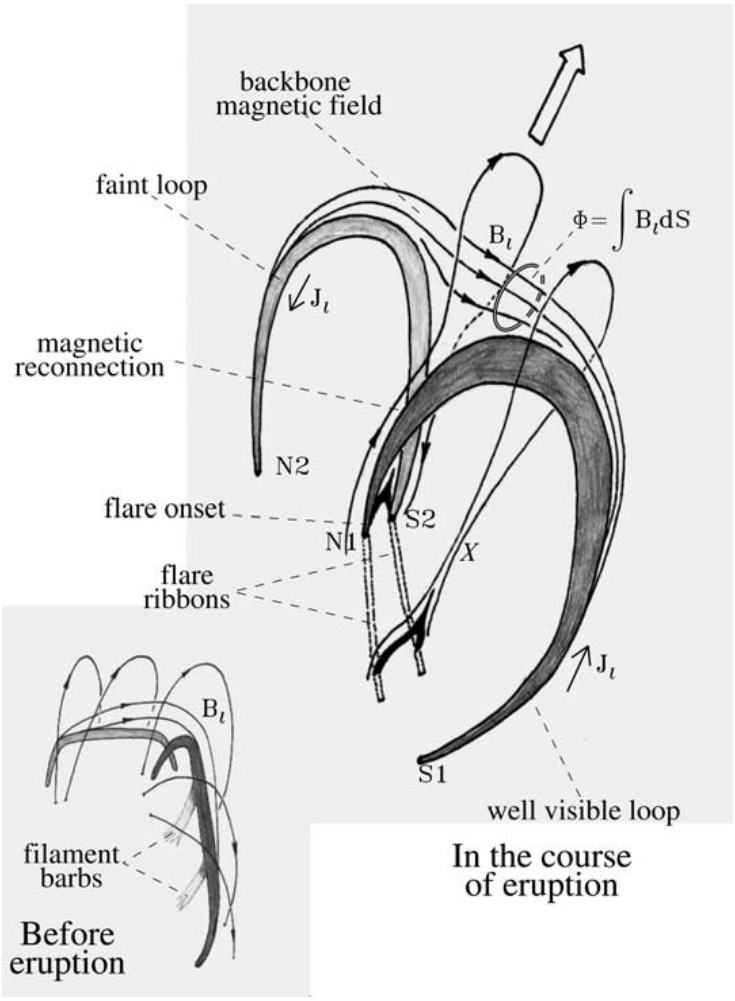

Figure 1.6: Dual-Filament CME initiation model. The initial filament contains two segments connected by a coronal backbone magnetic field (Figure 9 in (Uralov et al., 2002)).

eruptive event. The erupting cool prominence constitutes the CME core. The bright, expanding loops observed in EUV and soft X-rays form the post-eruptive arcade beneath the evacuated filament channel, corresponding to the classical flare loops (Švestka, 2001). The faint, broad structure leading the eruption in white-light coronagraphs represents the CME frontal structure, often visible in EUV as a diffuse brightening ahead of the core (Uralov et al., 2005). This integrated view frames the entire process as a magnetic field reconstruction event, where the loss of equilibrium of a coronal magnetic structure (containing the prominence) drives both the mass ejection and the magnetic reconnection responsible for the flare energy release.

1.2 Radiative Transfer

The radiative transfer process is very important for analysis in these works. Therefore, we will discuss radiative transfer equations and related quantities in this section. The discussion will follow contents from Heinzel (2014).

1.2.1 Basic Principles of Radiative Transfer

The diagnostic of prominence plasma relies fundamentally on the theory of radiative transfer. The propagation of radiation through a prominence is governed by the Radiative Transfer Equation (RTE). For a specific frequency ν along a path element ds, the change in specific intensity I_ν is given by:

$$\frac{dI_\nu}{ds} = -\chi_\nu I_\nu + \eta_\nu, \tag{1.1}$$

where I_ν is the specific intensity of radiation, and χ_ν and η_ν are the absorption and emission coefficients, respectively. The optical-depth scale at a given frequency v is defined by the absorption coefficient. We can regard a prominence as a 1D slab in Figure 1.7 to analyse the problem. If we use x as the reference coordinate, which is along the normal of the slab, it is given by $d\tau_\nu = -\chi_\nu dx$. The RTE then takes the standard form:

$$\mu \frac{dI_\nu}{d\tau_\nu} = I_\nu - S_\nu, \tag{1.2}$$

with $\mu = \cos\theta$ and the source function $S_\nu \equiv \eta_\nu/\chi_\nu$. As shown in Figure 1.7, θ is the angle between ds and dx.

The source function is a fundamental quantity that determines the radiation field within the plasma. Under Local Thermodynamic Equilibrium (LTE) conditions, where collisions dominate, S_ν equals the Planck function: $S_\nu = B_\nu(T)$. However, under typical prominence conditions characterized by low densities ($n_e \sim 10^{10} - 10^{11}$ cm^{-3}, lower in prominence centre, higher in prominence surface) and strong external radiation fields from the solar disc, they will show significant departures from LTE (Engvold, 2014). The source function is then no longer ther-

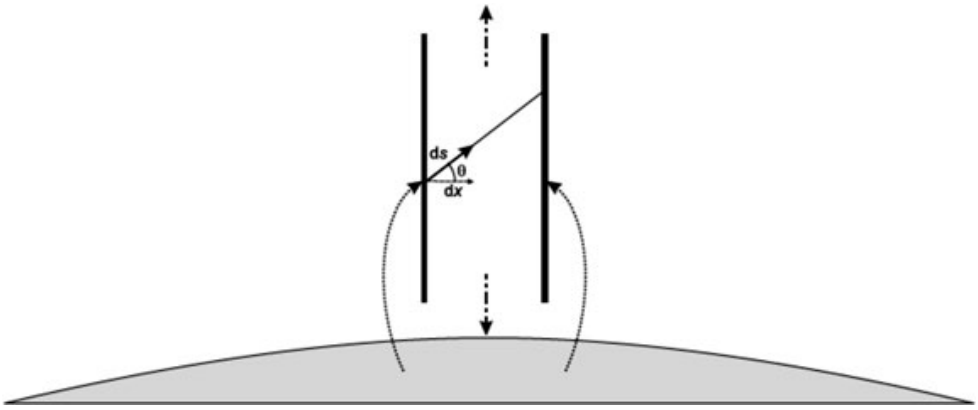

Figure 1.7: 1D prominence slab vertically standing above the solar surface (Fig.5.1 in (Heinzel, 2014)).

mal but is instead dominated by scattering processes, particularly for resonance lines in the cool prominence core. This necessitates a non-LTE (NLTE) treatment of the radiative transfer problem.

For a known source function, the emergent intensity at the slab surface is found through the formal solution of the RTE. Considering a plane-parallel slab of total optical thickness $\tau_\nu^{\rm tot}$ along the line of sight, the specific intensity emerging at an angle θ (with $\mu = \cos\theta$) is:

$$I_{\nu\mu} = I^0_{\nu\mu} e^{-\tau_\nu^{\rm tot}/\mu} + \int_0^{\tau_\nu^{\rm tot}} S_\nu(t_\nu) e^{-t_\nu/\mu} \frac{dt_\nu}{\mu}, \tag{1.3}$$

where $I^0_{\nu\mu}$ is the incident intensity illuminating the opposite side of the slab. The first term represents the attenuated background radiation, while the second integrates the contributions of the internal source function along the path to the surface. This equation is fundamental for interpreting both emission line profiles from limb prominences and absorption profiles of on-disc filaments against the brighter solar disc (Heinzel, 2014).

1.2.2 Statistical Equilibrium

The absorption and emission coefficients are determined by atomic level populations and atomic transition parameters. For a spectral line arising from a bound-bound transition between a lower level i and an upper level j, the absorption coefficient (corrected for stimulated emission) is:

$$\chi_\nu = \frac{h\nu_{ij}}{4\pi} \left(n_i B_{ij} \phi_\nu - n_j B_{ji} \psi_\nu \right), \tag{1.4}$$

and the emission coefficient is:

$$\eta_\nu = \frac{h\nu_{ij}}{4\pi} n_j A_{ji} \psi_\nu, \tag{1.5}$$

where n_i and n_j are the population densities of the levels, A_{ji}, B_{ij}, and B_{ji} are the Einstein coefficients, and ϕ_ν and ψ_ν are the normalized absorption and emission profiles, respectively

(Heinzel, 2014)).

The line profile ϕ_ν is generally described by a Voigt profile, which is a convolution of a Cauchy-Lorentz distribution and a Gaussian distribution.:

$$\phi_\nu = \frac{1}{\sqrt{\pi}\Delta\nu_D} H(a,x), \tag{1.6}$$

where $\Delta\nu_D$ is the Doppler width, $x = (\nu - \nu_0)/\Delta\nu_D$, a is the damping parameter, and $H(a,x)$ is the Voigt function. For optically thick lines, the line-wing broadening is governed by the Voigt profile. For many prominence lines, especially optically thin ones, their absorption profiles can be considered as a Gaussian profile.

The atomic level populations n_i are determined by solving the Equations of Statistical Equilibrium (ESE). The general form of the ESE (Equations of Statistical Equilibrium) describes the time evolution of the populations of various atomic species in a plasma. The ESE is given by

$$\begin{gathered} \frac{dn_i}{dt} = \sum n_j(R_{ji} + C_{ji}) - n_i \sum (R_{ij} + C_{ij}) \\ \frac{dn_i}{dt} = \frac{\partial n_i}{\partial t} + \frac{\partial n_i v}{\partial x} \end{gathered} \tag{1.7}$$

where R_{ij} are the radiative rates, those for absorption and stimulated emission depend on the line intensity, and C_{ij} are the collisional rates proportional to the electron density n_e and dependent on temperature T through the function $\Omega(T)$: $C_{ij} = n_e \Omega_{ij}(T)$. $\Omega_{ij}(T)$ represents the probability of the collisional transition from the energy level i to the energy level j, and depends on the temperature T of the plasma. According to the principle of detailed balance, in thermal equilibrium, the rate of a collisional transition from level i to level j must be equal to the rate of the reverse collisional transition from level j to level i: $C_{ji} = C_{ij}$ (Heinzel, 2014)).

An insightful simplification is the two-level atom model. Assuming collisional excitation from the ground level g and spontaneous radiative decay from the upper level j dominate, the ESE reduces to $n_e n_g C_{gj} = n_j A_{jg}$. The corresponding line source function becomes:

$$S = (1 - \varepsilon)\bar{J} + \varepsilon B_\nu(T) \tag{1.8}$$

where $\varepsilon = C_{jg}/(A_{jg} + C_{jg})$ is the photon destruction probability. Here C_{jg} is the collisional de-excitation rate from level j to level g, and A_{jg} is the spontaneous radiative decay rate. For typical quiescent-prominence parameters, $T \approx 8000$ K and $n_e \approx 10^{10}$ cm^{-3}, ε for the hydrogen Lyman α line is around 10^{-6}, so the source function is dominated by scattering. However, this is line-dependent, and collisions can become important for some transitions at densities around 10^{11} cm^{-3}.

1.2.3 Frequency Redistribution

In the scattering process, the frequency of the re-emitted photon may be correlated with that of the absorbed photon. In the common assumption of Complete Redistribution in Frequency (CRD), where $\psi_\nu \equiv \phi_\nu$, the absorption profile is completely not related to the emission profile. However, for strong resonance lines formed under low-collisional conditions, scattering is partially coherent in the atom's rest frame. This necessitates the use of Partial Redistribution (PRD) formalisms.

In PRD, the emission profile ψ_ν is not equal to ϕ_ν but depends on the radiation field through a redistribution function $R(\nu', \nu)$:

$$\psi_\nu = \frac{\int_0^\infty R(\nu', \nu) J_{\nu'} d\nu'}{\bar{J}} \tag{1.9}$$

A commonly used form for resonance lines is $R(\nu', \nu) = \gamma_1 R_{\rm II}(\nu', \nu) + (1-\gamma_1) R_{\rm III}(\nu', \nu)$, where $R_{\rm II}$ describes coherent scattering in the atom's frame, $R_{\rm III}$ describes complete redistribution in the atom's frame, and γ_1 is the branching ratio, the probability that a collisional perturbation of the upper atomic state does not destroy the coherence in the atom's frame. PRD significantly affects the emergent profiles of optically thick lines like H I Ly-α and He II 304 Å, producing more pronounced central reversals and altering wing intensities. It is therefore crucial for accurate diagnostics, especially when comparing synthetic profiles with high spectral resolution observations (Heinzel, 2014)).

1.2.4 Diagnostic Methods for Optically Thin Plasmas

The hot plasma of the Prominence-Corona Transition Region (PCTR), observed in UV and EUV lines, frequently satisfies the optically thin approximation. In this regime, the emergent intensity of a spectral line can be expressed as:

$$I(\lambda_{ij}) = \frac{1}{4\pi A} \int_V Ab \cdot G(T_e) n_e^2 \, dV \tag{1.10}$$

where A is the cross-sectional area of the emitting volume V, Ab is the elemental abundance, and $G(T_e)$ is the contribution function (Parenti, 2014b).

The emission measure (EM) represents the amount of emitting material along the line of sight:

$$\mathrm{EM} = \int_l n_e^2 \, dl \quad [\mathrm{cm}^{-5}] \tag{1.11}$$

If we want to apply a more detailed diagnostics, the differential emission measure (DEM) provides a temperature distribution:

$$\mathrm{DEM}(T) = n_e^2 \frac{dl}{dT} \quad [\mathrm{cm}^{-5}\mathrm{K}^{-1}] \tag{1.12}$$

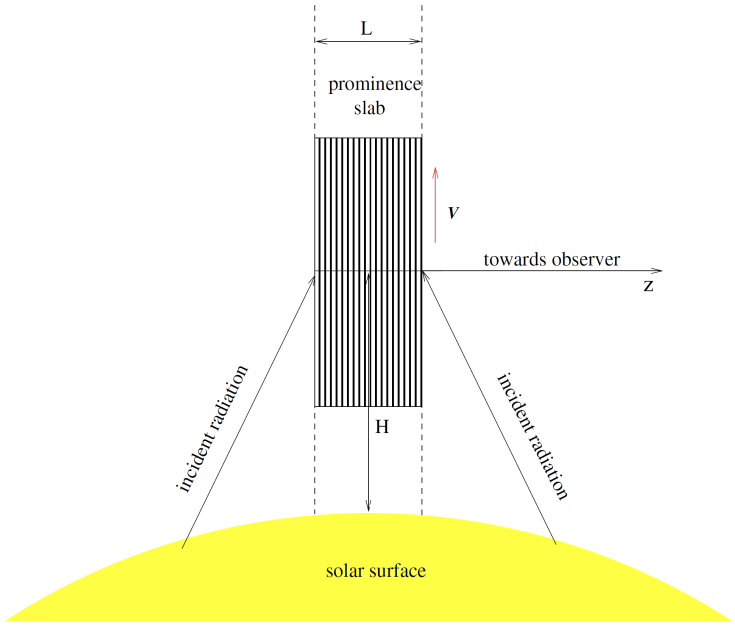

Figure 1.8: The schematic of 1D prominence slab model (Fig.6 in Labrosse and McGlinchey (2012))

related to the intensity by $I_\lambda \propto \int AbG_\lambda(T)\mathrm{DEM}(T)dT$. Inverting a set of observed line intensities to obtain the DEM is a standard procedure.

The ratio of intensities from two lines of the same ion can be a sensitive function of electron density if one of the lines involves a metastable level (e.g., the C III 977/1176 Å ratio). Similarly, the ratio of lines from adjacent ionization stages of the same element can provide a temperature diagnostic under the assumption of ionization equilibrium. These techniques yield average values along the line of sight.

1.2.5 The PRODOP Radiative Transfer Code

For the analysis of prominences in this thesis, we employ the one-dimensional NLTE radiative transfer code PRODOP (Gouttebroze and Labrosse, 2000). This code is specifically designed to model the spectrum of solar prominences and filaments, providing a robust tool for diagnosing plasma parameters under non-equilibrium conditions.

In Figure 1.8, we can see that, in this code, the prominence is modelled as a 1D slab oriented vertically above the solar surface, incorporating the prominence-corona transition region (PCTR). The model includes one bulk velocity component, which is assumed here to correspond to the radial velocity of the prominence, as an input parameter. Additional input parameters include the incident spectral profile, the temperature and pressure at the slab centre and at the boundary with the corona, the steepness of the temperature gradient in the PCTR, and the slab's total column mass, microturbulent velocity and altitude (Labrosse and McGlinchey, 2012). The PCTR modelling allows for gradients in temperature and pressure. The input of this velocity

component makes it suitable for studying eruptive events. However, this treatment is a simplification, since PRODOP does not include independent radial and horizontal velocity components. Recent modelling has shown that horizontal motions can also produce significant Doppler dimming or brightening effects and may be as important as radial motions for some lines (Peat et al., 2024). The code solves the coupled statistical equilibrium and radiative transfer equations iteratively. The statistical equilibrium equations determine the atomic level populations by balancing radiative and collisional population and depopulation rates, while the radiative transfer equation determines the radiation field and source functions throughout the slab. These two parts are coupled because the level populations depend on the radiation field, and the radiation field depends on the opacity and emissivity set by the level populations. The Feautrier method is used to solve the transfer equation as a finite-difference linear system, and variable Eddington factors are introduced to reduce the angular dependence of the radiation field and improve the efficiency of the calculation.

The thermodynamic structure of the slab is parameterized. Following Anzer and Heinzel (1999), temperature and pressure profiles are given by:

$$T(m) = T_{\rm cen} + (T_{\rm tr} - T_{\rm cen}) \left[1 - 4\frac{m}{M}\left(1 - \frac{m}{M}\right)\right]^{\Gamma}, \tag{1.13}$$

$$p(m) = 4p_c\frac{m}{M}\left(1 - \frac{m}{M}\right) + p_0, \tag{1.14}$$

$T_{\rm cen}$ is the central temperature and $T_{\rm tr}$ is the boundary transition-region temperature. Γ is the steepness of the temperature gradient in the PCTR. p_0 is the pressure at the outer boundary and $p_c = p_{\rm cen} - p_0$. p_c is the difference between the pressure at the centre and at the outer boundary. The column mass m ranges from $m = 0$ to $m = M$ (from one surface to the opposite surface). The parameter Γ is important because it controls how rapidly the temperature changes from the hot PCTR to the cool prominence core. A larger value of Γ produces a steeper transition near the slab boundaries, whereas a smaller value gives a more gradual temperature variation and a larger amount of material at high temperatures. This affects the ionization balance, optical depth, and contribution functions of spectral lines, and therefore has a direct influence on the emergent line intensities and profiles. It should be noted that Eqs. 1.13 and 1.14 are simple approximations for the thermodynamic structure of the slab. They are not intended to represent a self-consistent MHD solution, but rather provide a practical way to explore how different prominence core and PCTR conditions affect NLTE radiative transfer calculations. Therefore, the inferred parameters should be interpreted as diagnostic quantities within this 1D slab framework, rather than as a full description of the dynamical magnetic structure of the prominence. Although Eq. 1.13 formally varies across the whole slab, the factor in brackets can be written as $(2m/M - 1)^2$, so near the slab centre ($m/M \simeq 1/2$) the temperature remains close to $T_{\rm cen}$, especially for $\Gamma > 1$. Thus, the main temperature gradient is concentrated near the slab boundaries and represents the PCTR, while the prominence core is approximately isothermal.

The computational methodology is detailed in Labrosse et al. (2007, 2008). We require estimates for the ranges of input parameters prior to inputting them into the model. The code also requires a detailed incident radiation input. Subsequently, the model can be used to investigate the formation of different spectral line profiles.

This feature allows PRODOP to accurately model critical effects such as Doppler dimming (or brightening) in resonance lines, which serves as a powerful diagnostic for flows in erupting prominences (Labrosse et al., 2007).

In this work, PRODOP is used to compute synthetic line profiles for hydrogen Lyman lines and Helium lines. By comparing these synthetic profiles with observations like Solar Orbiter/SPICE and STEREO/EUVI, we aim to analyse the line formation processes and physical conditions within prominences.

1.3 Instrumentation

In this section, we will give the overview of the instrumentation we will use in this work. we will introduce the Solar Orbiter mission, specifically the SPICE spectrometer and the EUI imager, STEREO/EUVI and GONG Hα.

1.3.1 Solar Orbiter

Solar Orbiter is a Sun-observing satellite developed by the European Space Agency (ESA) (Müller et al., 2020). The highly elliptical orbit allows it to go close to the Sun. Since 2025, the orbit is inclined with respect to the ecliptic, allowing for the view of the poles.

Extreme Ultraviolet Imager

The Extreme Ultraviolet Imager (EUI) is on board the Solar Orbiter (Rochus et al., 2020). EUI captures images of the Sun's atmosphere in the extreme ultraviolet range, providing information about the Sun's corona, solar flares, and other phenomena. Full-Sun Imager (FSI) is a part of the EUI instrument suite on board the Solar Orbiter spacecraft. FSI is designed to observe the full solar disc in two EUV channels: 174 Å and 304 Å. The observations at various wavelengths enable the acquisition of detailed visual data of the sun's entire surface, thereby facilitating scientific analysis of various solar layers and phenomena.

Figure 1.9 shows a full disc image of the Sun along with prominence eruption observed in the 304 Å channel of EUI/FSI on 15 February 2022.

EUI observes the sun in multiple channels. Of particular interest to this project is the 304 Å channel. The 304 Å channel is primarily sensitive to emission from the He II 303.78 Å line, which forms in relatively cool plasma in the transition region between the solar chromosphere

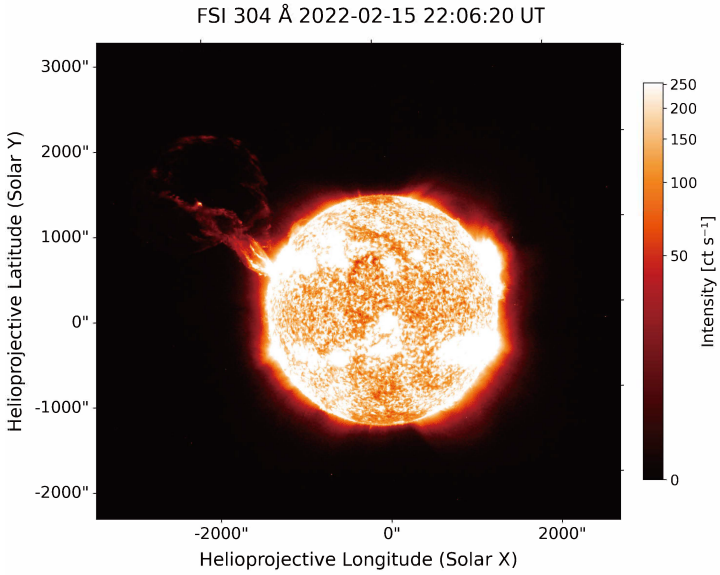

Figure 1.9: The full disc image of the Sun with the prominence eruption observed on 15 February 2022, by EUI/FSI 304 Å (Figure from Zhang et al (2026d, submitted)).

and corona. However, this channel can also include contributions from coronal emission, particularly from the Si XI 303.32 Å line. The 304 Å line has demonstrated high sensitivity to the radial movement of the solar prominence. This is due to its formation primarily occurring through the scattering of incident radiation from the Sun (Labrosse and McGlinchey, 2012). Here the incident radiation mainly refers to He II 304 Å radiation from the solar disc, produced in the chromosphere and transition region below the prominence. Coronal emission mainly contributes as background emission or passband contamination. It provides information on the dynamics of prominences, filaments, and other features on the solar disc (Mierla et al., 2022).

Spectral Imaging of the Coronal Environment

The Spectral Imaging of the Coronal Environment (SPICE) instrument is an imaging spectrometer operating at extreme ultraviolet (EUV) wavelengths from 69.6–79.6 nm (short wavelength, SW channel) and 96.0–105.8 nm (long wavelength, LW channel) (SPICE Consortium et al., 2020). SPICE's primary objective is to support the scientific aims of the Solar Orbiter mission by offering detailed insights into the physical properties and composition of the plasma within the solar atmosphere. SPICE employs two detector arrays, each with a format of 1024 × 1024 pixels, to simultaneously record dispersed spectra in these bands. The observations utilize a $4''$ slit width. The in-flight performances of the instrument are a spatial resolution of $6.7''$ (sampling of 1.098 arcsec/pixel across the slit) and a spectral resolution of about 9.4 pixels for the LW channel (Fludra et al., 2021). An important instrumental issue for SPICE is its point spread function (PSF), which can redistribute light between neighbouring spatial and spectral pixels. This may produce artificial Doppler shift patterns around bright structures, and therefore Doppler velocities and line widths derived from SPICE data must be interpreted with caution

(Plowman et al., 2023).

1.3.2 Solar Terrestrial Relations Observatory

The Solar Terrestrial Relations Observatory (STEREO) spacecraft, launched in 2006, aims to study Coronal Mass Ejections (CMEs) and solar wind dynamics (Kaiser et al., 2008). Two spacecraft orbit the Sun at approximately 1 AU, with one spacecraft leading Earth (STEREO-A) and the other trailing behind (STEREO-B). Equipped with various instruments, including coronagraphs and particle sensors, STEREO provides crucial data for understanding space weather and predicting CME impacts on Earth. STEREO-B has been out of contact since Oct 1, 2014. However, the remaining STEREO-A still provides a complementary view of solar structures under a different line of sight compared to Earth-based observations.

The Extreme Ultraviolet Imager (EUVI) (Wuelser et al., 2004) is a component of the Sun-Earth Connection Coronal and Heliospheric Investigations (SECCHI) instrument suite developed for NASA's STEREO mission (Howard et al., 2008). It focuses on the initiation and early evolution of CMEs. The EUVI features 2048 x 2048 pixel detectors that provide a field of view extending to 1.7 solar radii and records images in four EUV spectral channels, 171, 195, 284 and 304 Å covering a temperature range from 0.1 to 20 MK.

1.3.3 GONG Hα Telescope

The Global Oscillation Network Group (GONG) is a network of ground-based telescopes designed to observe the Sun in the Hα wavelength (656.3 nm) (Harvey et al., 1996). We use Hα images from the El Teide telescope in the GONG network. The Hα line is particularly useful for studying solar prominences, filaments, and other chromospheric phenomena, as it provides high-contrast images of these features and has long-term full-disc monitoring.

1.4 Concluding Remarks

This Chapter has provided an introduction to the physical characteristics, dynamics, and observational diagnostics of solar prominences. It concludes with an overview of the instrumentation and radiative transfer methods that will be employed in this work. As outlined, the primary observational data will come from the *Solar Orbiter* mission, specifically the SPICE spectrometer and the EUI imager, with supporting context from STEREO/EUVI and GONG Hα. The focus of the analysis will be on non-LTE radiative transfer modelling using the PRODOP code, applied to ultraviolet spectral lines to invert the thermodynamic properties of solar prominences.

In Chapter 2, we will introduce analysis of Lyman β and Lyman γ lines in a pre-eruptive and eruptive prominence with Solar Orbiter SPICE observations. In Chapter 3, we will introduce Non-LTE analysis of pre-eruptive prominence plasma parameters' effects on the Lyman β and

Lyman γ lines with Solar Orbiter SPICE observations. In Chapter 4, we will introduce prominence plasma parameters maps inferred from Lyman β and Lyman γ observations and Non-LTE modelling. In Chapter 5, we will introduce analysis of eruptive prominence plasma parameters' effects on the He II 304 Å line with Solar Orbiter EUI observations. In Chapter 6, I will give conclusions for this thesis.

Chapter 2

Analysis of Lyman β and Lyman γ Lines

In this chapter, we will introduce analysis of Lyman β and Lyman γ lines in a pre-eruptive and eruptive prominence with Solar Orbiter SPICE observations. I will show properties of Lyman β and Lyman γ lines and compare them between the pre-eruptive phase and the eruptive phase.

Most contents of this chapter (i.e. text, tables and figures) come from Zhang et al. (2026a) and are written or created by me unless otherwise stated. I analysed the data of SPICE observations on April 15th, 2023, generated all figures in this paper and proposed a way of calculating the radial velocity of an eruptive filament from a pair of 2D images. Nicolas Labrosse gave opinions about contents of figures and texts to comprise the paper, improved them and ensure the accuracy. Susanna Parenti and Therese A. Kucera gave supports with details and analysis methods of SPICE observations on April 15th, 2023.

The first dedicated observation of an off-limb prominence by Solar Orbiter took place on April 15, 2023. Solar prominences, which are large-scale structures of plasma suspended in the solar corona, play a critical role in the dynamics of the solar atmosphere and are often associated with coronal mass ejections (CMEs) that can significantly impact space weather. Understanding the physical conditions within prominences, such as temperature, column mass, pressure, and velocity, is essential for advancing our knowledge of solar physics and improving space weather forecasting.

The Lyman series of hydrogen plays a crucial role in understanding the physical processes occurring in the solar atmosphere. These spectral lines, formed primarily in the chromosphere and transition region, provide valuable diagnostics for plasma properties such as temperature, density, and dynamics. Early studies, such as those of Vernazza et al. (1981), established the foundational models of the solar chromosphere and transition region, highlighting the importance of Lyman series emissions in radiative transfer calculations. Subsequent observations from space-based instruments, including SOHO/SUMER (Curdt et al., 2001), have significantly advanced our understanding of the spatial and temporal variations of these lines across the solar disc. Recent studies have further explored the diagnostic potential of the Lyman series in solar prominences and fine structures. For instance, Vial et al. (2007) observed the Lyman

α and Lyman β profiles in solar prominences using SOHO/SUMER, revealing that the Lyman α/Lyman β ratio is sensitive to the fine structure and mass motions within prominences. Furthermore, Heinzel et al. (2001) analysed the complete hydrogen Lyman spectrum in solar prominences, demonstrating the importance of partial frequency redistribution (PRD) and the role of the prominence-corona transition region (PCTR) in shaping the observed line profiles. In addition, recent work by Hasegawa et al. (2020) investigated the formation of Lyman β and O I 102.7/102.8 nm lines, emphasizing their sensitivity to temperature and velocity perturbations from the low mid-chromosphere to the transition region. These studies highlight the importance of the Lyman series in understanding physical processes in the solar atmosphere.

Recent advancements in prominence modelling have shown that the asymmetries observed in Lyman line profiles, such as Lyman α and Lyman β, can be attributed to the combined effects of Doppler shifts and optical depth variations within individual fine-structure threads (Gunár et al., 2008). These asymmetries are particularly sensitive to the physical parameters of prominences, such as temperature, density, and velocity fields, which vary significantly across the PCTR. The formation of Lyman lines in prominences is strongly influenced by the temperature and density gradients within the PCTR. Studies have shown that the Lyman lines, particularly Lyman β and higher members of the series, are formed in the outer layers of the prominence, where the temperature increases sharply from the cool central regions to the hot corona. The brightness temperature of the Lyman lines, derived from the spectral radiance at line centre, has been found to be largely independent of the upper level number, indicating that the emitting regions are significantly hotter than the prominence core (Stellmacher and Wiehr, 2008). Furthermore, Tian et al. (2009) demonstrated that the Lyman line profiles are also influenced by the dynamics of the solar atmosphere, with the Lyman α and Lyman β lines exhibiting opposite asymmetries in response to transition-region flows. These highlight the critical role of parameter analysis in interpreting Lyman line observations and diagnosing the physical conditions within prominences.

The primary objective of this study is to analyse the hydrogen Lyman β and Lyman γ lines of a solar prominence during the pre-eruptive phase and eruptive phase observed by SPICE on April 15, 2023. In particular, their line widths provide diagnostics of the thermal and non-thermal broadening of the line profiles, while their integrated intensities help investigate the spatial variation of the prominence emission. Understanding these pre-eruptive conditions is crucial, as they set the stage for the subsequent eruption dynamics. This will provide valuable insights into the thermodynamic and dynamic properties of eruptive prominences, contributing to a deeper understanding of their role in solar activity and space weather. The event was observed during its pre-eruptive and eruptive phases, when significant changes in temperature, density, and pressure are expected, and thus the Lyman line profiles offer unique insight into the evolving prominence plasma.

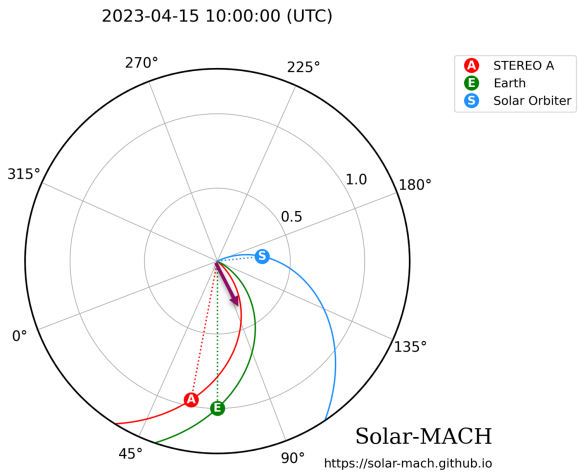

Figure 2.1: The positions of different spacecraft. The arrow is the eruption direction of the prominence (Figure from Zhang et al. (2026a)).

2.1 Observations

From Global Oscillation Network Group's (GONG) point of view, the prominence was a large quiescent prominence in the northern hemisphere that had been apparent on the disc for 6 days. From 07:30 -10:00 UT the prominence was starting to rise, but was not yet erupting. At around 10:00 UT the central section of the prominence erupted, leaving behind segments to either side.

2.1.1 Instrumentation

Solar Orbiter

Solar Orbiter is a Sun-observing satellite developed by ESA (the European Space Agency) (Müller et al., 2020). We have given detailed description of the Solar Orbiter in Section 1.3.1. Solar Orbiter operates in a highly elliptical orbit around the Sun, with most of its remote sensing observations taking place at perihelion. As shown in Figure 2.1, during these observations Solar Orbiter was 0.31 AU from the Sun and roughly in quadrature with Earth. At this time, $1''$ at Solar Orbiter corresponds to $0.31''$ as seen from 1 AU.

In these observations, SPICE contributes to addressing Solar Orbiter's Science Objective on coronal mass ejection (CME) formation through coordinated prominence observations during a dedicated 10-hour perihelion campaign. For these observations, SPICE was pointing towards the edge of the solar disc to observe limb prominences and coronal structures above the surface, with the Earth quadrature configuration, combining SPICE's spectral diagnostics with EUI's high-resolution imaging. We only have EUI/HRI observation till 05:52 UT. In this chapter, we concentrate on the analysis of SPICE data. The difference in the wavelength sampling between the pre-eruption and eruption datasets (0.0096 nm/pixel and 0.0192 nm/pixel, respectively) results from different binning factors, indicating that the eruption raster was acquired with coarser

Table 2.1: Summary of SPICE observational parameters in this study (pre-eruption vs. eruption). X and Y coordinates are from the point of view of Solar Orbiter.

Parameter	Pre-eruption	Eruption
Observations		
Date	15 April 2023	15 April 2023
Time window (UTC)	07:03–08:09 UT	08:13–11:58 UT
SOOP campaign	R_BOTH_HRES_HCAD_Nanoflares	R_BOTH_HRES_HCAD_Nanoflares
Slit width	$4''$	$4''$
Exposure time	89.6 s	60.0 s
Field of view (Helioprojective)	X: $-2823''$ to $-2560''$ Y: $1035''$ to $2166''$	X: $-3040''$ to $-2033''$ Y: $1102''$ to $2129''$
Spectral characteristics		
Wavelength range (LW)	96.0–105.8 nm	8 selected spectral windows including 102.28–102.87 nm (Lyβ window)
Spectral resolution	Approximately 0.07 nm	Approximately 0.07 nm
Spectral dispersion	0.0096 nm/pixel (unbinned)	0.0192 nm/pixel (binned)
Photometric calibration		
Calibration factor	100.50 DN/(W m^{-2} sr^{-1} nm^{-1})	139.65 DN/(W m^{-2} sr^{-1} nm^{-1})

spectral sampling.

For the pre-eruption raster we analyse, we have a full spectrum in the given range of the LW channel. During the eruptive phase, the raster covers a wider field of view and multiple spectral windows including the Lyman β line at 102.57 nm. The data span from 07:03 to 08:09 UT, before the eruption, and from 08:13 to 11:58 UT during the eruption (DOI:10.48326/idoc.medoc.spice.5.0). Table 2.1 summarizes the key observational parameters discussed above.

STEREO

The Extreme UtraViolet Imager aboard the Solar Terrestrial Relations Observatory-A (STEREO/EUVI-A) (Kaiser et al., 2008; Howard et al., 2008) produced EUV images in four wavebands. We have given detailed description of the Solar Orbiter in Section 1.3.2. On the day of the observations described here, there was a 2.5 minute cadence in the 19.5 nm band. The response function is peaked at $log\ (T) = 6.2$ in the 19.5 nm band (Wuelser et al., 2004).

2.1.2 Observation

Figure 2.2 shows images of integrated intensities of the prominence taken by SPICE before eruption in Lyman β and Lyman γ lines. Figure 2.3 shows the prominence observed by EUI/HRI$_{\mathrm{EUV}}$ at 05:52:57 UT, 15 April 2023 in the 17.4 nm channel, which is 4 hours before eruption (DOI: https://doi.org/10.24414/z818-4163). The region of the SPICE observation is shown as the red rectangle region in Figure 2.3.

Figure 2.4 shows the LW channel observation of SPICE at 07:37:39 UT. The Lyman β and Lyman γ line profiles on the right panels in Figure 2.4 are from the green cross in Figure 2.2. The slit position is the same as the blue cut in Figure 2.2 (x=5 in pixel coordinate). The green cross is at the location of maximum intensity along the prominence region of the cut. The red

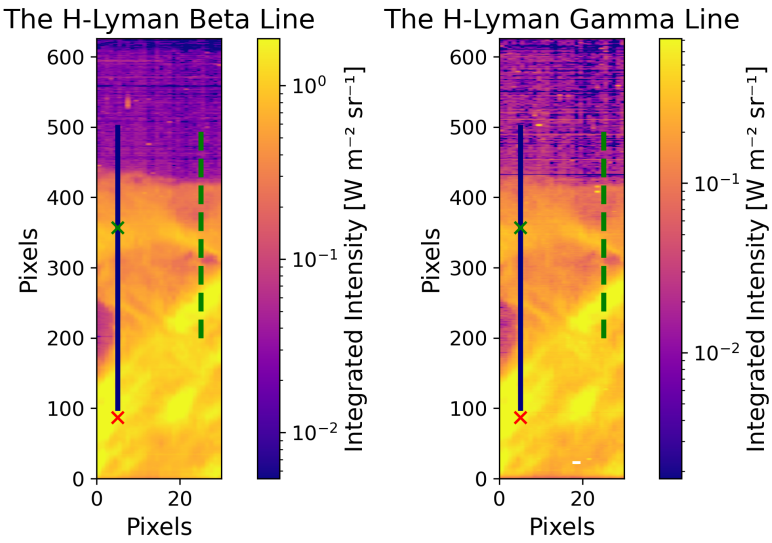

Figure 2.2: The SPICE observation of the integrated intensity of the Lyman β and Lyman γ lines taken from 07:03 - 08:09 UT, 15 April 2023. The green cross has the maximum intensity of the prominence region along the blue cut. The red cross has the maximum intensity of the disc region along the blue cut (Figure from Zhang et al. (2026a)).

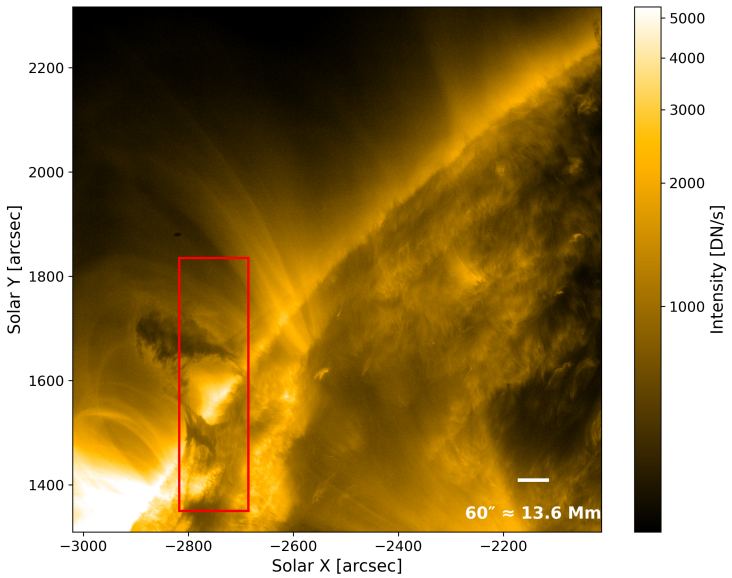

Figure 2.3: The prominence at 05:52:57 UT, 15 April 2023, observed by EUI/HRI$_{\mathrm{EUV}}$ 17.4 nm. The red rectangle shows the region observed by SPICE in Figure 2.2. The details of structures are slightly different from Figure 2.2 because of the difference of observation time (Figure from Zhang et al. (2026a)).

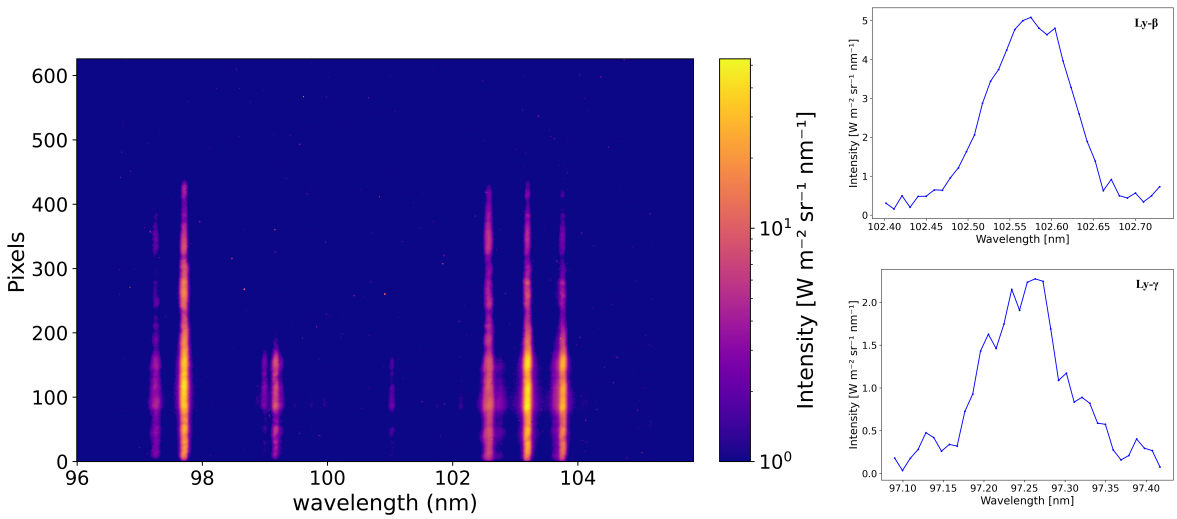

Figure 2.4: Left: The LW channel observation of SPICE during pre-eruption phase at 07:37:39 UT. The slit position is the same as the blue cut in Figure 2.2. Right: The Lyman β and Lyman γ line profiles are from the green cross in Figure 2.2 (Figure from Zhang et al. (2026a)).

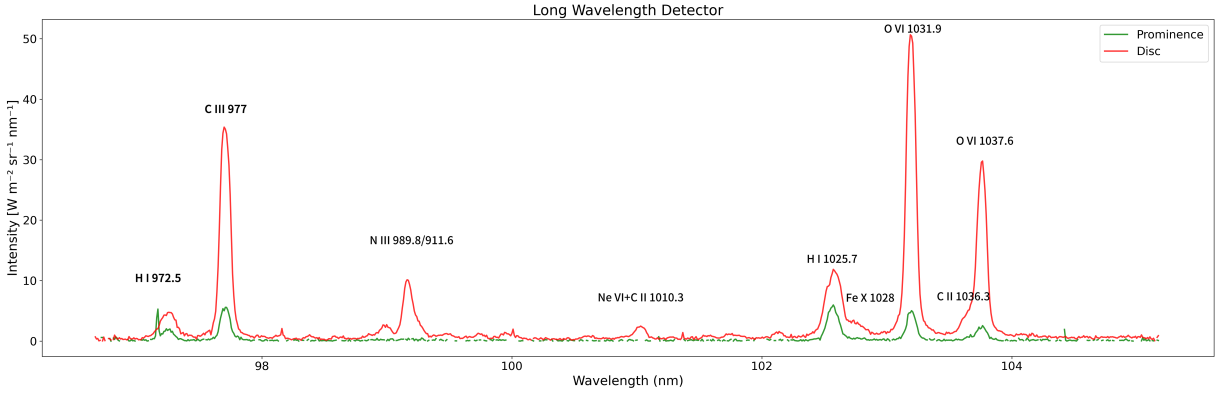

Figure 2.5: The spectrum of the LW channel during pre-eruption phase at the green cross and the red cross in Figure 2.2. Lines wavelengths are in Å (Figure from Zhang et al. (2026a)).

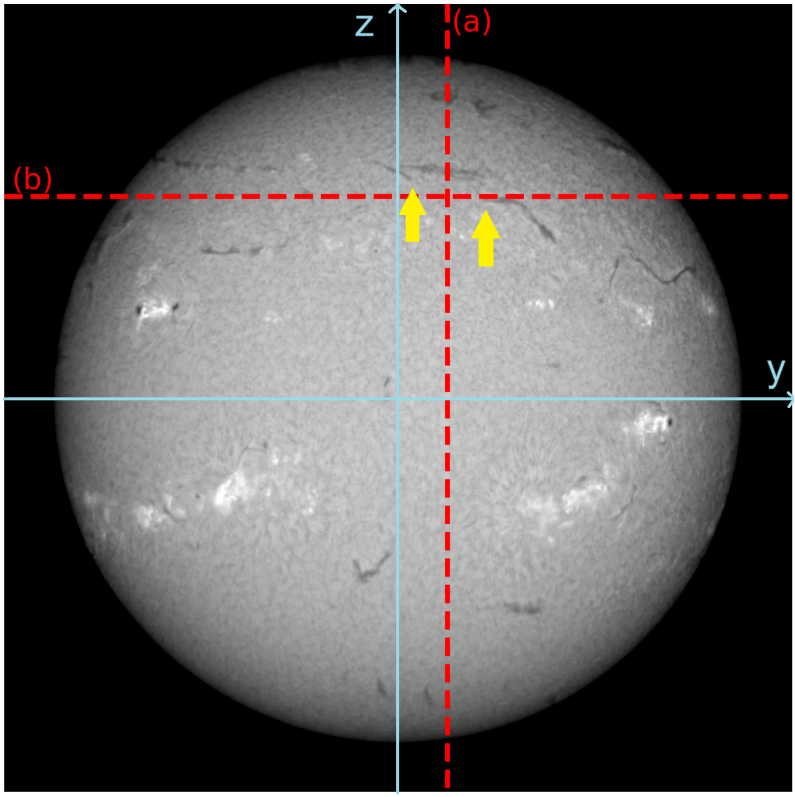

Figure 2.6: Hα image of El Teide at 10:07 UT. The yellow arrows point to the prominence we study. The blue lines show the coordinate we use in the analysis and the red dashed lines show the cross-sections we analyse (Figure from Zhang et al. (2026a)).

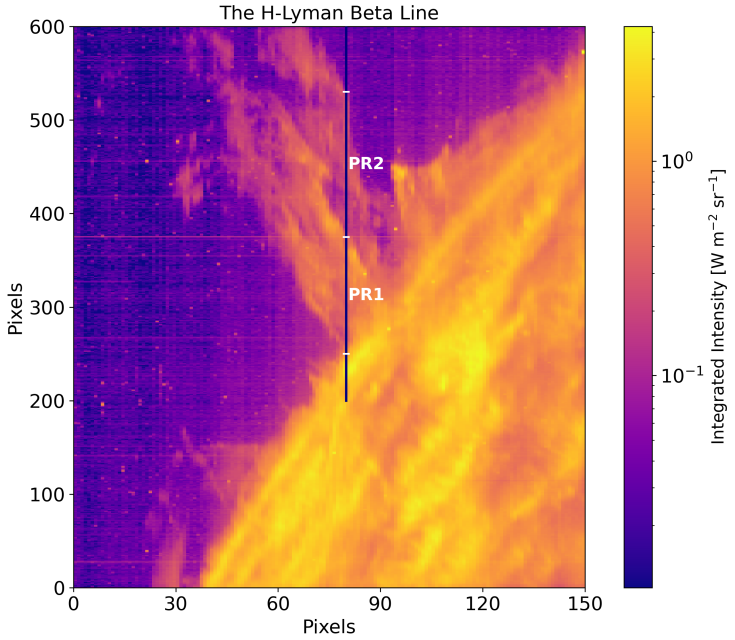

Figure 2.7: The SPICE observation of the integrated intensity of the Lyman β from 08:13 - 11:58 UT, 15 April 2023. 'PR' is the abbreviation of 'Prominence Region' (Figure from Zhang et al. (2026a)).

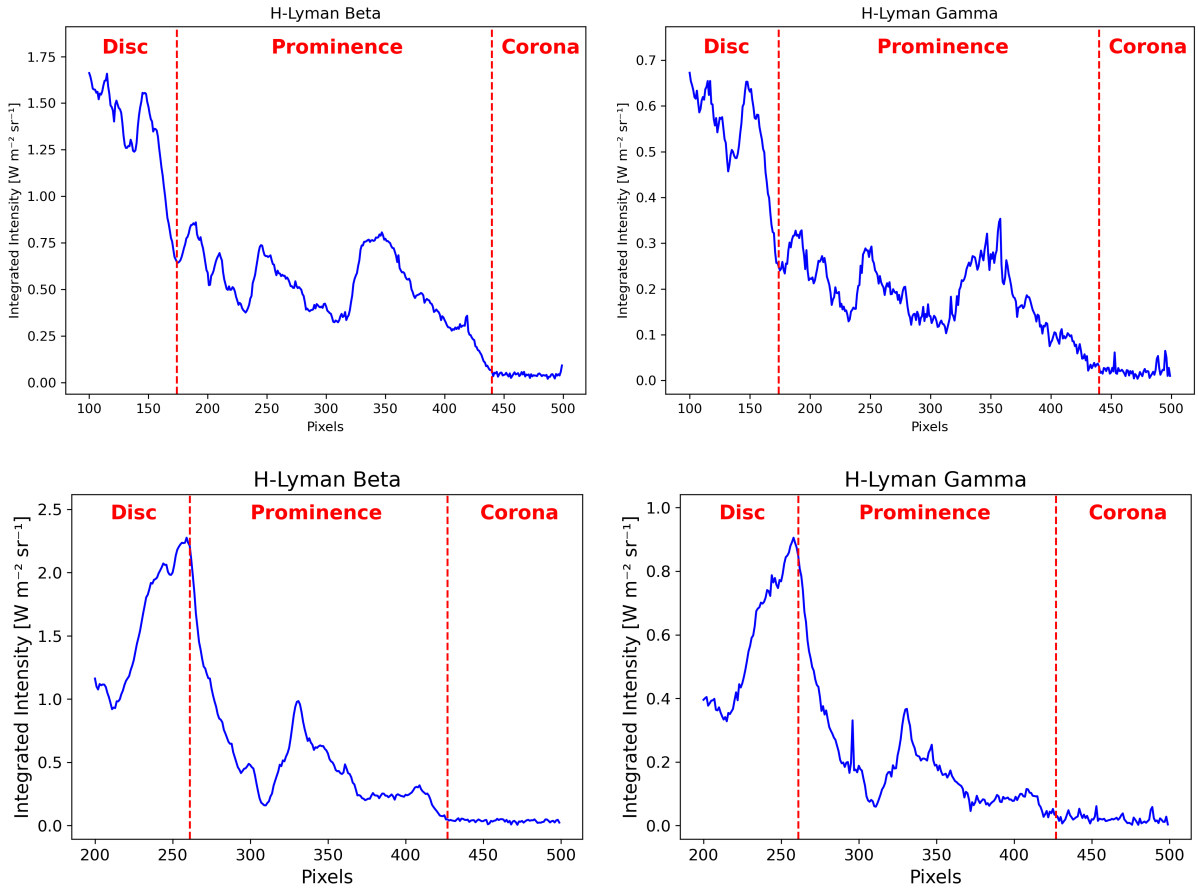

Figure 2.8: Top: The integrated intensity along the blue cut (x=5) for Lyman β and Lyman γ lines during pre-eruption phase. Bottom: The integrated intensity along the green dashed cut (x=25) for Lyman β and Lyman γ lines during pre-eruption phase (Figure from Zhang et al. (2026a)).

cross is at the location of maximum intensity along the disc region of the cut. Figure 2.5 shows the spectrum of the LW channel at the location of the green and red cross in Figure 2.2. In the right side of Figure 2.4, we can see the Lyman β and Lyman γ line profiles from the green cross.

Figure 2.6 shows the Hα image of El Teide at 10:07 UT. From GONG Hα observations, we know that the start time of the eruption is around 10:00 UT. Figure 2.7 shows the prominence in the Lyman β line during the eruption. The Lyman γ line was not observed during the eruption. From SPICE data we can infer that the altitude range of the prominence during the rasters observing both the pre-eruption and eruption time periods was about 20000 km $\sim$ 60000 km.

2.1.3 Integrated Intensity

To investigate the spatial variation of the prominence emission, we analysed the integrated intensity of the Lyman β and Lyman γ lines along the blue cut indicated in Figure 2.2. The intensity is obtained by performing a standard integration of the spectral intensity over 0.17 nm from central wavelength of each line at every spatial pixel along the cut. The value of 0.17 nm

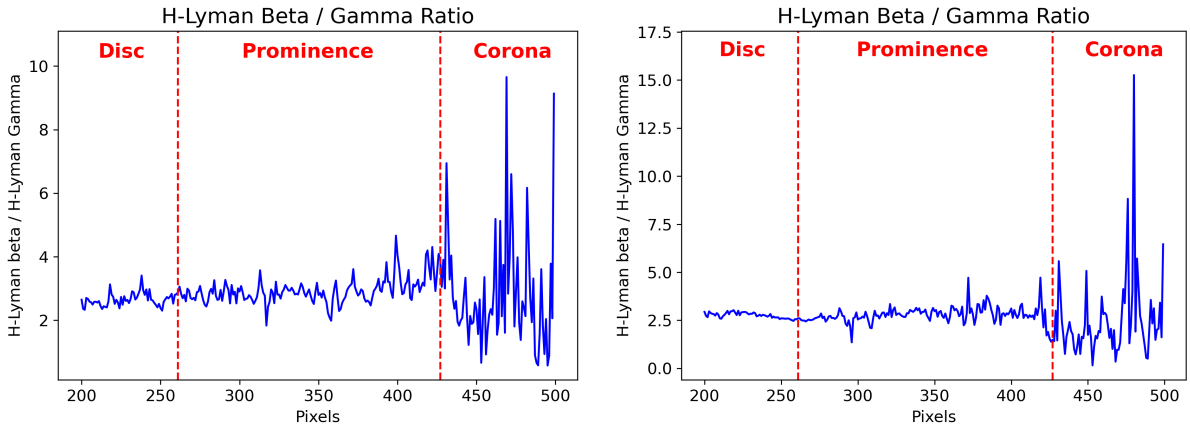

Figure 2.9: The ratio of the integrated intensity of Lyman β and Lyman γ lines along the blue cut (x=5, left) and the green dashed cut (x=25, right) during pre-eruption phase (Figure from Zhang et al. (2026a)).

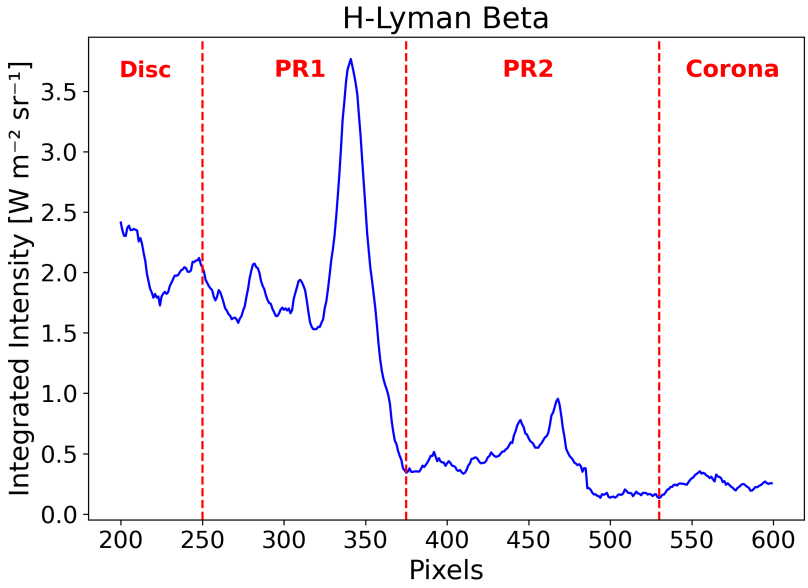

Figure 2.10: The integrated intensity along the blue cut in Figure 2.7 for Lyman β during eruption phase. PR1 and PR2 are two prominence regions showed in Figure 2.7 (Figure from Zhang et al. (2026a)).

Table 2.2: Mean integrated intensities and mean line widths of the Lyman β and Lyman γ lines measured in the disc and prominence regions before and during the eruption.

Phase	Region	Line	Integrated Intensity (W m^{-2} sr^{-1})	Observed Line Width (nm)	Intrinsic Line Width (nm)
Pre-eruption	disc	Lyman β	1.29	0.12	0.09
Pre-eruption	disc	Lyman γ	0.47	0.15	0.13
Pre-eruption	Prominence	Lyman β	0.52	0.13	0.10
Pre-eruption	Prominence	Lyman γ	0.19	0.18	0.16
Eruption	disc	Lyman β	1.50	0.09	0.05
Eruption	Prominence	Lyman β	1.07	0.09	0.05

was chosen as it corresponds to roughly half the width of the Lyman β window in data from the eruption raster, ensuring we capture the full profile. We do not use Gaussian fitting because the line profiles of Lyman β and Lyman γ deviate from Gaussian distributions due to the joint influence of noisy data, their intrinsically non-Gaussian shape when the lines are optically thick, and blending with other lines. The He II 102.527 nm line has a contribution about 1.5 % to the integrated intensity of Lyman β line (Ebadi et al., 2009). In this observation, actually, we cannot see the He II 102.527 nm line in most Lyman β line profiles.

The integrated intensity along the blue cut in Figure 2.2 for Lyman β and Lyman γ lines is shown in the upper panel of Figure 2.8. The solar disc region is on the left side of the first red dashed line and it shows relatively high intensity. The solar corona region is on the right side of the second red dashed line and it shows a very low intensity. This mainly reflects the higher temperature in the corona region that ionizes hydrogen or much higher density of the plasma in the disc region compared with the corona region. In the lower panel of Figure 2.8, we show the integrated intensity along the green dashed cut in Figure 2.2. From Figure 2.3 and Figure 2.7, we can infer that the angle of the prominence axis with the LOS of Solar Orbiter is small and the position of the farther away footpoint can be quite far away from the closer footpoint. Prominence materials along the green cut are behind most prominence materials along the blue cut. The projection effects along the line of sight should be different for the blue cut and the green dashed cut.

In Figure 2.9, we can see that there is a roughly constant ratio for the integrated intensity of Lyman β and Lyman γ lines in the Disc and the Prominence regions, which is around 2.5. This relatively stable ratio suggests that both lines are formed under similar radiative transfer conditions in these regions. It is a possible indication that both lines are formed through resonance scattering of the chromospheric radiation. In Heinzel et al. (2001), the ratio for the integrated intensity of Lyman β and Lyman γ lines in the Prominence regions is from 2.22 to 3.03. Our result is within this range. Also, the ratio between peak values of Lyman β and Lyman γ lines profiles can be derived from the SUMER atlas of Parenti et al. (2004, 2005) , which provides a value around 5 for the quiet sun and the prominence region. In Ebadi et al. (2009) , the ratio of the peak values of Lyman β and Lyman γ lines profiles is around 1.6. Since the shapes of

Lyman β and Lyman γ lines profiles are almost identical for each observation, we can assume the ratio of peak intensities is the same as ratios of integrated intensities for Lyman β and Lyman γ lines. So we can compare results in Parenti et al. (2004, 2005) and Ebadi et al. (2009) with Heinzel et al. (2001) and our results. Results in Parenti et al. (2004, 2005); Ebadi et al. (2009) are different from results from Heinzel et al. (2001) and ours. From Lemaire et al. (2012) , we know that the Lyman α to Lyman β irradiance ratio changes with solar activity. During minimum activity period, the standard deviation is around 30 %; during moderate activity period, the standard deviation is around 50 %. There is still no statistic for the solar maximum period.

These differences of ratios among Parenti et al. (2004, 2005) , Ebadi et al. (2009) , Heinzel et al. (2001) and us can be explained if the Lyman β to Lyman γ peak intensity ratio follows similar variations as the Lyman α to Lyman β irradiance ratio. Although no equivalent statistical study is available for the Lyman β/Lyman γ ratio, these three lines all belong to the Lyman series and are resonance transitions to the ground level. In prominences, their formation is strongly influenced by the incident radiation, so changes in the solar Lyman irradiance with solar activity are expected to affect Lyman β and Lyman γ in a broadly similar way to Lyman α and Lyman β.

Our observations are from 2023. Observations of Heinzel et al. (2001) and Parenti et al. (2004, 2005) are from 1999. These are during solar moderate activity period. The values should be within the normal variation range ($\sim$50 %). The value from Ebadi et al. (2009) is quite low compared with other papers. This is because their Lyman β line observation is from 2004 and their Lyman γ line observation is from 2001. The year of 2001 is during solar maximum. Both Lyman β and Lyman γ lines intensities in 2004 should be much lower than that in 2001 because of the reduction of the solar activity. Therefore, if we use Lyman β line observation in 2004 and Lyman γ line observation in 2001 to calculate the ratio, the value will be much lower than values calculated within the same year.

The ratio varies a lot in the Corona region in Figure 2.9. Such a large variation is likely due to the extremely low signal level in the corona, where noise, scattered light, small changes in optical thickness, or weak emission can strongly affect the ratio.

It should also be noted that the observed prominence pixels are not necessarily filled only by cool prominence plasma. Because the prominence filling factor can be small and the fine structure is not fully resolved, each spatial pixel may contain a mixture of prominence material and background coronal emission. Therefore, the ratio measured in the prominence region should be regarded as a spatially averaged quantity. However, since Lyman β and Lyman γ lines are hydrogen lines and the signal in the selected prominence region is much stronger and more coherent than in the surrounding corona, the measured ratio is expected to be dominated by the cool prominence plasma rather than by coronal emission.

We do not assign a formal uncertainty to this ratio, mainly because in low-signal regions both the Lyman β and Lyman γ integrated intensities can be close to zero. The division of two small

quantities makes the ratio highly sensitive to small absolute fluctuations from noise, scattered light, and residual background.

We also investigate the spatial variation of the prominence emission of the Lyman β line during eruption phase. In Figure 2.10, we can see how integrated intensity changes along the blue cut in Figure 2.7. In Figure 2.7, some pixels in prominence even have larger intensities than the disc region. This suggests that during the eruption, additional heating or increased column density of hydrogen can temporarily make the prominence brighter than the solar disc in Lyman β line. From Figure 2.7, we can see that Prominence Region 1 and Prominence Region 2 seem to belong to different parts located at different positions with respect to the plane of sky. Also in Figure 2.3, we can see that the footpoint of Prominence Region 2 is behind the Prominence Region 1. The integrated intensity of prominence region 1 is larger than prominence region 2. The difference may come from projection effects and different optical thickness along the line of sight. The integrated intensity of the Lyman β line in prominence region 1 during the eruption phase is generally larger than that during the pre-eruption phase. This is consistent with the expectation that eruption processes lead to enhanced plasma heating, mass motions, and possibly compression, all of which can increase line emissivity. But the integrated intensity of the Lyman β line in prominence region 2 is even lower than that during the pre-eruption phase. This lower intensity may also result from a lower density, different optical thickness or stronger Doppler dimming due to the eruptive velocity.

If we compare the Lyman β line profiles of Figure 2.11 and Figure 2.12 during the pre-eruptive phase, we can find that the peak values of Lyman β line profiles along the blue cut is about 1.5 times larger than the green cut. The peak value of Lyman β line is around 6.5 W m^{-2} sr^{-1} nm^{-1} along the blue cut and 4.2 W m^{-2} sr^{-1} nm^{-1} along the green cut . As discussed above, the difference may come from projection effects along the line of sight as the two cuts belong to different parts located at different positions with respect to the plane of sky. In Parenti et al. (2004, 2005), the peak value of Lyman β line in prominence regions is also around 6.5 W m^{-2} sr^{-1} nm^{-1}.

We have provided mean integrated intensities and mean line widths of the Lyman β and Lyman γ lines measured in the disc and prominence regions before and during the eruption in Table 2.2. In general, the integrated intensity of the eruptive prominence is much higher than the integrated intensity of the quiescent prominence shown in Heinzel et al. (2001). In Heinzel et al. (2001), the mean integrated intensities of several prominences are 0.22–0.70 W m^{-2} sr^{-1} for Lyman β line and 0.04–0.18 W m^{-2} sr^{-1} for Lyman γ line. The mean integrated intensities of the prominence region of two cuts we study during the pre-eruption phase are 0.52 W m^{-2} sr^{-1} for Lyman β line and 0.19 W m^{-2} sr^{-1} for Lyman γ line. The values are close to the May 28, 1999 prominence mentioned in Heinzel et al. (2001), which is low and dense. In Vial et al. (2007), the integrated intensities of the prominence region have ranges of 0.027–0.237 W m^{-2} sr^{-1} for Lyman β line. Values of Vial et al. (2007) come from the SUMER observation in 2005, which is closer to solar minimum. On the other hand, our observations and those of Heinzel et al.

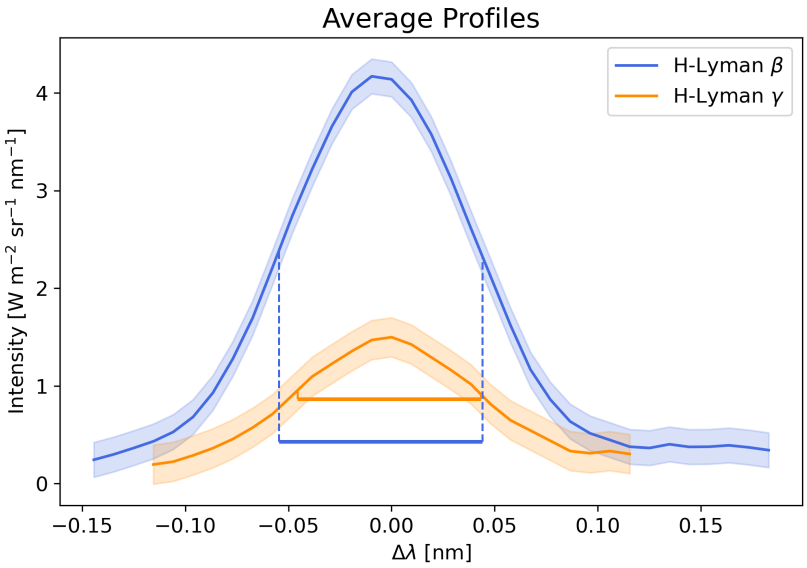

Figure 2.11: The average profiles of Lyman β and Lyman γ lines of Prominence Region during pre-eruption phase along the green dashed cut in Figure 2.2. The centre wavelength is 102.57 nm and 97.25 nm, respectively. The shaded regions show the estimated profile uncertainties estimated by the standard deviation of the corona region intensity, while the dashed lines and horizontal lines indicate the line widths defined between CDF=0.12 and CDF=0.88.

(2001) are closer to solar maximum. This could explain why the integrated intensities of the prominence region for Lyman β line in Vial et al. (2007) are much smaller. The 8th Orbiting Solar Observatory (OSO-8) observation in Vial (1982) shows that the integrated intensities of the prominence region for Lyman β line are 0.44–0.55 W m^{-2} sr^{-1}. The OSO-8 observation in Vial (1982) is also during solar minimum, but the values are far from Vial et al. (2007). The lower values reported by Vial et al. (2007) should not be attributed solely to the phase of the solar activity cycle. Although the global level of solar activity can influence the incident chromospheric radiation, the intensity of an individual prominence also depends strongly on local physical conditions, such as density, temperature, and optical thickness, as well as instrumental calibration. During the eruption phase, the mean integrated intensity in Lyman β of the prominence region of the blue cut we study is 1.07 W m^{-2} sr^{-1}. This value is obviously larger than all the quiescent prominences shown in Heinzel et al. (2001), Vial et al. (2007) and Vial (1982). Enhanced plasma heating, mass motions, and an increase in plasma density due to compression associated with the reconfiguration of the magnetic field during the eruption may contribute to the increased integrated intensity.

2.1.4 Line Width

Here we discuss the properties of the observed profiles without performing a full deconvolution from the instrumental profile because we don't have enough information about the instrumental

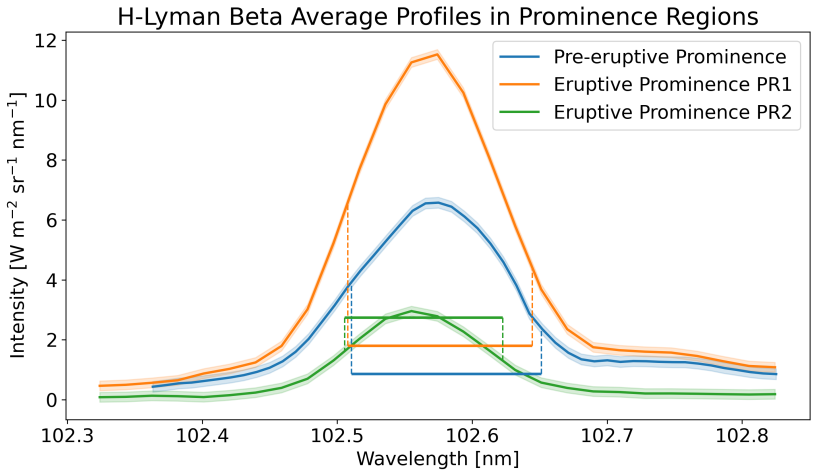

Figure 2.12: The average profiles of Lyman β in the prominence region along the blue cuts during the pre-eruption phase and eruption phase. The shaded regions show the estimated profile uncertainties estimated by the standard deviation of the corona region intensity, while the dashed lines and horizontal lines indicate the line widths defined between CDF=0.12 and CDF=0.88.

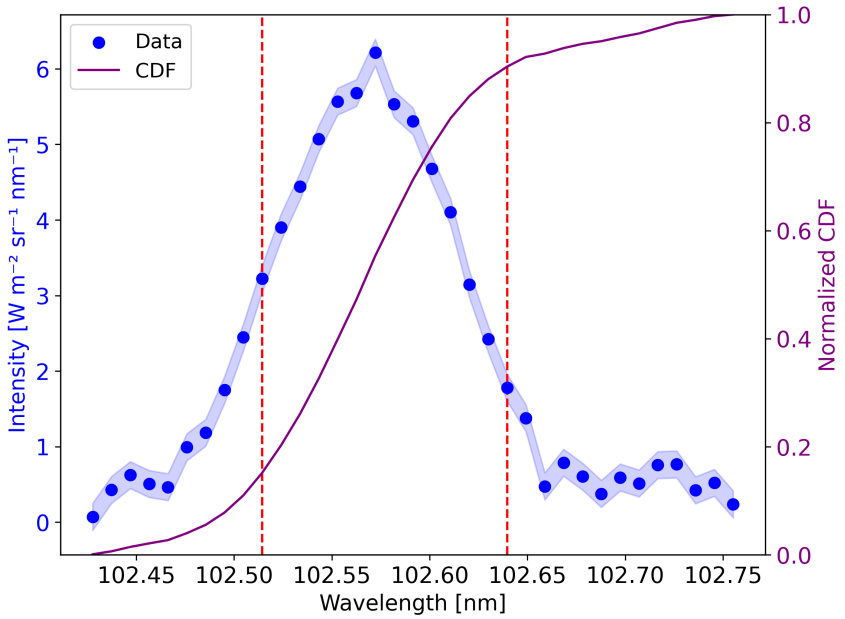

Figure 2.13: The method of line width calculation. CDF is the cumulative distribution function. The two red dashed lines lie in the locations of CDF=0.12 and CDF=0.88. The distance of the two red dashed lines is the line width of this line profile. The blue dots show data points and CDF is shown by the purple line. The shaded regions show the estimated profile uncertainties estimated by the standard deviation of the corona region intensity.

profile of the SPICE instrument. We provide values for the measured line widths before and after applying a simple correction for the instrumental width. The average profiles of Lyman β and Lyman γ lines in the Prominence Region along the green dashed cut (x=25) in Figure 2.2 during the pre-eruption phase are shown in Figure 2.11. In general, the line profile of Lyman β have higher intensity and wider line shape than the line profile of Lyman γ.

In Figure 2.12, we can see that the line profiles of eruptive prominence region 1 have generally larger intensity and wider line shape than that during the pre-eruption phase. This may indicate that eruptive prominence region 1 has either higher density or higher temperature along the line of sight. The broadening could be related to the change of temperature among different rasters or motions along LOS. In Figure 2.12, we also compare the average profiles of Lyman β in the prominence region during the pre-eruption phase and eruption phase. The eruptive prominence region 1 has higher intensity and broader line width than pre-eruption phase, which is as we expected. But the eruptive prominence region 2 has lower intensity and narrower line width than pre-eruption phase. The eruptive prominence region 2 also shows some blue-shift in Lyman β line profile.

We calculate the line width of the Lyman β and Lyman γ profiles from SPICE in order to diagnose the plasma conditions, since the line width carries information on both thermal and non-thermal broadening. To estimate the line widths of the Lyman β and Lyman γ lines we adopt the quantile method, which has been successfully applied in recent IRIS studies (Kerr et al., 2015; Ruan et al., 2018). This method relies on constructing the cumulative distribution function (CDF) of the line profile. The line centre is then given by the 50% quantile. Compared with standard Gaussian fitting, the quantile method is more robust against noise and line asymmetries, and thus particularly well-suited for our data where the observed line profiles deviate from a simple Gaussian shape. In this work, the CDF is constructed directly from the observed line profile within the selected wavelength window, without subtracting a local background. Therefore, the measured width represents an effective width of the observed spectral feature in that window. Signals near the edges of the window can influence the normalized CDF. These edge signals may come from weak neighbouring lines blends or noise rather than from the target Lyman line itself. But their relative contributions cannot be separated quantitatively with the present data.

The line widths reported in this section should be regarded as effective observed widths, not as direct measurements of thermal or turbulent velocity. Although line widths can in principle be related to thermal and non-thermal broadening, the interpretation is complicated here by line-of-sight velocity, unresolved fine structures, and uncertainties in the SPICE instrumental profile and PSF.

The line width measurement by the quantile method can be chosen so that it conveniently reproduce the full-width at half-maximum of a Gaussian profile. We solve the equation derived from the ratio of two functions involving a Gaussian distribution with a mean $\mu = 0$ and cal-

culate the corresponding CDF values. The probability density function (PDF) of a Gaussian distribution with mean $\mu = 0$ and standard deviation σ is given by:

$$f(x) = \frac{1}{\sigma\sqrt{2\pi}} \exp\left(-\frac{x^2}{2\sigma^2}\right) \tag{2.1}$$

x is the variable that follows Gaussian distribution. At half maximum intensity, $f(x)/f(0) = 0.5$, so

$$\exp\left(-\frac{x^2}{2\sigma^2}\right) = 0.5 \tag{2.2}$$

This could be simplified as

$$x^2 + 2\sigma^2 \ln(0.5) = 0 \tag{2.3}$$

The Gaussian CDF for a given x is defined as:

$$\mathrm{CDF}(x) = \frac{1}{2}\left(1 + \mathrm{erf}\left(\frac{x-\mu}{\sqrt{2}\sigma}\right)\right) \tag{2.4}$$

In Equation 2.1.4, erf is error function. After substituting the solutions for x in Equation 2.3 into this CDF formula, we can find the corresponding CDF values at the half maximum intensity positions. The results are 0.12 and 0.88.

By identifying the locations of CDF=0.12 and CDF=0.88, we get the line width (Figure 2.13). The line width before the eruption for the Lyman β and Lyman γ lines is shown in Figure 2.14. Considering the instrumental broadening $\mathrm{L_{inst}}$, values that are lower than $\mathrm{L_{inst}}$ have been changed to the value of $\mathrm{L_{inst}}$.

The average line widths in the prominence region (y-pixel 326 to 426) are 0.13 nm for the Lyman β line and 0.18 nm for the Lyman γ line. The average line widths in the disc region (y-pixel 0 to 100) are 0.12 nm for the Lyman β line and 0.15 nm for the Lyman γ line. We can calculate the intrinsic line width after accounting for the instrumental broadening ($\mathrm{L_{inst}}$ = 0.0775 nm) of SPICE's long-wavelength channel (Young et al., 2025). The average line widths in the prominence region are 0.10 nm for the Lyman β line and 0.16 nm for the Lyman γ line after correction. The average line widths in the disc region are 0.09 nm for the Lyman β line and 0.13 nm for the Lyman γ line after correction. The broader width of the Lyman γ line compared to Lyman β can be attributed to the smaller signal-to-noise ratio of the Lyman γ line. The noisy data can affect the calculation of the line width and usually enlarges the value. The effect is larger in the Lyman γ line because of the lower signal to noise ratio of the Lyman γ line.

As shown in Figure 2.14, the measured Lyman γ widths are systematically larger than the Lyman β widths over much of the field of view, so this difference is a clear tendency in the observed profiles. However, a formal uncertainty is not assigned here because the measured

widths are affected by several coupled factors, including signal-to-noise level, weak blends, unresolved line-of-sight velocity structures, and uncertainties in the SPICE instrumental profile. Therefore, the broader Lyman γ widths should be interpreted as a robust observational tendency in the effective widths, but not necessarily as direct evidence that Lyman γ has a larger intrinsic thermal or non-thermal width than Lyman β.

This result shows that the intrinsic line width of the prominence and disc regions are generally similar. This suggests similar line formation conditions, like temperature, and optical thickness of both lines, for the two different regions.

The Lyman β line width observed by SPICE during the eruption is shown in Figure 2.15. Values that are narrower than L_{inst} have also been changed to the value of L_{inst}. The two white rectangles represent the prominence region and the disc region. The average line width in the prominence region is 0.09 nm and the average line width in the disc region is 0.09 nm. After accounting for the instrumental broadening, the intrinsic line width of the two regions is 0.05 nm.

In Heinzel et al. (2001), the line widths of Lyman β and Lyman γ are around 0.05–0.06 nm (the instrumental broadening of Lyman lines was neglected) for the quiescent prominences observed on May 28 and June 2, 1999, by SUMER. In Tian et al. (2009) , the line width of Lyman β is also around 0.05 nm. However, Tian et al. (2009) did not present this quantity as an intrinsic line width corrected for instrumental broadening. These values in Heinzel et al. (2001) and Tian et al. (2009) are much less than our results. This may suggest that the plasma conditions in quiescent prominences that are close to eruption can be quite different from those that are not, leading to different line-broadening effects. However, The discrepancy may also arise from instrumental effects and different definitions of line width. This physical interpretation therefore cannot be confirmed solely from the present data. The discrepancy may also be influenced by the remaining relative uncertainties in the instrumental profiles of SPICE compared with other instruments such as SUMER on SOHO. Future modelling would allow us to determine whether there are narrower profiles in the eruption phase.

2.1.5 Line Profile

We present the spatial and temporal evolution of Lyman β and Lyman γ lines profiles in this section, which might provide information for diagnostics of the plasma conditions. Figure 2.16 shows Lyman β and Lyman γ lines spectra before the eruption from image of the detector for the exposures at the raster position x=5, 10, 15, 20, 25 in Figure 2.2. The Lyman β line spectra during eruption from images of the detector for the exposures at the raster position x=80, 82, 84, 86, 88 are shown in Figure 2.17. The differences between the prominence region and disc region in Figure 2.17 seem to be more pronounced than those in Figure 2.16. The pre-eruption and eruption rasters images were obtained at different raster positions and cover different pixel ranges, so the pixel coordinates and apparent disc edge positions are not directly comparable. Therefore, Figure 2.17 is mainly to demonstrate that, within the eruption raster, the contrast

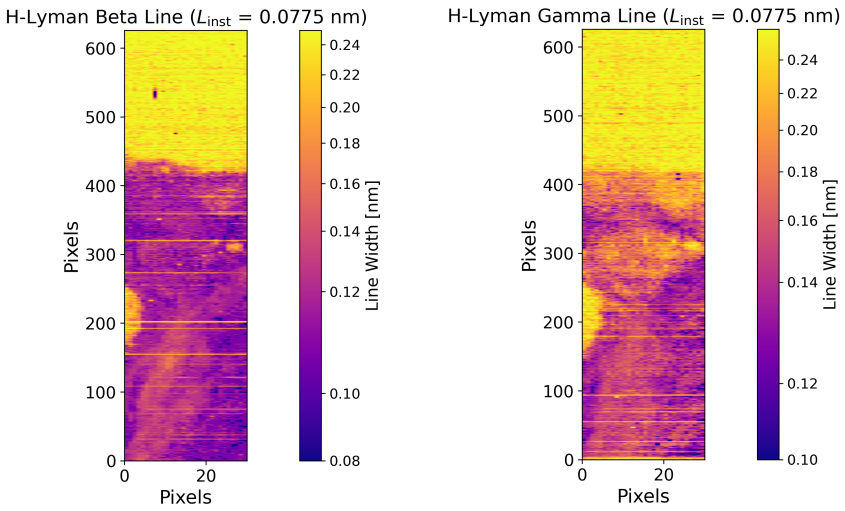

Figure 2.14: The line width of Lyman β and Lyman γ lines profiles during pre-eruption phase (Figure from Zhang et al. (2026a)).

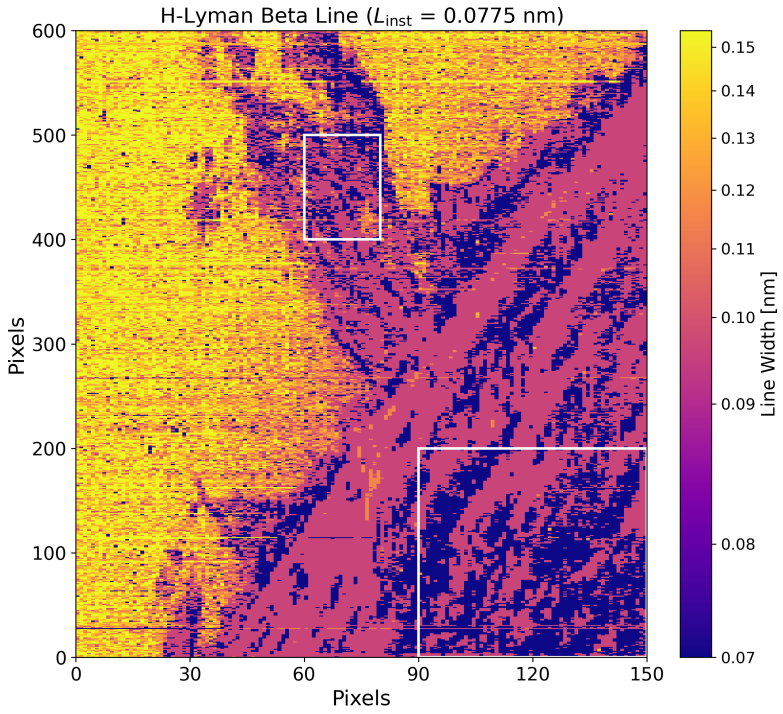

Figure 2.15: The line width of Lyman β lines profiles during eruption phase. The white rectangles show locations where we take samples for the disc region and the prominence region (Figure from Zhang et al. (2026a)).

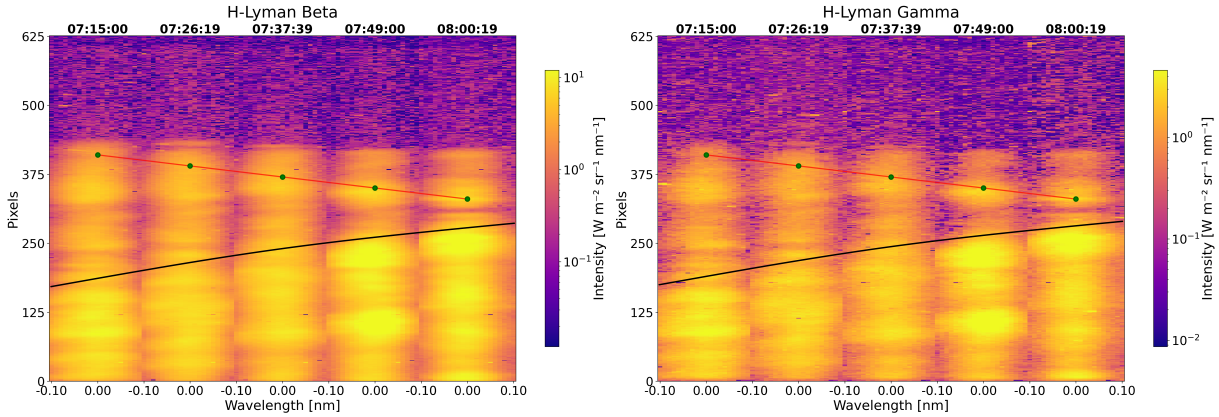

Figure 2.16: The Lyman β and Lyman γ lines spectra before the eruption from image of the detector for the exposures at the raster position x=5, 10, 15, 20, 25 in Figure 2.2 during pre-eruption phase. The centre wavelength is 102.57 nm and 97.25 nm. The green dots and red lines refer to the positions of line profiles in Figure 2.18. The black curve is the boundary of the solar disc (Figure from Zhang et al. (2026a)).

between the disc and the prominence regions is more pronounced.

Figure 2.18 shows line profiles with details of spatial and temporal evolution before the eruption. The reference line centre (the red dashed lines) are taken from the CDF=0.5 position of the average profile of the disc region (y-pixel 0-100 for all 30 slits in Figure 2.2). The centre wavelength is 102.57 nm and 97.25 nm. The Lyman γ line exhibits relatively more small-scale variations compared to Lyman β, although part of these features could be influenced by the difference in signal-to-noise ratio between the two lines. The temporal evolution is also more pronounced in the Lyman γ line spectra. Weak He II blends may contribute to these wavelength windows, but they cannot be identified or separated reliably in the present spectra because of the noise level. The lower signal-to-noise ratio of Lyman γ means that small-scale variations in the Lyman β/Lyman γ ratio should not be over-interpreted. The physical comparison with Lyman α/Lyman β is only qualitative.

Figure 2.19 shows Lyman β line profiles with details of spatial and temporal evolution during the eruption. The reference line centre (the red dashed line) is taken from the CDF=0.5 position of the average profile of the disc region (the lower right white rectangle in Figure 2.15). The centre wavelength is 102.56 nm. The pixels we choose in Figure 2.19 generally show higher intensity compared with Lyman β line profiles in Figure 2.18. We have calculated the Doppler shift of these line profiles. Most of the values are below the SPICE resolution limit (approximately 30 km s^{-1}) (Plowman et al., 2025). We can conclude that no significant line-of-sight velocity can be detected.

Overall, the spectral profiles indicate that the eruption enhances spatial and temporal variations in line intensity and line-of-sight motions, reflecting dynamic changes in plasma conditions within the prominence.

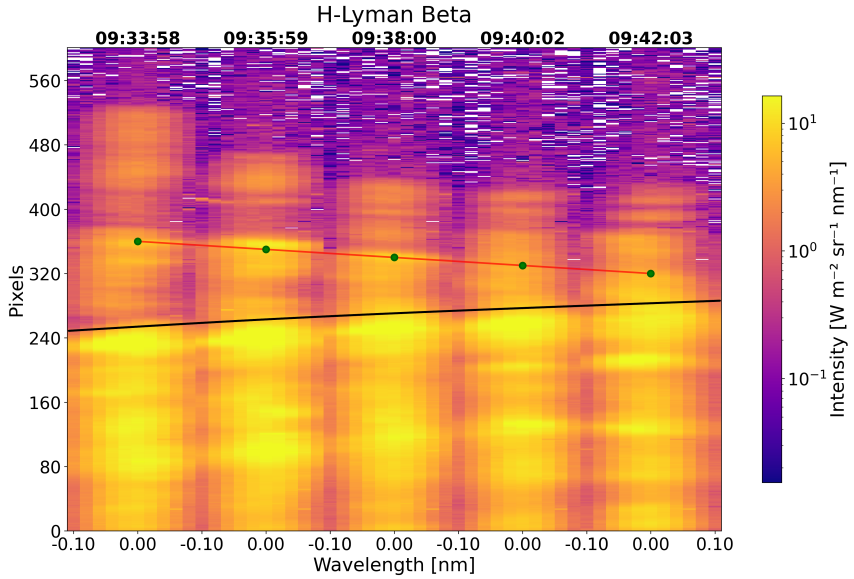

Figure 2.17: The Lyman β lines spectra during eruption from image of the detector for the exposures at the raster position x=80, 82, 84, 86, 88 in Figure 2.7 during eruption phase. The centre wavelength is 102.56 nm. The green dots and the red line refer to the positions of line profiles in Figure 2.19. The black curve is the boundary of the solar disc (Figure from Zhang et al. (2026a)).

2.1.6 Fitting of Line Profile

We have tried to fit line profiles of the Lyman β line. The Lyman γ line profile in this observation is too noisy and obviously, it is not suitable for a fitting test. Since the Lyman β line is approximately optically thin line and the shape is near Gaussian, we use Gaussian function to fit the line profile. We want to distinguish the He II line with the Lyman β line. From Parenti et al. (2005), we know that the He II line is 0.42 nm away from the Lyman β line. Therefore, we use Equation (2.5) to fit line profiles of the Lyman β line from SPICE observations.

$$f(x) = d + a_1 \exp\left[-\left(\frac{x-(b-0.42)}{c_1}\right)^2\right] + a_2 \exp\left[-\left(\frac{x-b}{c_2}\right)^2\right] \tag{2.5}$$

In Equation (2.5), x denotes the independent variable and $f(x)$ is the corresponding function value. The parameter d represents a constant background value. The coefficients a_1 and a_2 correspond to the amplitudes of the two Gaussian components. The parameter b defines the central position of the second Gaussian, while the first Gaussian is centred at $b-0.42$. The first Gaussian component is the He II line and the second Gaussian component is the Lyman β line. The parameters c_1 and c_2 describe the widths of the two Gaussian components, respectively.

From Figure 2.20, we can see that the fitting result of a line profile from a prominence region is roughly consistent with the data points. Nevertheless, fitting results are quite sensitive to the initial values of all parameters. Also, the two Gaussian components are not convincing. The first component is too large compared with the second component. The data resolution and effect of

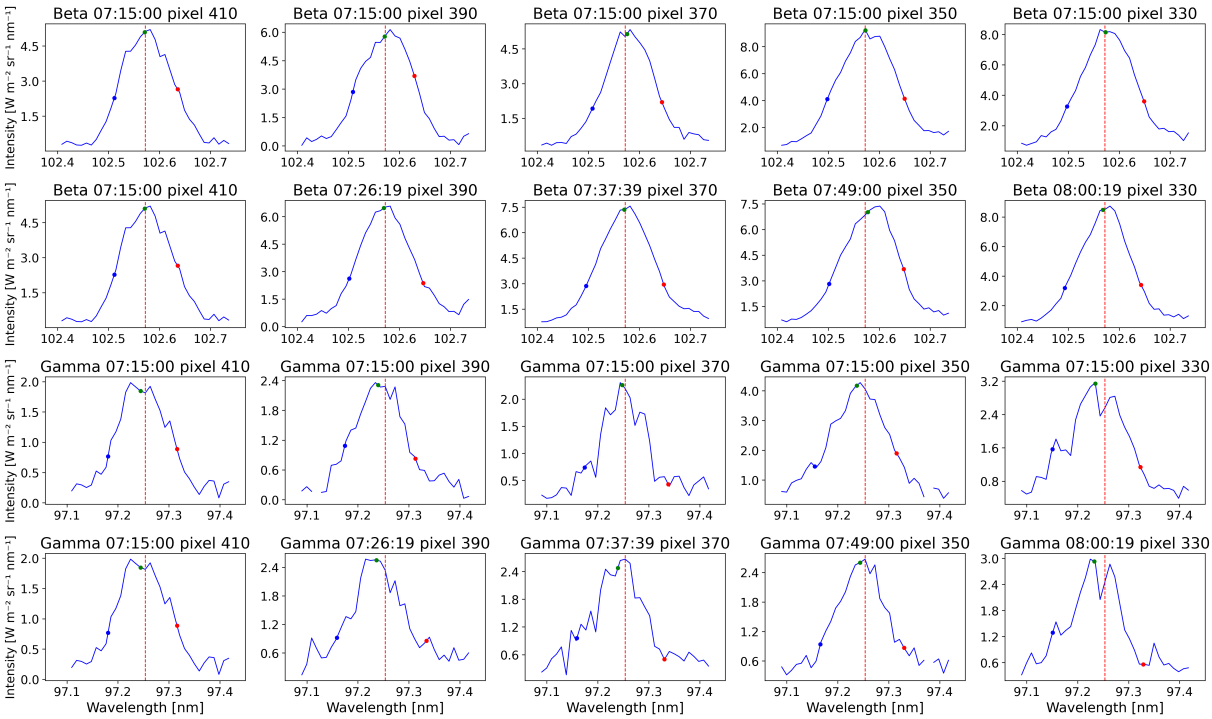

Figure 2.18: The Lyman β and Lyman γ lines profiles in the prominence region from SPICE observation before the eruption. The first and second rows are the Lyman β line profiles. The first row is pixel 410, 390, 370, 350 and 330 at 07:15:00 UT in Figure 2.16. The second row is pixel 410, 390, 370, 350 and 330 from 07:15:00 UT to 08:00:19 UT, which is the same as the connection order of green points in Figure 2.16. The third and forth rows are the Lyman γ line profiles. The time and location for these lines profiles are the same as the Lyman β line. The blue point is the location CDF=0.12, the green point is the location CDF=0.50, and the red point is the location CDF=0.88. The red dashed lines are x=102.57 nm in the Lyman β line profile and x=97.25 nm in the Lyman γ line profile. These values are taken from the CDF=0.5 position of the average profile of the disc region (y-pixel 0-100 for all 30 slits in Figure 2.2) (Figure from Zhang et al. (2026a)).

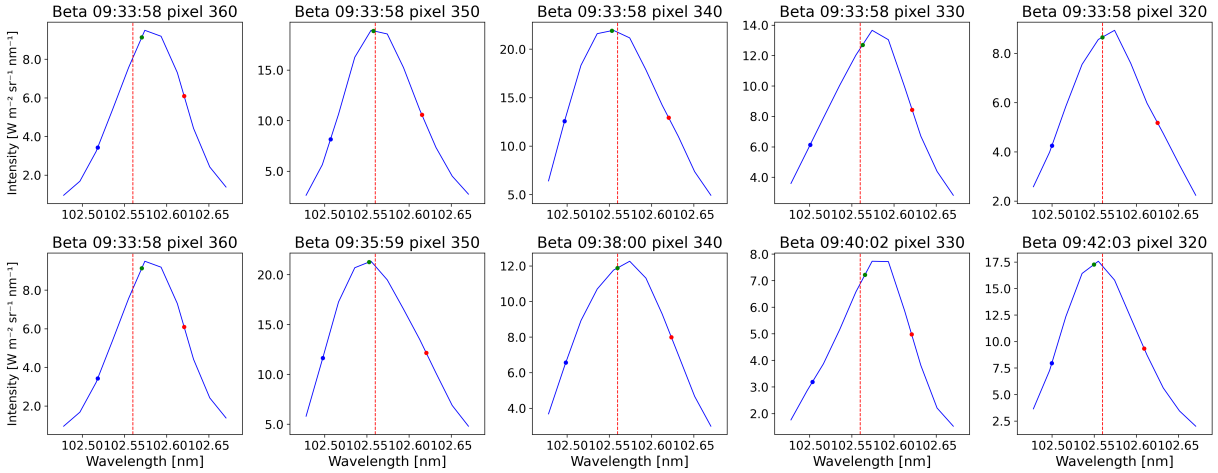

Figure 2.19: The Lyman β lines profiles in the prominence region from SPICE observation during the eruption. The first row is pixel 360, 350, 340, 330 and 320 at 09:33:58 UT in Figure 2.17. The second row is pixel 360, 350, 340, 330 and 320 from 09:33:58 UT to 09:42:03 UT, which is the same as the connection order of green points in Figure 2.10. The blue point is the location CDF=0.12, the green point is the location CDF=0.50, and the red point is the location CDF=0.88. The red dashed lines are x=102.56 nm. The value is taken from the CDF=0.5 position of the average profile of the disc region (the lower right white rectangle in Figure 2.15) (Figure from Zhang et al. (2026a)).

the noisy data affect the fitting process. We cannot distinguish the He II line component by the double Gaussian fitting.

2.2 Radial velocity estimation

Although Doppler shift of these line profiles is hard to determine, we still need to estimate the radial velocity by the observation as it is an important parameter in the Non-LTE modelling which we will present in the next chapter and Lyman lines may be sensitive to Doppler dimming. Because there is no adequate off-limb observation of the pre-eruption and eruption phases to allow us to estimate the radial velocity for this event, we have to rely on on-disc images that show these phases. We propose a new way of calculating the radial velocity from images. We can obtain the radial velocity at a certain time by 2 images of an instrument with the same point of view. This technique is fast and convenient only relying on a few assumptions.

2.2.1 Direction of the eruption

We need to derive the direction of the eruption to understand how the radial velocity is projected in the 2D image in Figure 2.6. According to McCauley et al. (2015), 75 % of filament eruptions are radial. The rarity of non-radial solar eruptions can be attributed to the negative role of magnetic asymmetry in eruption initiation. Magnetic asymmetry inhibits, rather than facilitates, the

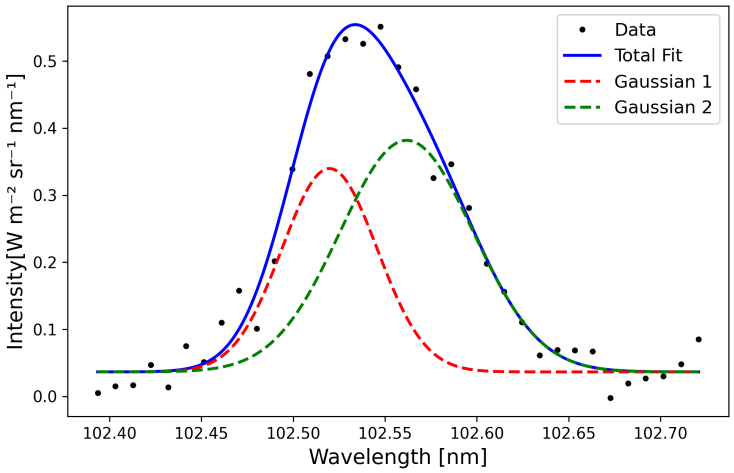

Figure 2.20: The double Gaussian fitting of the He II line and the the Lyman β line. The black points are data points from a prominence region. The blue solid curve is the fitting of the whole line profile. The red and green dashed lines are two Gaussian components of the double Gaussian fitting.

eruption process. Numerical simulations by Liu et al. (2024) demonstrate that as the asymmetry of the magnetic flux distribution increases, the eruption direction deviates further from the radial path, while the eruption intensity weakens. In cases of strong asymmetry, eruptions may not occur at all, explaining why non-radial eruptions are less frequent than radial ones. Therefore, it is reasonable to assume radial eruption. In Figure 2.6, from the Hα observation of El Teide at 10:07 UT, we identify the coordinates of two footpoints of this filament by choosing two points around the footpoints' area with similar intensity. Thus, we get the coordinates of the centre point of the filament and convert these to spherical coordinates.

We set the horizontal direction of the Hα image as the y-axis, the vertical direction of the 2D image is the z-axis, and the x-axis is outward from the plane and perpendicular to the other axes. The θ and ϕ angles are shown in Figure 2.21. The coordinates of the centre point of the filament footpoints (point P) projected in the $x = 0$ plane are (y,z). We find the relationship of y, z, θ, and ϕ from two cross-sections of the sphere in Figure 2.22. The left one is through the dashed line (a) and the right one is through the dashed line (b) in Figure 2.6. On the left side of Figure 2.22, the cross-section contains the z-direction and point P. On the right side of Figure 2.22, the cross-section is parallel to the xy-plane and contains point P.

We assume the point P is on the solar surface. There should be some error about height in making this assumption, but it is negligible compared with the relatively large value of solar radius. After this step, we get the eruption direction by a vector $\vec{OP} = (r,\theta,\phi)$ in the spherical coordinate. The point O is the solar centre.

So

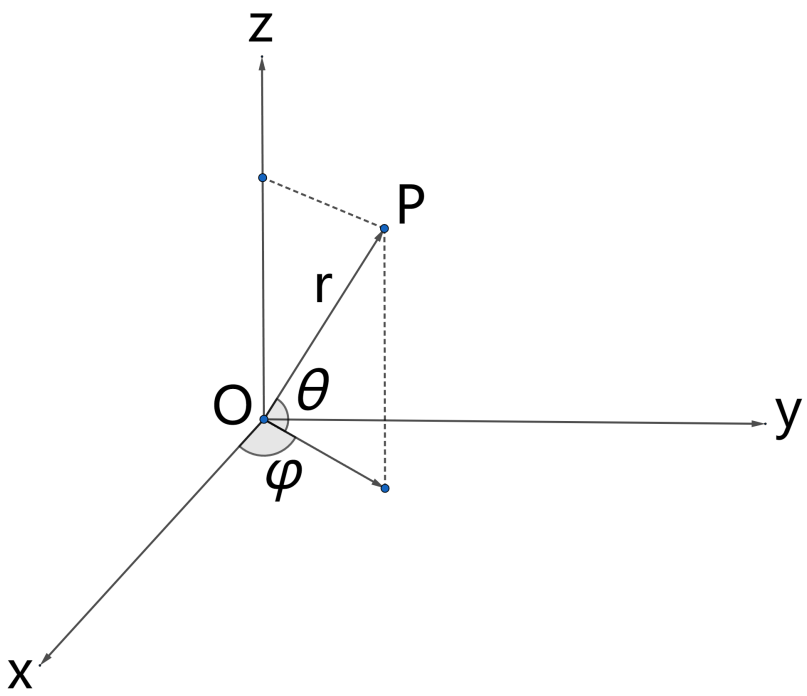

Figure 2.21: The illustration of the coordinates and angles (Figure from Zhang et al. (2026a))

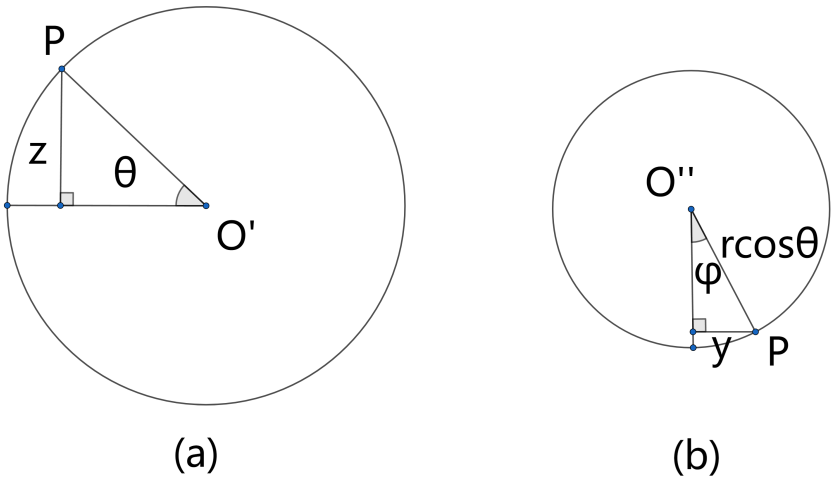

Figure 2.22: Two cross-sections of the sphere. The left one is through the dashed line (a) and the right one is through the dashed line (b) in Figure 2.6 (Figure from Zhang et al. (2026a)).

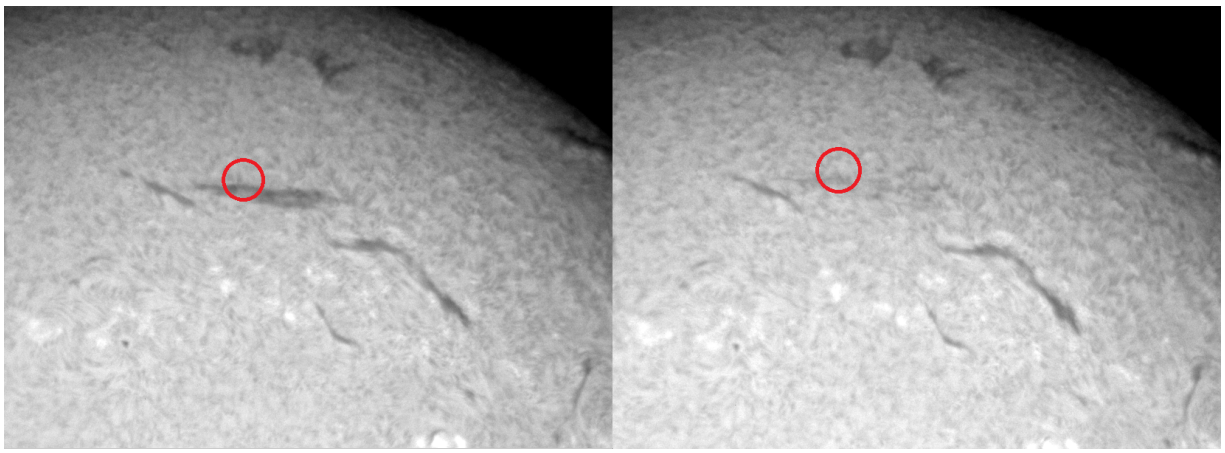

Figure 2.23: Hα image of El Teide at 09:57 UT (left) and 10:17 UT (right), April 15, 2023. The filament is in the same region as Figure 2.6. The red circle shows the feature we track (Figure from Zhang et al. (2026a)).

$$z = r\sin\theta \tag{2.6}$$
$$y = r\cos\theta\sin\phi \tag{2.7}$$

Then

$$\theta = \arcsin\left(\frac{z}{r}\right) \tag{2.8}$$
$$\phi = \arcsin\left(\frac{y}{r\cos\theta}\right) \tag{2.9}$$

2.2.2 Projection on 2D plane

Assume the radial velocity is $\vec{v} = (v_r, 0, 0)$ in spherical coordinates, or in Cartesian coordinates $\vec{v} = (v_x, v_y, v_z)$:

$$v_x = v_r\cos\theta\cos\phi \tag{2.10}$$
$$v_y = v_r\cos\theta\sin\phi \tag{2.11}$$
$$v_z = v_r\sin\theta \tag{2.12}$$

Also

$$\vec{v} = \vec{v}_x + \vec{v}_{yz} \tag{2.13}$$

where the projection of the radial velocity on the $y-z$ plane is:

$$\begin{aligned}\vec{v}_{yz} &= \vec{v} - \vec{v}_x \\ &= (v_r \cos\theta\cos\phi, v_r \cos\theta \sin\phi, v_r \sin\theta) \\ &\quad - (v_r \cos\theta\cos\phi, 0, 0) \\ &= (0, v_r \cos\theta \sin\phi, v_r \sin\theta) \end{aligned} \tag{2.14}$$

So

$$\left|\vec{v}_{yz}\right| = v_r \sqrt{(\cos\theta\sin\phi)^2 + (\sin\theta)^2}$$

Since the velocity v is assumed to be entirely in the radial direction

$$\left|\vec{v}_{yz}\right| = |\vec{v}| \sqrt{(\cos\theta\sin\phi)^2 + (\sin\theta)^2} \tag{2.15}$$

2.2.3 Calculation of radial velocity

We assume that the eruption is uniformly accelerated motion, and that different parts of the filament have the same speed during eruption. According to Zhang et al. (2001), constant acceleration rate fitting is not adequate for some events. Nevertheless, our calculation is only based on 2 images with a 20 min interval, which is a relatively short period. Therefore, we assume the acceleration in the initiation phase of CME is stable. This assumption should be reasonable. Since the filament began to erupt at 09:57 UT, we used 09:57 UT and 10:17 UT images to identify the radial velocity at 10:07 UT.

Figure 2.23 shows a feature that we can identify in the 09:57 UT and 10:17 UT images. After finding the coordinates of the circled features on these two images, the velocity of the filament eruption in the y-z plane can be calculated. Then, we can use the Equation 2.15 to obtain the radial velocity. 10:07 UT is the last time we could identify the radial velocity by the Hα observation of El Teide. This calculation shows that the radial velocity should be around 31 ± 7 km s^{-1} at 10:07 UT. The uncertainty of the result comes from the uncertainty of the location of the circled ends (about ± 7 pixels), which is ambiguous in Figure 2.23. There are uncertainties from other sources: (1) if the radial eruption assumption is not satisfied, the derived velocity would have error depending on the inclined angle to the radial direction; (2) if the uniform acceleration assumption is not satisfied, the derived velocity would have an error depending on the pattern of acceleration process.

We apply the same technique for the EUVI-A observation for this event as cross validation

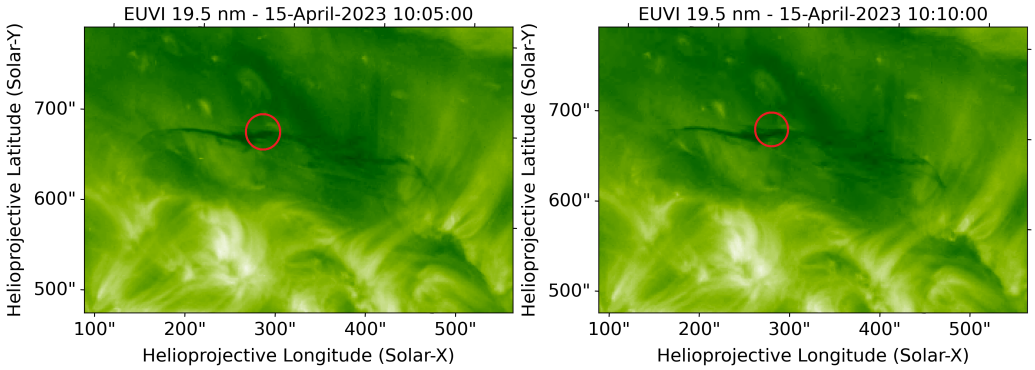

Figure 2.24: 19.5 nm observation of EUVI-A at 10:05 UT (left) and 10:10 UT (right), April 15, 2023. The filament is in the same region as Figure 2.6. The red circle shows the feature we track (Figure from Zhang et al. (2026a)).

(Fig. 2.24). This would be useful because STEREO is not on the Sun-Earth line on April 15, 2023. The result shows that the radial velocity should be around 44 ± 5 km s^{-1} at 10:07:30. The uncertainty of the result comes from the uncertainty of the location of the circled ends (about ± 5 pixels). This result is quite close to our calculation using the Hα observation of El Teide. The difference in the two results could be caused by the uncertainty of the location brought about by the two different observations at two different wavelengths. Nevertheless, we can see that results of calculation are relatively stable. We set the result as the upper limit of radial velocity of the SPICE observation before 10:00 UT, April 15, 2023. Our SPICE observation during pre-eruptive phase is 2-3 hours before this time point, and it only shows slow rising motions in GONG Hα observations. Therefore, this result should be reliable. Considering the radial velocity derived from these observations, only a modest Doppler dimming effect on the hydrogen Lyman lines is expected.

2.3 Concluding Remarks

In this study, we analyse the first dedicated observation of an off-limb eruptive prominence by the Spectral Imaging of the Coronal Environment (SPICE) which took place on April 15, 2023.

We have analysed the spatial variation of the integrated intensity of the Lyman β and Lyman γ lines. The solar disc exhibits high intensity due to its dense plasma and efficient collisional excitation, while the corona shows low intensity consistent with its low density. The ratio of Lyman β to Lyman γ remains roughly constant in the disc and prominence, suggesting similar radiative transfer conditions, but varies widely in the corona due to low signal levels. During the

eruption, the prominence intensity of Lyman β in region 1 increases substantially, occasionally surpassing the Lyman β intensity in the disc, indicating enhanced heating, increased hydrogen column density, or compression. But eruptive prominence region 2 shows lower intensity and smaller line width compared with pre-eruption phase. This might be due to the low density in eruptive prominence region 2.

We analysed the line widths of the Lyman β and Lyman γ lines using the quantile method. In the pre-eruption phase, the prominence region exhibits similar intrinsic line widths (0.10 nm for Lyman β, 0.16 nm for Lyman γ) compared with the solar disc (0.09 nm for Lyman β, 0.13 nm for Lyman γ). During the eruption, the line widths of the prominence and disc regions become comparable (intrinsic width $\sim$ 0.05 nm).

Compared with previous observations of quiescent prominences, our results show that eruptive prominences can display significant variations in line width, highlighting the strong influence of eruption processes on plasma dynamics and line broadening. But this possibility cannot be established solely from the present data. The difference may also be related to remaining relative uncertainties in the instrumental profiles of SPICE compared with other instruments such as SUMER on SOHO. We analysed the spatial and temporal evolution of the Lyman β and Lyman γ line profiles to diagnose plasma conditions. Overall, the spectral profiles indicate that the eruption enhances spatial and temporal variations in line intensity and line-of-sight motions, reflecting dynamic changes in plasma conditions within the prominence.

We present a method to estimate the radial velocity through a 2D plane image. This offers an efficient way of calculating the radial velocity of an eruptive filament from a pair of 2D images. The upper limit of radial velocity of the SPICE observation is about 40 km s^{-1}before 10:00 UT, April 15, 2023.

In next chapter, we will extend our analysis by applying Non-LTE radiative transfer modelling to reproduce the observed Lyman β and Lyman γ line profiles. This will allow us to constrain the plasma parameters of the prominence and refine our understanding of the physical processes governing its evolution.

Chapter 3

Non-LTE Analysis of Lyman β and Lyman γ Lines

In this chapter, we will introduce Non-LTE analysis of pre-eruptive prominence plasma parameters' effects on the Lyman β and Lyman γ lines with Solar Orbiter SPICE observations. We will use the parallel coordinate plot and the elasticity coefficient to analyse relationships among parameters. After that, we will constrain key parameters based on patterns of probability distributions.

Most contents of this chapter (i.e. text, tables and figures) come from Zhang et al. (2026b) and are written or created by me unless otherwise stated. I used PRODOP code to analyse the prominence event on April 15th, 2023, generated all figures in this paper, calculated incident radiation using SPICE full disc mosaic observations, proposed the method to analyse parameters' relations based on the parallel coordinate plot and the elasticity coefficient, and proposed a way to constrain parameters based on patterns of probability distributions. Nicolas Labrosse gave opinions about contents of figures and texts to improve the quality of the paper. Susanna Parenti and Therese A. Kucera also gave useful comments to improve the paper.

Solar Orbiter conducted its first dedicated off-limb prominence observation on April 15, 2023 (Müller et al., 2020). Solar prominences, consisting of magnetically confined plasma suspended in the corona, represent key structures in solar atmospheric dynamics and are frequently associated with coronal mass ejections (CMEs), which have significant implications for space weather. Characterizing the physical conditions of prominences, such as temperature, mass, pressure, and velocity, is essential for advancing solar physics and improving space weather forecasting.

In Chapter 2, we presented the first comprehensive analysis of Solar Orbiter/Spectral Imaging of the Coronal Environment (SPICE) off-limb prominence observation on April 15, 2023 (SPICE Consortium et al., 2020). We investigated the spatial and temporal evolution of the H-Lyman β and H-Lyman γ line profiles in the pre-eruptive and eruptive phases of the prominence. By comparing integrated intensity and line width distributions between prominence, disc, and

coronal regions, we revealed variations indicative of dynamic changes in density, temperature, and optical thickness. The study also introduced a geometric approach to derive radial velocities of eruptive filaments from a pair of Hα images. Overall, the results highlighted the diagnostic potential of SPICE Lyman lines for probing prominence plasma conditions. However, Chapter 2 also highlighted that observational data alone cannot uniquely constrain key physical parameters, thereby motivating the need for detailed non-LTE radiative transfer modelling to fully interpret the observational data in this chapter.

Gouttebroze et al. (1993) established 140 prominence models using 1D isothermal and isobaric slab geometries. Their systematic investigation provided comprehensive predictions of the hydrogen spectrum across a wide parameter space. This study revealed crucial correlations between plasma parameters and radiative outputs, particularly demonstrating a tight relationship between Hα intensity and emission measure. Warren et al. (1998) provided observational constraints through high-resolution measurements of the Lyman series (Lyβ to Lyλ) obtained with the SUMER instrument aboard SOHO. Their analysis revealed that Lyman lines show clear signatures of radiative transfer effects, with Lyβ through Lyε exhibiting self-reversed profiles and higher series members displaying flat-topped shapes. These observations also documented significant centre-to-limb variations and intensity-dependent profile asymmetries, providing essential validation for theoretical models and establishing reference profiles for incident radiation in prominence simulations.

More recently, Gunár et al. (2020) addressed the critical issue of temporal variability in incident radiation by deriving a reference quiet-Sun Lyman-α profile from SOHO/SUMER observations during the 2008 solar activity minimum. Their work provided not only a standardized profile for radiative transfer modelling but also a methodology to scale Lyman line intensities with the solar cycle using the LISIRD composite Lyman-α index. Through detailed analysis using a 2D prominence fine-structure model, they demonstrated that synthetic spectra are sensitive to changes in incident radiation, with central and integrated intensities of Lyman lines responding nearly proportionally to variations in solar illumination.

The primary objective of this study is to investigate how different plasma parameters (e.g., central pressure and central temperature) affect different properties (e.g., integrated intensity and optical thickness) of an eruptive solar prominence observed by SPICE on April 15, 2023, and to explore their influence on the formation of the Lyman β and Lyman γ lines of hydrogen. By analysing the Lyman β and Lyman γ lines observed by SPICE, we aim to derive these key parameters and investigate their influence on the formation of Lyman lines. The data were taken during the pre-eruptive phase of the prominence. During this phase, plasma parameters such as temperature, density, and pressure may undergo significant changes as the prominence evolves toward eruption. For instance, an increase in magnetic stress or heating may lead to higher temperatures and enhanced line emissions, while changes in density distribution could affect the optical thickness and collisional contributions to the Lyman lines. Understanding these pre-

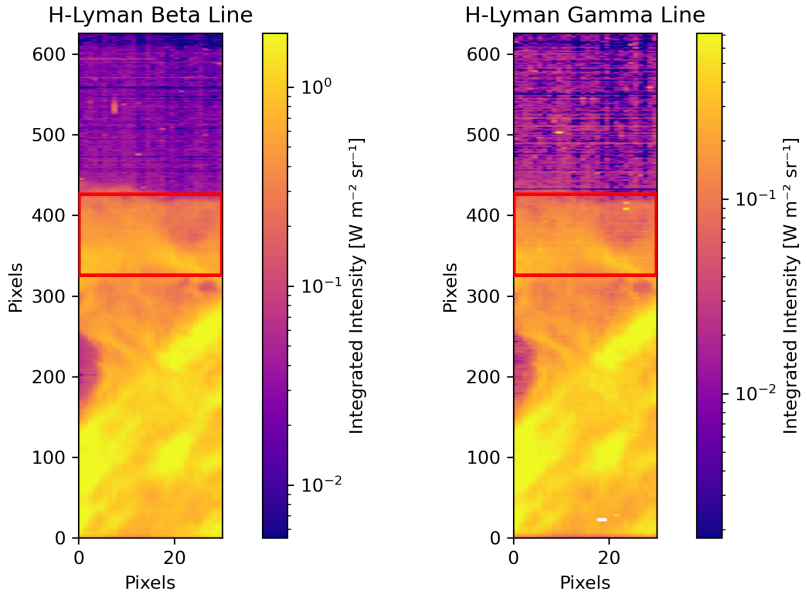

Figure 3.1: The SPICE observation of the integrated intensity of the Lyman β and Lyman γ lines taken from 07:03:40 - 08:09:23 UT, 15 April 2023. The red rectangle is the prominence region we study (Figure from Zhang et al. (2026b)).

eruptive conditions is crucial, as they set the stage for the subsequent eruption dynamics. This will provide valuable insights into the thermodynamic and dynamic properties of prominences eruption, contributing to a deeper understanding of their role in solar activity and space weather.

3.1 Observations

3.1.1 Instruments

Solar Orbiter, a solar observation mission developed by the European Space Agency (ESA) (Müller et al., 2020), follows a highly elliptical orbit around the Sun. We have given detailed description of Solar Orbiter in Section 1.3.1. The majority of its remote sensing measurements are conducted near perihelion. At the time of this observation, Solar Orbiter was located at a heliocentric distance of 0.31 AU and positioned approximately in quadrature relative to Earth.

The SPICE instrument is an imaging spectrometer that operates in the extreme ultraviolet (EUV) range, covering 69.6–79.6 nm in the short-wavelength (SW) channel and 96.0–105.8 nm in the long-wavelength (LW) channel (Anderson et al., 2020). Its primary mission is to support Solar Orbiter's scientific objectives by providing detailed diagnostics of the physical conditions and composition of plasma in the solar atmosphere.

SPICE plays a direct role in addressing Solar Orbiter's scientific objective related to coronal mass ejection (CME) formation by conducting coordinated prominence observations during 10-hour campaigns near perihelion. These campaigns utilize limb-pointing strategies in an Earth

quadrature configuration, integrating SPICE's spectral diagnostics with high-resolution imaging from the EUI instrument (Rochus et al., 2020).

In this chapter, we focus on observations of Lyman β and Lyman γ lines. The rest wavelengths of Lyman β and Lyman γ lines are 102.57 nm and 97.25 nm respectively. The formation temperature of these lines is around a few 10^4 K (Dufresne et al., 2024). These lines are emitted by neutral hydrogen in the solar atmosphere and correspond to radiative transitions of neutral hydrogen from the $n = 3$ and $n = 4$ energy levels to the ground state ($n = 1$), respectively. They are strong lines and well suited to study chromospheric plasmas, especially prominences (Heinzel et al., 2001).

3.1.2 Observations

The prominence, a large quiescent structure located in the northern hemisphere, had been observable on the solar disc as seen from Earth for 6 days prior to this observation. Between 07:30 and 10:00 UT, it exhibited initial upward motion without undergoing eruption. At approximately 10:00 UT, the central segment of the prominence erupted, leaving residual material on both sides.

SPICE observations were conducted on 15 April 2023 from 01:03 to 14:58 UT. In this study, we utilize the pre-eruption rasters acquired between 07:03 and 08:09 UT to analyse the event (DOI: 10.48326/idoc.medoc.spice.5.0).

Figure 3.1 presents SPICE observations of the prominence prior to eruption in the Lyman β and Lyman γ lines. Based on our previous work about observations (Chapter 2; Zhang et al., 2026a),, the eruption is estimated to have commenced around 10:00 UT on 15 April 2023. Analysis of the SPICE data indicates that the prominence altitude ranged approximately from 20,000 km to 60,000 km during both the pre-eruption and eruption phases. We also showed in Chapter 2 that both lines exhibit strong intensity contrast between the solar disc, prominence, and corona, with the prominence displaying intermediate but spatially structured emission. The Lyman β / Lyman γ ratio remains relatively stable in the disc and prominence, while strong scatter appears in the corona due to weak signals.

3.2 Modelling

A non-LTE (non-local thermodynamic equilibrium) model is used to describe the physical properties of plasma in the solar atmosphere, where local thermodynamic equilibrium conditions are not satisfied. This approach enables the computation of various spectral profiles. For example, to determine the emergent intensities of the Lyman lines, the radiative transfer and statistical equilibrium equations for hydrogen are solved. These calculations assume the plasma to be in ionisation equilibrium and steady state, meaning that the population of each energy level of ions

remains constant over time because of the balance between excitation and de-excitation processes. We will study the property of the pre-eruptive period of the prominence observed from 07:03 to 08:09 UT. We focus on this period because it is the only time period during which we have both Lyman β and Lyman γ lines observed simultaneously. During this period, the prominence has slow initial upward motion but the structure appears relatively stable without obvious changes in positions and shapes. We consider the assumptions of steady-state and ionisation equilibrium to be a reasonable approximation.

In this study, we use the 1D non-LTE radiative transfer code PRODOP (Gouttebroze and Labrosse, 2000). The detailed description of this code is in Section 1.2.5.

The source function of a spectral line is given by Equation 3.1:

$$S = (1-\varepsilon)\bar{J} + \varepsilon B_{\nu_0} \tag{3.1}$$

This equation has the same formal form as Equation 1.8, but its meaning is more general. Equation 1.8 is derived from a simple two-level atom, where ε can be written as $C_{jg}/(A_{jg}+C_{jg})$. In PRODOP, the atomic model contains multiple levels and continua. Therefore, ε should be interpreted as an effective photon destruction probability rather than the simple two-level expression. It represents the fraction of radiation that comes from thermal emission rather than scattering processes. B_{ν_0} in Equation 3.1 is the Planck function at frequency ν_0. $\bar{J}$ is the mean intensity of the radiation field. $(1-\varepsilon)\bar{J}$ is the radiation term and εB_{ν_0} is the collision term. Here the collision term represents the local thermal contribution associated with collisional processes.

3.2.1 Incident radiation

An accurate determination of the radiation illuminating the structure is a requirement to study the formation of resonance lines in quiescent and eruptive prominences, as this incident radiation serves as boundary condition to solve the radiative transfer equation (e.g. Labrosse et al., 2010; Vial and Engvold, 2015). In the following we describe how we determine the incident radiation on the prominence analysed in this work by using SPICE full disc mosaic observations.

In order to have the intensity from the full Sun, we used data collected during the closest SPICE mosaic observation on Nov 13–14, 2023 to generate the incident Lyman β line profile. This is the closest date of observation we can use, although it is still 7 months from the eruption. In Figure 3.4, we show the data on the solar disc used to calculate the incident Lyman β line profile. We follow the procedure of Zhang (2019) to calculate the incident radiation. We have not considered the centre-to-limb variation of the Lyman β line because it is negligible. We calculated the mean Lyman β intensity as a function of μ from the same SPICE full-disc mosaic, as shown in Figure 3.2. Here $\mu = \cos\theta$, where θ is the heliocentric angle between the local solar vertical and the line of sight. $\mu = 1$ corresponds to the disc centre and $\mu = 0$ corresponds to the solar limb. The intensity does not show a significant centre-to-limb variation.

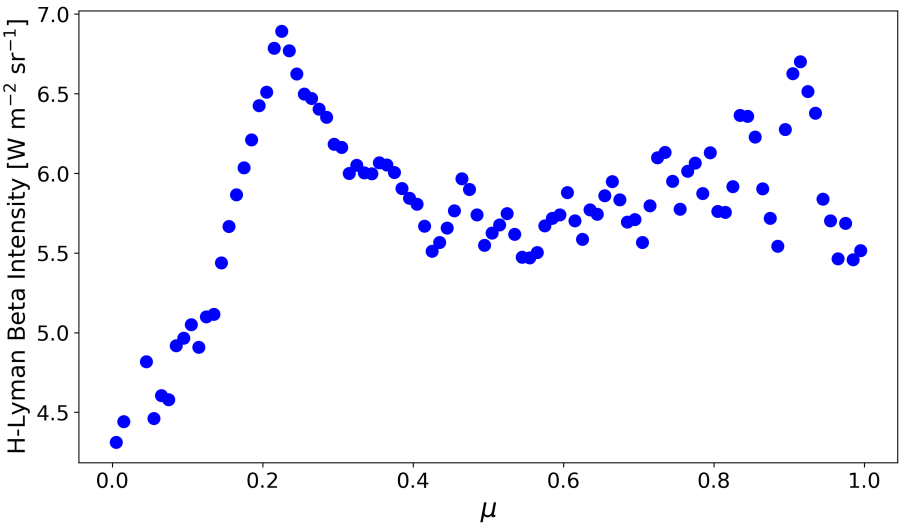

Figure 3.2: Lyman β intensity as a function of μ from the SPICE full-disc mosaic observation on Nov. 13–14, 2023.

The process of calculation involves several steps: determining the geometry of the observed region, calculating the solid angle, and integrating the intensity over the region.

Geometric Configuration

The observed solar region is modelled as a segment of the Sun, with the Sun's centre denoted as O, and the centre of the observed region on the solar surface as P_o, as shown in Figure 3.3. The SPICE instrument observes the solar region from the point M, and the radius of the Sun is represented as R_s.

The angular extent of the observed solar region is represented by ψ, which is calculated as

$$\psi = \sin^{-1}\left(\frac{R_s}{R_M}\right) \tag{3.2}$$

where R_M is the distance from the scattering point M to the centre of the Sun O (length of the line OM), given as $R_M = 152.7R_s$. The angle δ represents the angle between PM and OP from the point P. θ is the angle between P_o and P as seen from O. α is the angle between P_o and P as seen from M.

Incident Radiation Calculation

The calculation involves determining the mean intensity J from the observed region by summing contributions from individual grid points in the intensity map.

1. Coordinate Transformations and Geometry. The intensity grid represents the observed intensity values for each point on the solar surface. For each grid point (m,n), the pixel

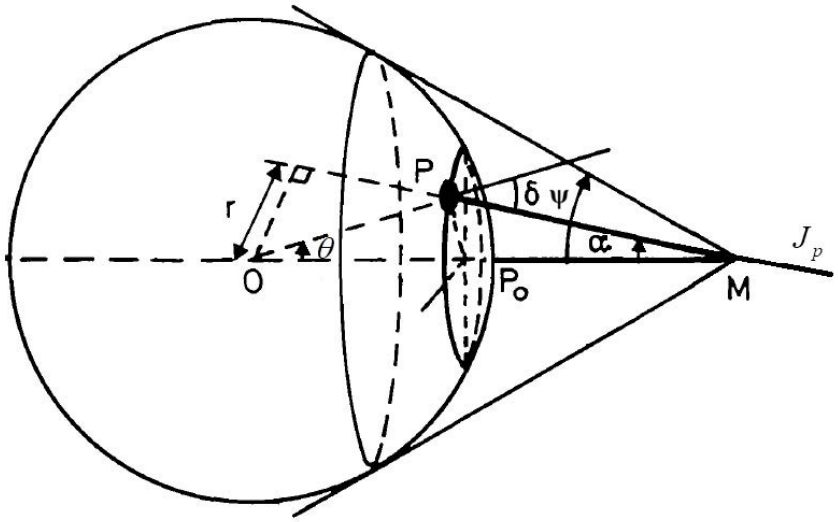

Figure 3.3: Geometric configuration of the observed solar region. O represents the Sun's centre, P_o is the centre of the observed region, and M is the scattering point. Angles ψ, α, θ and δ are shown for the region's orientation and extent (modified from Figure 5 in Sahal-Bréchot et al. (1986)).

coordinates are converted as

$$px = \text{lon_mesh}[m,n], \quad py = \text{lat_mesh}[m,n]$$

The radial distance r from the disc centre (px_0, py_0) is computed as

$$r = \sqrt{(px - px_0)^2 + (py - py_0)^2} \tag{3.3}$$

If r satisfies $r < R_s \cos(\psi)$, where $\psi = \arcsin\left(\frac{R_s}{R_M}\right)$, the grid point is considered part of the observed region.

2. Calculation of Radiation Flux. The mean radiation flux J is determined by summing the contributions from all the grid points. The contribution of each point involves calculating the solid angle $d\Omega$ and the corresponding flux contribution dJ.

   First, the area element ds corresponding to each grid point is given by

$$ds = \frac{dx\,dy}{\cos(\theta)} \cdot \mu \tag{3.4}$$

   where dx and dy are the pixel sizes in the longitude and latitude directions, and $\mu = \cos(\delta)$ accounts for the projection of the surface element based on the zenith angle δ. The term $\frac{1}{\cos(\theta)}$ compensates for the projection of the area element onto the plane of the sky, correcting for the curvature of the Sun's surface. The factor $\mu = \cos(\delta)$ ensures that the radiation flux calculation accounts for the orientation of the observed region relative to the

observer's line of sight (**OM**).

The solid angle $d\Omega$ subtended by the area element is then

$$d\Omega = \frac{ds}{D^2} \tag{3.5}$$

where D is the distance from the area element on the Sun's surface to the scattering point M

$$D = \sqrt{R_1^2 + r^2} \tag{3.6}$$

where R_1 is defined as

$$R_1 = R_M - R_s \cos(\theta) \tag{3.7}$$

with $R_M = 152.7 R_s$ and R_s being the radius of the Sun.

The solid angle represents the fraction of the sky subtended by the area element, and is essential in calculating the radiation observed by the instrument.

The contribution to the total flux dJ from each grid point is given by

$$dJ = \frac{d\Omega \cdot \text{intensity_grid}[m,n]}{4\pi} = J(\Omega)\, d\Omega \tag{3.8}$$

Now, the mean intensity from the observed region is calculated as

$$\begin{aligned} J &= \frac{1}{\Omega} \oint_\Omega J(\Omega)\, d\Omega = \frac{1}{\frac{\pi (R_s \cos\psi)^2}{R_M^2}} \oint_\Omega J(\Omega)\, d\Omega \\ &= \frac{R_M^2}{\pi R_s^2 \cos^2(\psi)} \oint_\Omega J(\Omega)\, d\Omega \\ &= \frac{1}{\cos^2(\psi)\sin^2(\psi)\pi} \oint_\Omega J(\Omega)\, d\Omega \end{aligned} \tag{3.9}$$

In Figure 3.5, the red points are the incident Lyman β line profile we obtain by integrating over the entire disc and the orange line is the Gaussian fit of the red points. The green line is the average line profile within the 50 arcsec of the solar centre in the mosaic image. The blue line is the original Lyman β line profile in the PRODOP NLTE code. It is a disc-averaged profile from Warren et al. (1998) and also the default input of the PRODOP NLTE code. It is obtained by the SUMER instrument on SOHO and presented in Warren et al. (1998). Thus, the orange and green profiles are derived from the SPICE mosaic, while the blue profile is the adopted modelling input of the incident spectral shape.

However, we cannot use the incident Lyman β line profile we obtained (orange line in Fig. 3.5) directly, as the incident spectral profile is convolved with the broad SPICE instrumental profile. It is clear that the typical line shape of the Lyman β line with its two peaks and central reversal is lost due to the convolution with the instrumental profile. Using this profile

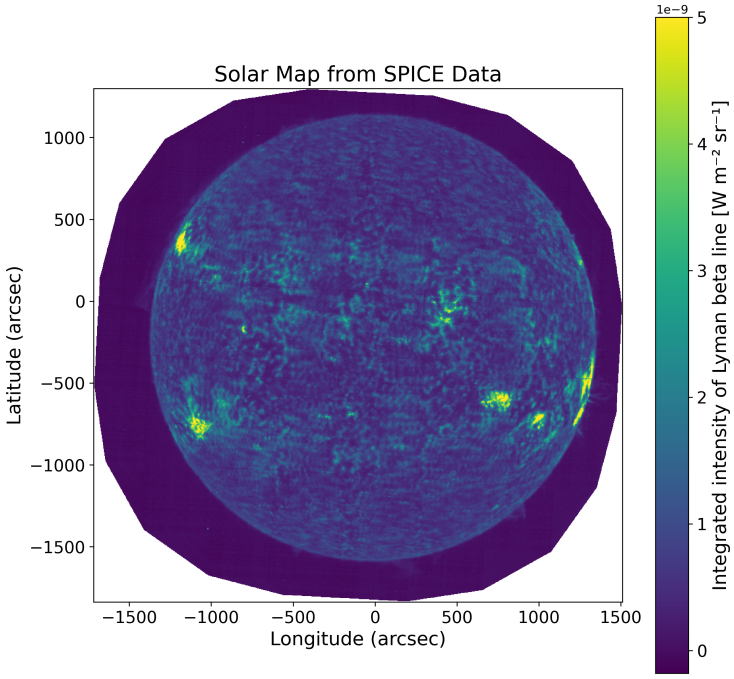

Figure 3.4: The solar map of the integrated intensity of the H-Lyman β line by SPICE full disc mosaic observation on Nov 13-14, 2023 (Figure from Zhang et al. (2026b)).

would not enable us to compute realistic emergent profiles. The SPICE Point Spread Function introduces several artefacts which are discussed in Plowman et al. (2023). For our purpose, we preferred to avoid the deconvolution of the profile and instead adopt the shape of the profile from Warren et al. (1998). The reason for adopting the blue profile is that the SPICE profiles are strongly influenced by the instrumental profile. This line shape is important for the NLTE radiative transfer calculation because the incident radiation field controls the resonance scattering contribution to the emergent prominence emission. We did not attempt to deconvolve the SPICE profile because a reconstruction of the intrinsic Lyman β profile would require the SPICE instrumental line profile.

Therefore, we only use the integrated intensity of the observed incident Lyman β line profile to re-scale the original Lyman β line profile used in the NLTE code. We also normalize the original Lyman γ line profile in the NLTE code by the same ratio we apply to normalize the Lyman β line profile in the NLTE code. We do not correct the incident intensities of the other Lyman lines in the code. As we cannot determine more precisely the line profiles to determine the incident radiation on the day of these observations, it is reasonable to assume that the overall shapes of both lines do not vary significantly over time.

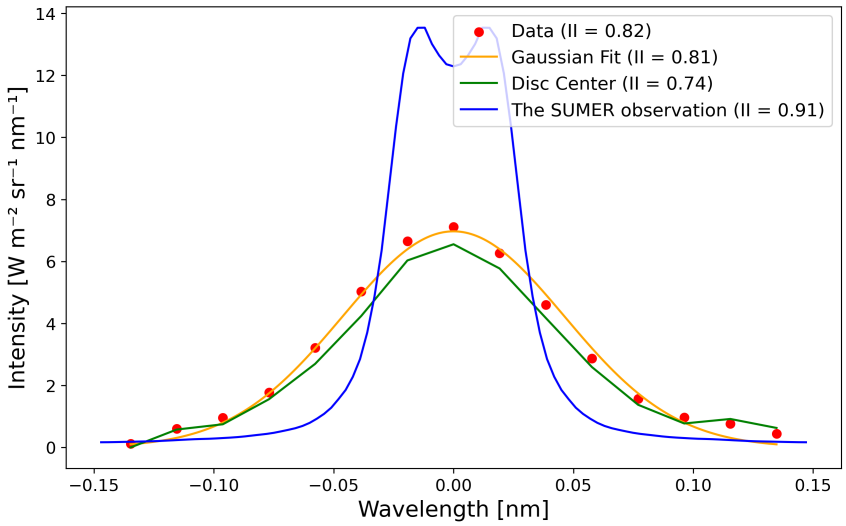

Figure 3.5: The red points are the incident Lyman β line profile we obtained following the method of Zhang (2019) with SPICE full disc mosaic observation on Nov 13–14, 2023, and the orange line is the Gaussian fit of the red points. The green line is the average line profile within the 50 arcsec of the solar centre in the mosaic image. The blue line is the incident Lyman β line profile in the PRODOP NLTE code. It is obtained by the SUMER instrument on SOHO and presented in Warren et al. (1998). II is the abbreviation of Integrated Intensity, with units of W m^{-2} sr^{-1} (Figure from Zhang et al. (2026b)).

3.2.2 Toolkit to interpret model results

Parallel coordinate plot

We use the method of the parallel coordinate plot to analyse the parameters' effect in the 2023 April 15th event (Edsall, 2003; Ge et al., 2009). Parallel coordinate plots provide a method to visualize relationships in multivariate data. With this method, we can see a parameter's effect more obviously without setting other parameters to specific values, and we can simultaneously display and compare values and relationships of multiple variables, even for non-linear relationships. We demonstrate the potential of this method by studying the well-known correlation between Hα intensity and emission measure in prominences (Gouttebroze et al., 1993; Heinzel et al., 1994). We create 200 random isobaric and isothermal models with the same parameters' ranges as Heinzel et al. (1994).

Figure 3.6 shows the relation between emission measure, temperature, pressure, and slab thickness on the emitted intensity in the Hα line. In a parallel coordinate plot like Figure 3.6, each line connected from left side to right side represents a model and each connected point on this line represents one parameter of the model. In Figure 3.6, the temperature, pressure and slab thickness are inputs of the model, and integrated intensity and emission measure are outputs of the model. The colour is set by values of integrated intensity. If we see a diversity of colours connected to different value ranges when we focus on one parameter's axis, this means the parameter does not have much effect (such as slab thickness in Figure 3.6); on the other

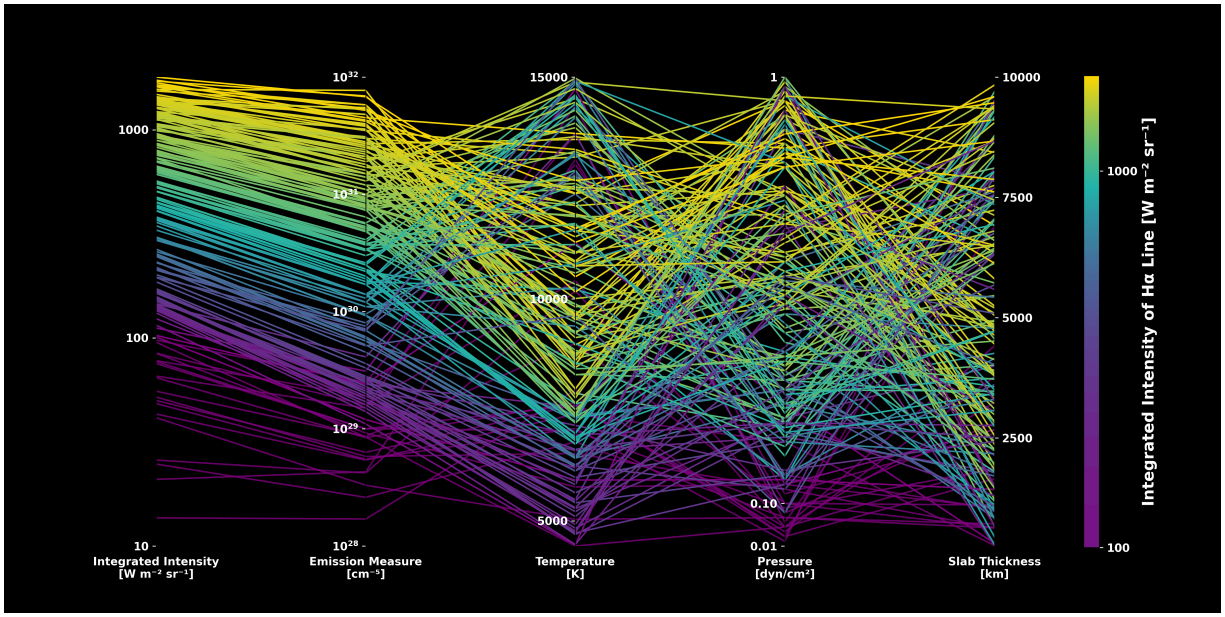

Figure 3.6: The parallel coordinate plot of 4 parameters with the integrated intensity of the Hα line. In a parallel coordinate plot, if we see a diversity of colours connected to different value ranges when we focus on one parameter's axis, this means the parameter does not have much effect; on the other hand, if we see a certain colour concentrated on a certain value range, this means the parameter has some effect. For example, we can see that in the axis of emission measure, temperature, and pressure, the colour seems to be more uniform in different parts. This suggests that these parameters have relatively high correlation coefficients (usually larger than 0.3) with integrated intensity (Figure from Zhang et al. (2026b)).

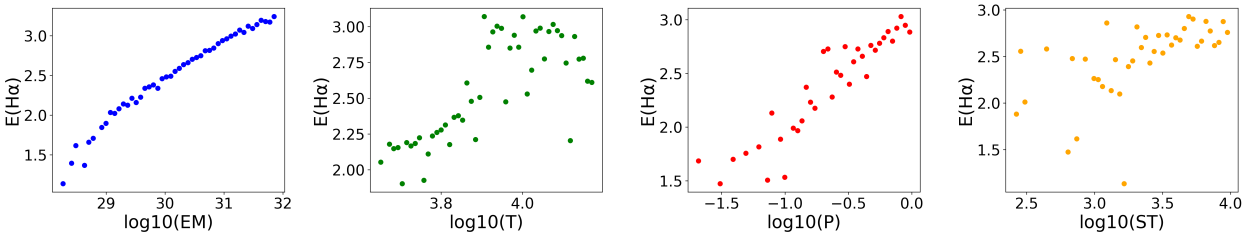

Figure 3.7: Integrated intensity vs. emission measure, temperature, pressure and slab thickness for the Hα line. We divided the range of each x-axis parameter (log EM, log T, log p, log ST) into 50 bins. For each bin, all models falling inside it (the number varies across bins) were averaged in log E(Hα), and only bins containing data are shown (Figure from Zhang et al. (2026b)).

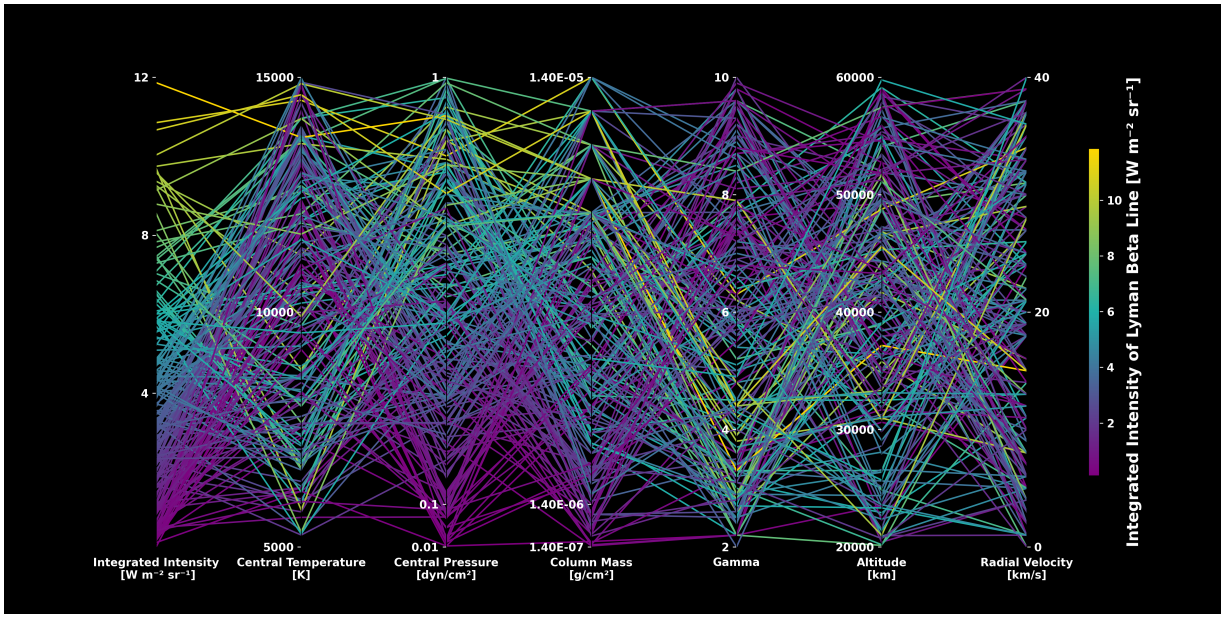

Figure 3.8: The parallel coordinate plot of 6 parameters with the integrated intensity of the Lyman β line (Figure from Zhang et al. (2026b)).

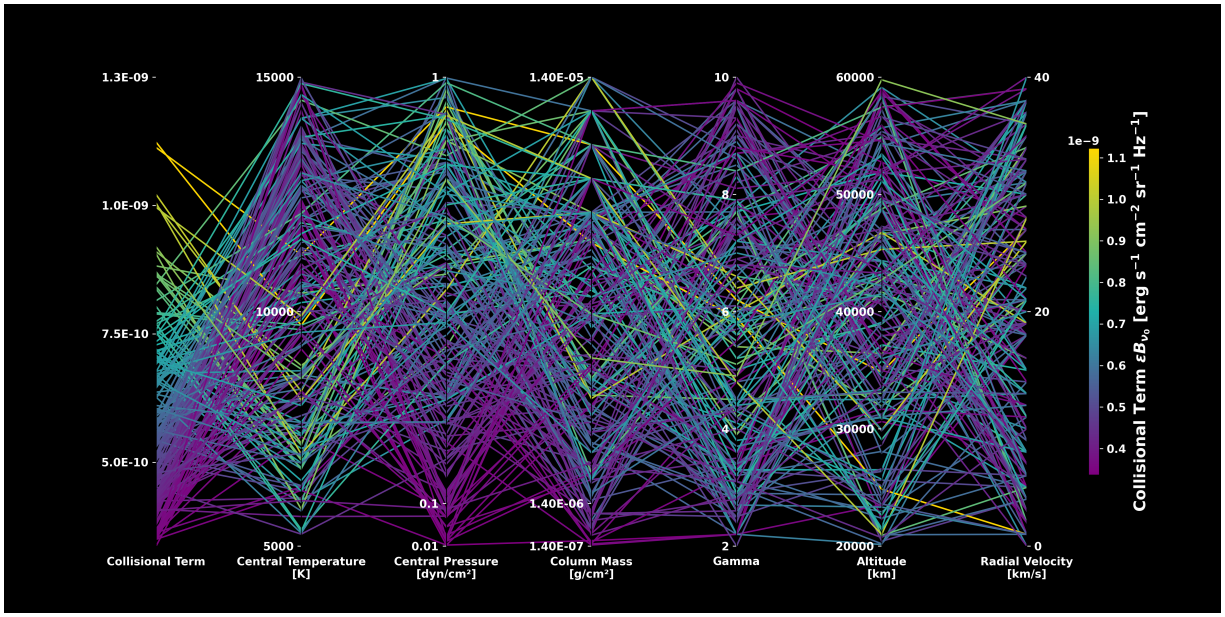

Figure 3.9: The parallel coordinate plot of 6 parameters with the collisional term εB_{ν_0} of the Lyman β line (Figure from Zhang et al. (2026b)).

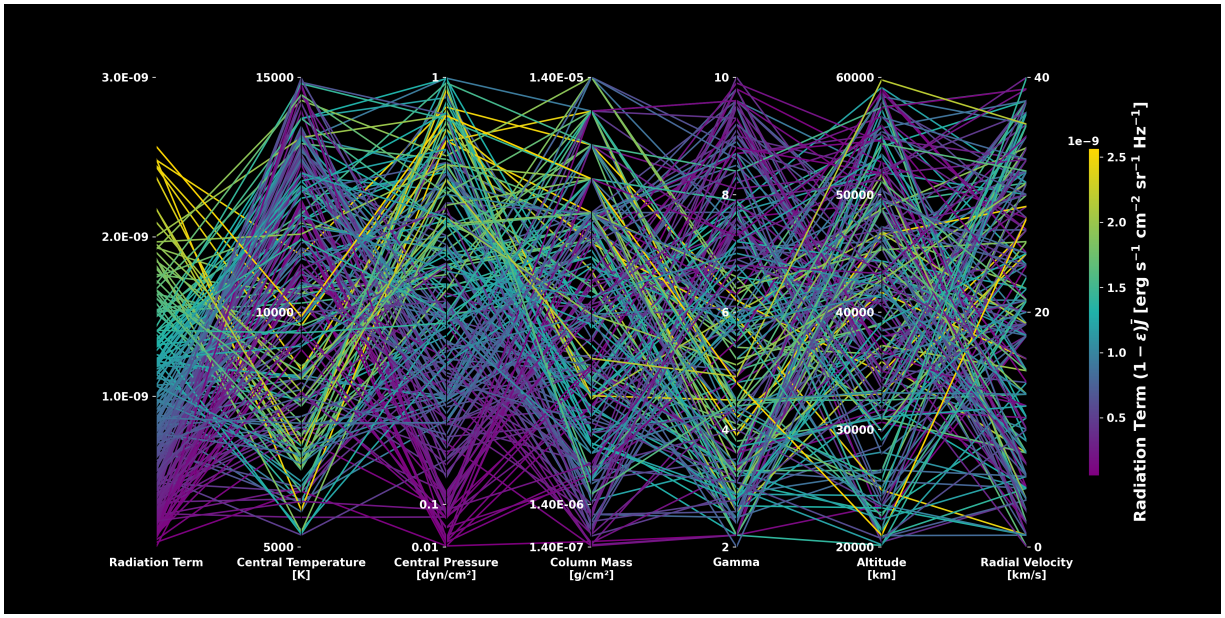

Figure 3.10: The parallel coordinate plot of 6 parameters with the radiation term $(1-\varepsilon)\bar{J}$ of the Lyman β line (Figure from Zhang et al. (2026b)).

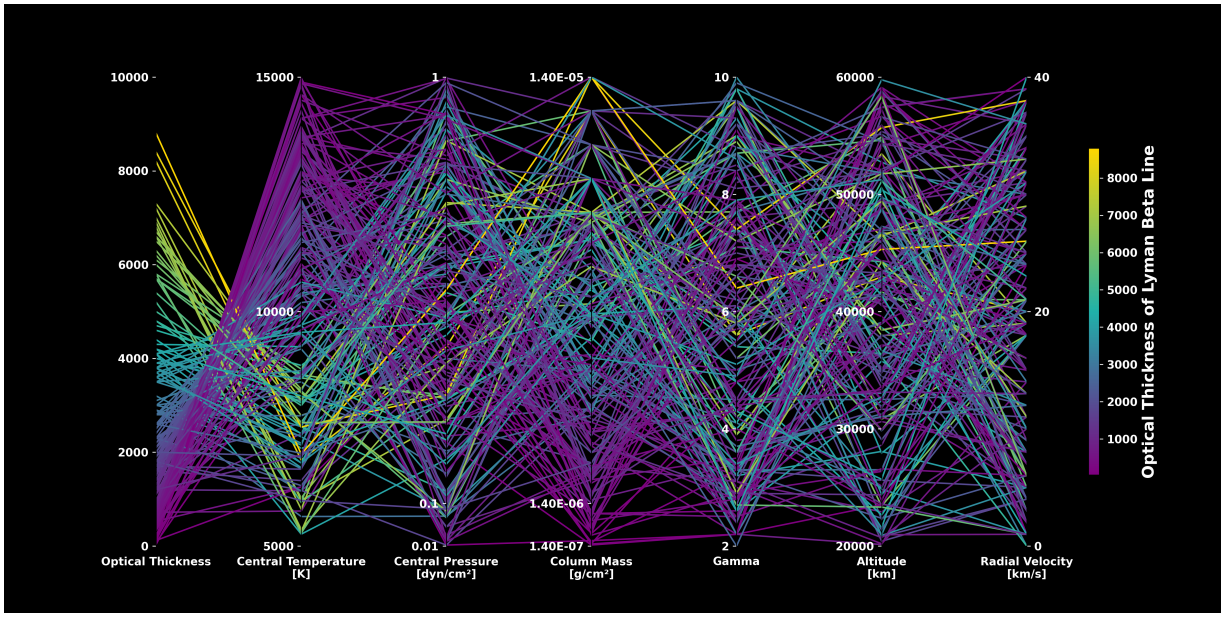

Figure 3.11: The parallel coordinate plot of 6 parameters with the optical thickness of the Lyman β line (Figure from Zhang et al. (2026b)).

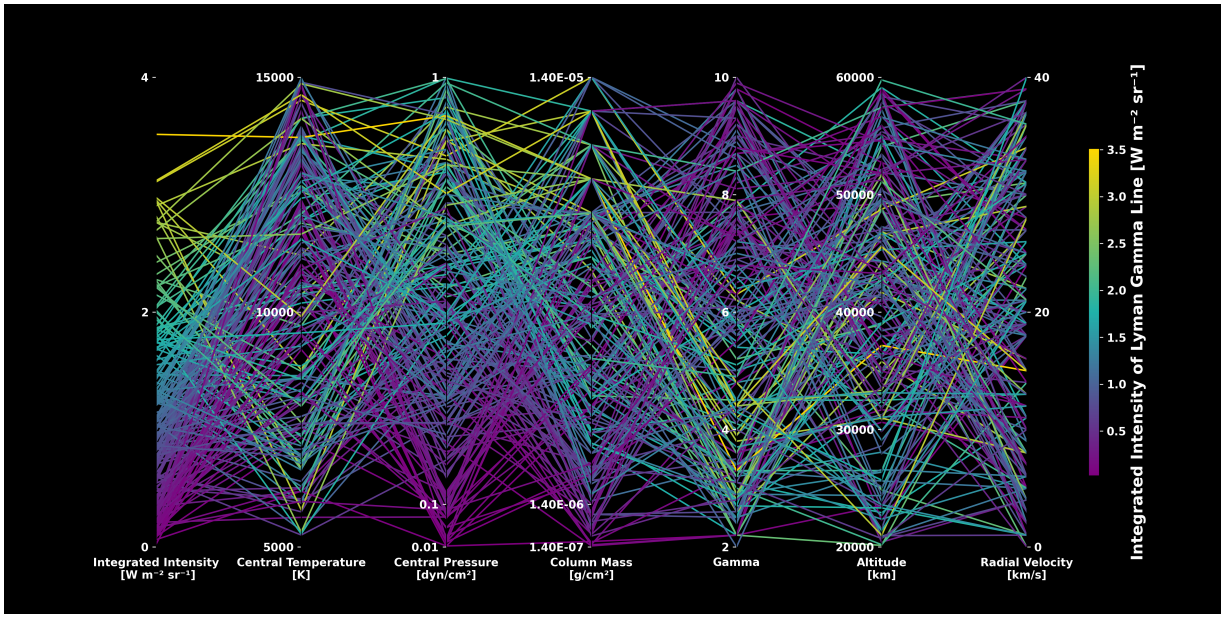

Figure 3.12: The parallel coordinate plot of 6 parameters with the integrated intensity of the Lyman γ line (Figure from Zhang et al. (2026b)).

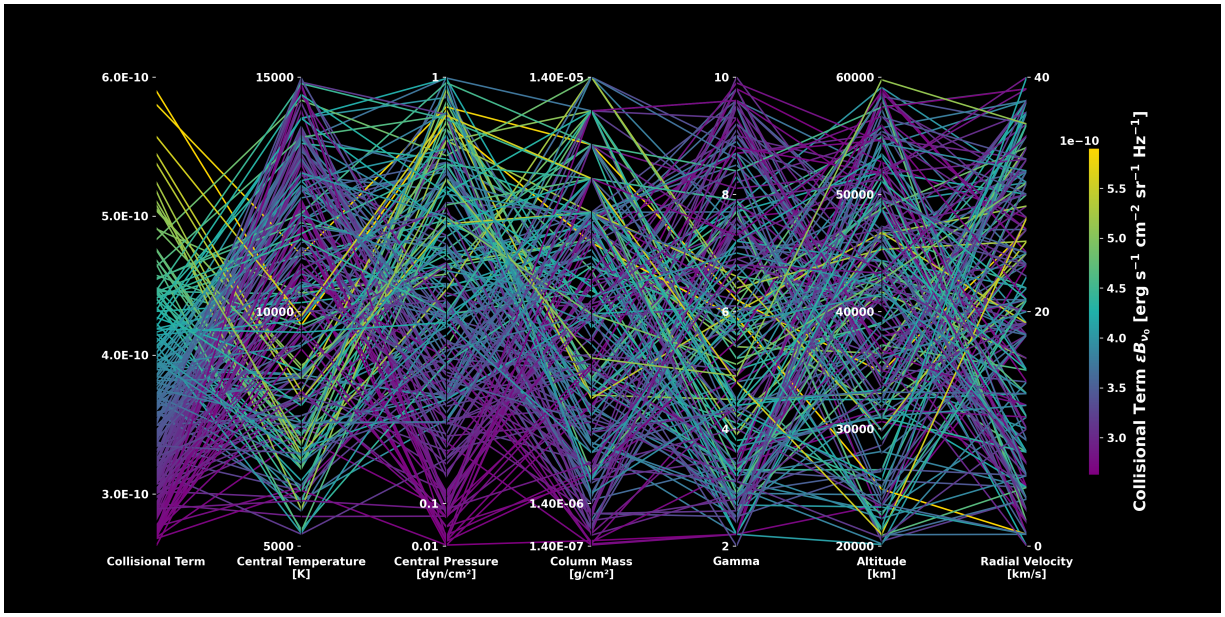

Figure 3.13: The parallel coordinate plot of 6 parameters with the collisional term εB_{ν_0} of the Lyman γ line (Figure from Zhang et al. (2026b)).

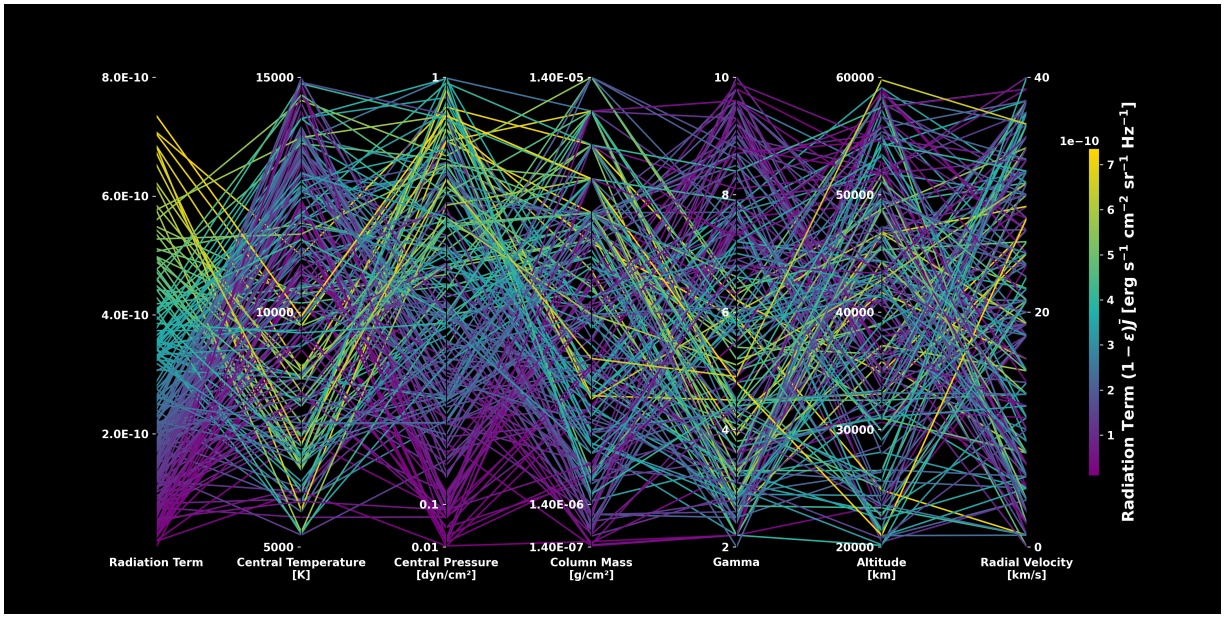

Figure 3.14: The parallel coordinate plot of 6 parameters with the radiation term $(1-\varepsilon)\bar{J}$ of the Lyman γ line (Figure from Zhang et al. (2026b)).

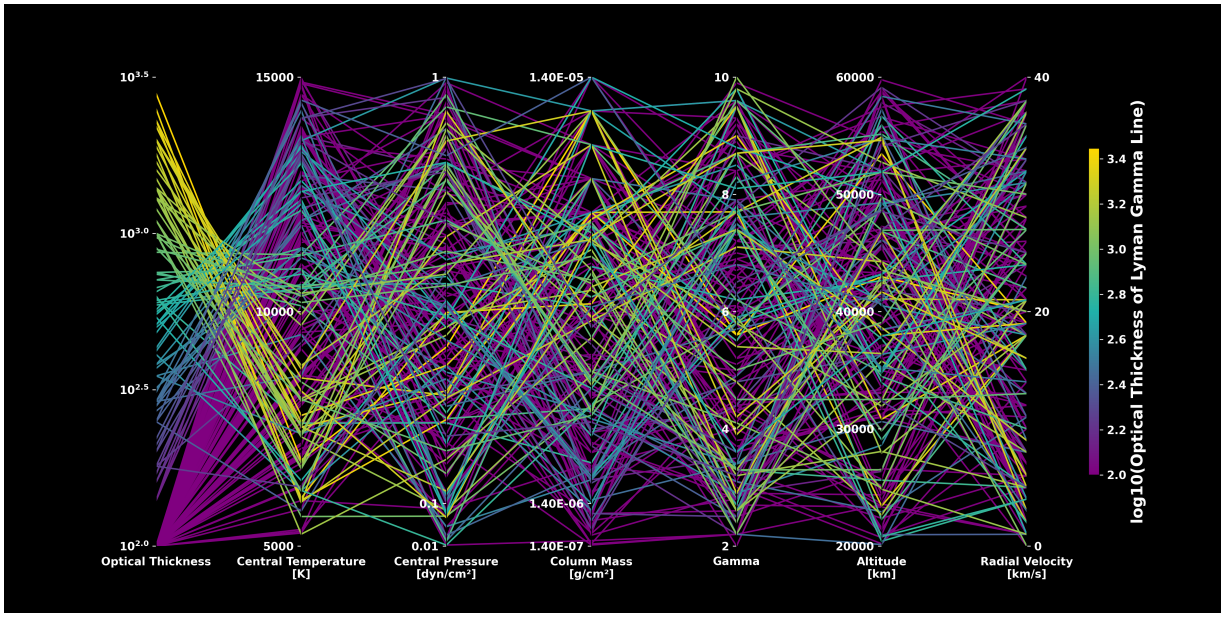

Figure 3.15: The parallel coordinate plot of 6 parameters with the optical thickness of the Lyman γ line (Figure from Zhang et al. (2026b)).

hand, if we see a certain colour concentrated in a certain value range, this means the parameter has some effect (such as emission measure, temperature, and pressure in Figure 3.6).

Figure 3.7 shows the relations between Hα integrated intensity and emission measure, temperature, pressure and slab thickness in a more common representation. Figure 3.7 shows that Hα intensity increases with emission measure and pressure. This conclusion is the same as Heinzel et al. (1994). The panels showing integrated intensity of the Hα line versus temperature and slab thickness in Figure 3.7 are not included in Heinzel et al. (1994). The panel showing Hα integrated intensity versus temperature suggests a broad tendency for larger Hα intensities at higher temperatures, but the correlation is scattered. No error bars are shown in Figure 3.7 because the points are not observational measurements, but individual NLTE models. For the models computed in this study, Figure 3.7 shows that the Hα integrated intensity versus slab thickness relationship does not exhibit as clear a trend as the other relationships.

Figure 3.7 shows the relations between emission measure, temperature, pressure and slab thickness, with the integrated intensity of the Hα line. However, a single parallel coordinate plot in Figure 3.6 contains the same information about these relations, and includes even more information. When the value range on which a certain colour is concentrated is narrow, the effect is more significant. From Figure 3.6, we know emission measure, temperature, and pressure have an effect on the integrated intensity of the Hα line. From the concentration of colour, we know the correlation between emission measure and the integrated intensity of the Hα line is stronger than the correlation between pressure and the integrated intensity of the Hα line, and the correlation between temperature and the integrated intensity of the Hα line is even weaker than the correlation between pressure and the integrated intensity of the Hα line. We can use correlation coefficients to further confirm this result. After calculation based on the running results of 200 random models, we know that emission measure, temperature, and pressure have correlation coefficients of 0.98, 0.41, and 0.66 with the integrated intensity of the Hα line, which is consistent with our result. It is not necessary to use correlation coefficients when we use parallel coordinate plots. It depends what conclusions the user wants. If the user just want to find out which parameter has stronger effect on a property, it is not necessary to use the correlation coefficient. Actually, the parallel coordinate plot contains more information about how a parameter is related to a property. But if the user want to quantify the result, we can calculate the correlation coefficient.

Additionally, we can not only check one parameter's effect by focusing on the axis, but also track other parameters' values by following the lines. In this way, we can find out the composition of models with high integrated intensity and those with low integrated intensity.

Parallel coordinate plots complement correlation coefficients by showing how parameter influences vary across their value ranges. In the rest of our analysis, they will serve mainly as a compact way to identify where the collisional term, radiation term, integrated intensity, and optical thickness reach high or low values, and what parameter combinations produce them. This

integrated view of multi-parameter behaviour cannot be obtained from correlation coefficients alone, making the plot an efficient diagnostic tool for identifying non-linear or range-dependent relationships.

In summary, a parallel coordinate plot has the following advantages:

- It helps us discover potential relations among different parameters. The parallel coordinate plot effectively illustrates how all data points transition across multiple parameters, thereby revealing structural patterns and potential inter-parameter relationships. We can intuitively draw some conclusions by focusing on a parallel coordinate plot. It is not a quantitative method, but it helps to identify possible correlations among parameters. These visually identified relations are used only as exploratory guidance and are not treated as quantitative modelling results. Quantitative methods can be further used to characterise correlations that are found in a parallel coordinate plot. Especially when the relationship is non-linear, it would be hard to notice the relationship just by quantitative methods like correlation coefficient calculation.

- It is an efficient way to show parameters' relations. A single parallel coordinate plot contains a large amount of information. Other more traditional figures show similar information but require several figures to arrive at the same level of information.

- We can track specific colours to identify the parameters that are used to construct different models;

- We can understand the sensitivity of the property that determines the colours to different ranges of the other parameters shown in the plot.

We will introduce these advantages with detailed examples in the following sections.

Elasticity coefficient

We calculate the elasticity coefficient to show how the quantities we study (quantities in the first axis and depicted by the colour in our parallel coordinate plots) are sensitive to changes in other parameters. In the following definition, y represents the studied quantity, such as integrated intensity, and x represents one model parameter. We calculate the elasticity coefficient between two quantities x and y (e.g. central pressure and integrated intensity) by Equation 3.10.

$$e_{xy} = \frac{\frac{\Delta x}{\bar{x}}}{\frac{\Delta y}{\bar{y}}} = \frac{\Delta x}{\Delta y} \cdot \frac{\bar{y}}{\bar{x}} \tag{3.10}$$

$\frac{\Delta x}{\Delta y}$ is estimated by the regression coefficient in a simple linear regression model using the individual model results. Therefore, the elasticity coefficient represents a relative sensitivity

within the sampled model range, rather than a local physical derivative. $\bar{x}$ and $\bar{y}$ are means of x and y. A larger elasticity coefficient e_{xy} (the absolute value) means the parameter x is more sensitive to the relative change of the studied quantity y.

It should be noted that the elasticity coefficient measures relative changes, not absolute changes. Therefore, it cannot be interpreted simply from the total range covered by each parameter in the plot. A parameter spanning several orders of magnitude does not necessarily imply a stronger sensitivity, because the coefficient also depends on the regression slope and on the normalisation by the mean values of the two quantities.

We can also take Heinzel et al. (1994) as an example. After calculation based on modelling results, we know that emission measure, temperature, and pressure have elasticity coefficients of 5.91, 0.24, and 0.22 with the integrated intensity of the Hα line. This suggests that within the sampled model grid, the integrated intensity of the Hα line has the largest relative sensitivity to emission measure.

In Figure 3.6, the transition regions between high-value and low-value ranges of integrated intensity of the Hα line are more concentrated at the axis of emission measure. This characteristic is qualitatively consistent with the high elasticity coefficient of emission measure.

3.3 Results

Using the altitude and incident radiation constraints as described in Section 3.1.2 and Section 3.2.1, the radial velocity constraint from Chapter 2, and the usual range for the other parameters from Labrosse and McGlinchey (2012), we generate 200 random PCTR models for the prominence as shown in Table 3.1. The altitude range is taken from the observed height of the prominence in the SPICE data, and the radial velocity range is constrained by the observational upper limit derived in Chapter 2. The remaining thermodynamic parameters are chosen to cover typical prominence and PCTR conditions used in previous NLTE prominence modelling studies.

The line-of-sight depth is estimated from the prominence width measured in the GONG Hα observation, assuming that the LOS depth is comparable to the plane-of-sky width. With $L_{\mathrm{LOS}} = 136000$ km and the column mass range in Table 3.1, the line-of-sight averaged number density is estimated to be $n \sim 5.0 \times 10^8\ cm^{-3}$. This value is comparable to the density near the surface part of the NLTE slab models, where the temperature is high and the pressure is relatively low. It is much lower than the density in the cool prominence core, which can reach values of order 10^{11} cm^{-3} in the models.

The number of models was chosen as a compromise between sampling the parameter space and computational cost. We tested different random samples, including 1000 models, and found that the main trends shown in the parallel coordinate plots did not change significantly compared with the 200 models sample. Increasing the number of models mainly increased the density of lines in the plots, but did not reveal additional parameter information. Since this section com-

pares the effect of each input parameter on each line property separately, rather than performing a full multidimensional parameter inversion, 200 models are sufficient for identifying the main qualitative trends discussed here. The calculations were run on a machine with an Intel Core i7-10875H processor at 2.3 GHz. The calculation of 200 models required approximately 1 hours. A substantially larger grid would therefore increase the computational cost, while providing little additional information for the exploratory analysis.

The surface temperature is fixed at 100000 K because it mainly affects the outer PCTR layers, which contain only a small fraction of the total column mass. Moderate changes of this value have a limited effect on the Lyman lines emission in these models. Its influence would become more important only if the surface temperature were changed by a much larger factor. Therefore, in this grid we keep the surface temperature fixed.

In Figures 3.8–3.15, we explore the effects of central temperature, central pressure, column mass, gamma, altitude and radial velocity on integrated intensity, collisional term, radiation term and optical thickness in a qualitative graphical way. Since there are more obvious effects on a parallel coordinate plot when the correlation coefficient is larger than 0.3, we consider a parameter important in this case. We also use the correlation coefficient and the elasticity coefficient (between the parameter and the property we study) in the Table 3.2 and Table 3.3 to quantify the effect. The correlation coefficient and the elasticity coefficient are not expected to be simply related. The correlation coefficient measures how tightly two quantities vary together, while the elasticity coefficient measures the relative response of the studied property to a relative change in a model parameter. Since the elasticity coefficient also depends on the regression slope and on the normalisation by the mean values of the two quantities, a parameter with a relatively small correlation coefficient can still have a non-negligible elasticity coefficient. Values not shown in the tables correspond to correlation coefficients smaller than 0.3 and their elasticity coefficients are generally smaller than the lowest values listed in the tables. However, there are exceptions. For example, the elasticity coefficient of central temperature for the radiation term in Lyman β and Lyman γ lines is very close to that of column mass (0.39 and 0.42), even though its correlation coefficient is below 0.3. Similarly, for the collisional term in the Lyman γ line, altitude and central temperature have elasticity coefficients (-0.15 and 0.13) comparable to that of column mass. For optical thickness, only the elasticity coefficient of temperature exceeds 1, while column mass also shows relatively large values (0.77 for Lyman β and 0.62 for Lyman γ) though its correlation coefficient is below 0.3.

From Figures 3.8–3.15, the dependencies between the line properties and the model parameters can be summarized as follows. For both Lyman β and Lyman γ, a higher central pressure usually corresponds to a higher integrated intensity, while larger values of column mass also tend to increase the intensity. In contrast, when Γ increases, the integrated intensity decreases, indicating that a stronger temperature gradient suppresses the total emission. When Γ is large, it means that the temperature changes quickly from prominence surface to the prominence centre.

Table 3.1: Parameter ranges for different variables

Parameter	Range
Central Temperature	5000 K $\sim$ 15000 K
Surface Temperature	100000 K
Central Pressure	0.01 dyn cm^{-2} $\sim$ 1.0 dyn cm^{-2}
Surface Pressure	0.01 dyn cm^{-2}
Column Mass	1.4×10^{-7} g cm^{-2} $\sim$ 1.4×10^{-5} g cm^{-2}
Γ	2 $\sim$ 10
Altitude	20000 km $\sim$ 60000 km
Radial Velocity	0 km s^{-1} $\sim$ 40 km s^{-1}
Microturbulent Velocity	5 km s^{-1}

Table 3.2: Correlation and elasticity coefficients for Lyman β line properties

Property	Key Parameters	Coefficients	
		Correlation	Elasticity
Integrated Intensity	Central pressure	0.70	0.90
	Column mass	0.49	0.61
	Gamma	-0.32	-0.56
Collisional Term εB_{ν_0}	Central pressure	0.66	0.35
	Column Mass	0.37	0.19
Radiation Term $(1-\varepsilon)\bar{J}$	Central pressure	0.72	0.86
	Column Mass	0.34	0.39
	Gamma	-0.34	-0.54
Optical Thickness	Central temperature	-0.66	-2.13
	Column mass	0.51	0.76

Note: The parameters that don't appear in the table correspond to correlation coefficients less than 0.3.

Table 3.3: Correlation and elasticity coefficients for Lyman γ line properties

Property	Key Parameters	Coefficients	
		Correlation	Elasticity
Integrated Intensity	Central pressure	0.69	0.89
	Column mass	0.45	0.56
	Gamma	-0.37	-0.65
Collisional Term εB_{ν_0}	Central pressure	0.69	0.25
	Column Mass	0.37	0.13
Radiation Term $(1-\varepsilon)\bar{J}$	Central pressure	0.69	0.86
	Column Mass	0.35	0.42
	Gamma	-0.34	-0.56
Optical Thickness	Central temperature	-0.37	-2.23

Note: The parameters that don't appear in the table correspond to correlation coefficients less than 0.3.

Therefore, there would be less hot materials for the prominence. This could affect the population of different energy levels of the hydrogen atoms and then affect the emission.

For the collisional term εB_{ν_0}, higher central pressure or larger column mass is generally associated with a larger collisional term. For the radiation term $(1-\varepsilon)\bar{J}$, higher central pressure or larger column mass is also generally associated with a larger radiation term, whereas larger Γ values lead to smaller values of the radiation term.

For the optical thickness, an increase in central temperature tends to reduce optical thickness in both lines, meaning that hotter core conditions lead to smaller optical thickness. At the same time, larger column mass values correspond to higher optical thickness, reflecting the role of plasma content in enhancing absorption. This effect is strong in Lyman β line but not in Lyman γ line.

3.3.1 The Lyman β line

Figures 3.8–3.11 show the relationships between various parameters and the Lyman β line properties. In Figure 3.8, we can see that in the axis of central pressure, column mass and gamma, the colour seems to be more uniform in different parts. This usually suggests a relatively high correlation coefficient (larger than 0.3). Also, the axis of central pressure shows less diversity of colour in different parts of the axis, which suggests a higher correlation coefficient. We can refer to Table 3.2. The correlation coefficient between central pressure and integrated intensity of Lyman β is 0.70. This is higher than column mass and gamma. In Figure 3.9 and Figure 3.10, we can see that the collisional term εB_{ν_0}, and the radiation term $(1-\varepsilon)\bar{J}$ have a similar order of magnitude and the value range of the radiation term is about ~ 2 times of collisional term. This suggests that the collisional and radiative contributions are equally important for the formation of the Lyman β line.

The elasticity coefficients for the Lyman β line properties are presented in Table 3.2. For parameters with large values of the elasticity coefficient in Table 3.2, we can refer to Figure 3.8, Figure 3.10, and Figure 3.11. The high-value and low-value ranges of the quantities we study are more concentrated and their colour in those ranges is more uniform. In Figure 3.11, the high-value range of the optical thickness (larger than 4000) is well concentrated below the 10000 K on the axis of the central temperature, while the values of the optical thickness are all below 4000 above 10000 K. Also, in Figure 3.10, we can see that the high-value range of the radiation term $(1-\varepsilon)\bar{J}$ (larger than 2×10^{-9}) is well concentrated on the upper side of the axis of the central pressure. Therefore, the elasticity coefficient is also a useful tool to describe the characteristics of certain parameters. When an elasticity coefficient for two parameters is high, this indicates that it is possible to use one parameter to constrain the other (we will discuss this further in Section 3.3.3).

The correlation coefficients and elasticity coefficients of the key parameters for the properties of the Lyman β line are summarized in Table 3.2. From Table 3.2, we can see that there are no

direct relations between the correlation coefficients and the elasticity coefficients. The elasticity coefficients can be high or low with a similar correlation coefficient.

3.3.2 The Lyman γ line

The correlation coefficients and elasticity coefficients of the key parameters for the properties of the Lyman γ line are summarized in Table 3.3. The results are similar to those obtained from the analysis of the Lyman β line.

In Figure 3.12, we can see that in the axis of central pressure, column mass and gamma, the colour seems to be more uniform in different parts, which suggests a relatively high correlation coefficient (larger than 0.3). In Figures 3.13 and 3.14, we can see that the collisional term εB_{ν_0} and radiation term $(1-\varepsilon)\bar{J}$ have a similar distribution of values. This suggests that collisional contribution and radiative contribution are equally important for the formation of the Lyman γ line. In Figures 3.15, we can see that all yellow lines (optical thickness larger than 1000) distribute below 10000 K on the axis of central temperature and the distribution seems to be random on other axis. This suggests that temperature is the only key parameter that is related to optical thickness of the Lyman γ line.

3.3.3 Constraining parameters using SPICE data

We have just determined that the important parameters for the integrated intensity of the Lyman β and the Lyman γ lines are central pressure, column mass, and gamma. Therefore, we can further constrain these parameters through the Lyman β and the Lyman γ line intensities measured for the prominence. In Figure 3.1, the red rectangle is the prominence region we study. The mean integrated intensity of Lyman β in this region is 0.46 W m^{-2} sr^{-1}, and the standard deviation is 0.21 W m^{-2} sr^{-1}. The mean integrated intensity of Lyman γ in this region is 0.16 W m^{-2} sr^{-1}, and the standard deviation is 0.08 W m^{-2} sr^{-1}.

When we apply a restriction to filter the 200 random models to make the Lyman β and Lyman γ integrated intensities within three standard deviations of the mean, we obtain 38 models which meet the requirement. We find that 36 of them have a central pressure below 0.48 dyn cm^{-2}. However, we find that the column mass and gamma of these models seem to have a nearly equal possibility of being distributed in each value within the range after restricting the integrated intensity of the Lyman β and Lyman γ lines. This might be because the correlation coefficient and the elasticity coefficient between the integrated intensity and the column mass, and also that between the integrated intensity and gamma, are not as large as those between the integrated intensity and the central pressure. We do not constrain all parameters but only parameters with clear biased distributions that show systematic tendencies for data to cluster in certain regions rather than being balanced or symmetric across the entire range..

Figure 3.16 shows the probability distribution of the central pressure after restricting the

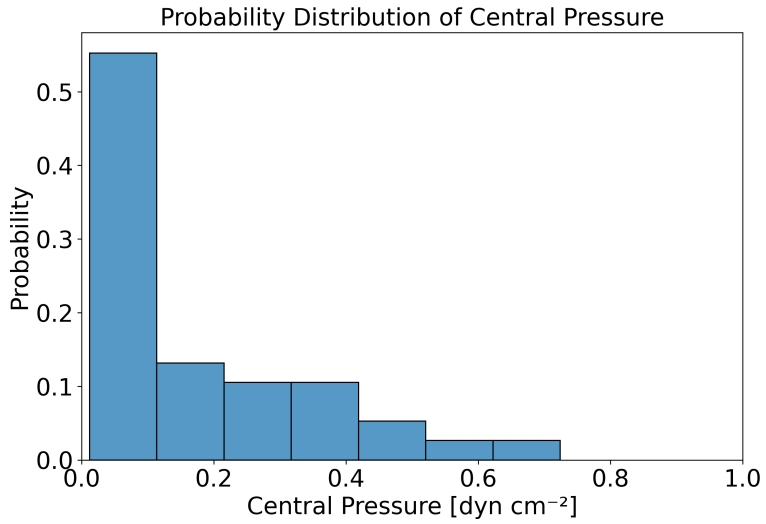

Figure 3.16: The probability distribution of the central pressure constrained by observation (Figure from Zhang et al. (2026b)).

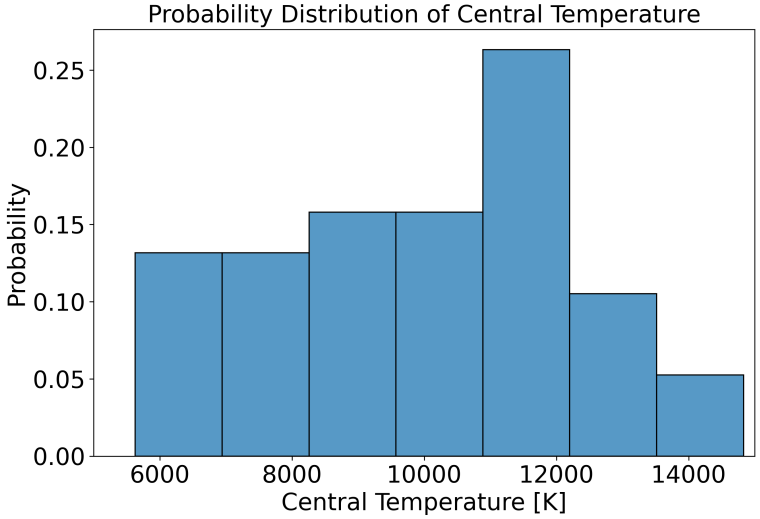

Figure 3.17: The probability distribution of the central temperature constrained by observation (Figure from Zhang et al. (2026b)).

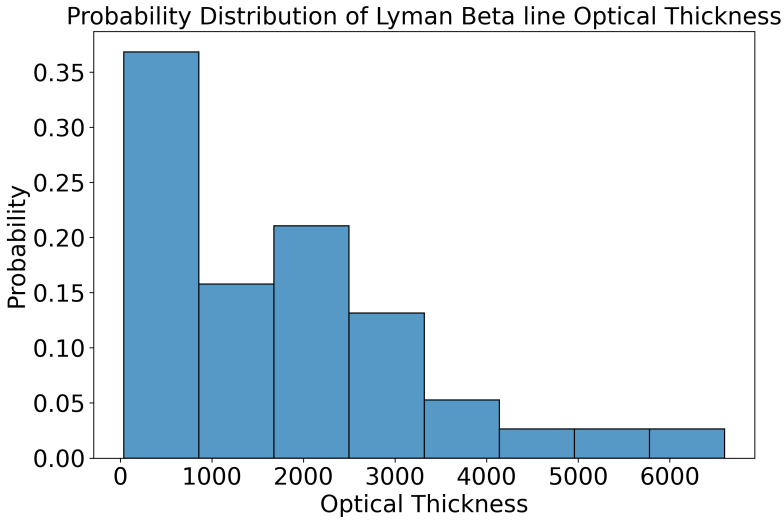

Figure 3.18: The probability distribution of the Lyman β line optical thickness constrained by observation (Figure from Zhang et al. (2026b)).

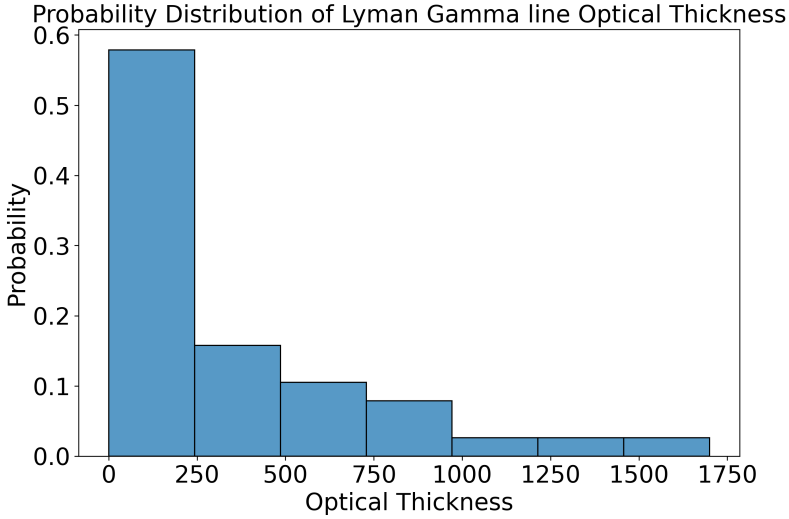

Figure 3.19: The probability distribution of the Lyman γ line optical thickness constrained by observation (Figure from Zhang et al. (2026b)).

models by considering the observed integrated intensities. The distribution is derived from the relative frequencies of central pressure values, calculated by counting how many models fall within each pressure interval and normalizing by the total number of accepted models. There are no models for values above 0.7 dyn cm^{-2}, and models with lower pressures are more frequent. Thus, central pressure is a good example of a parameter we can constrain.

Figure 3.17 shows the probability distribution of the central temperature after constraining the models by considering the observed integrated intensities. The possibility of values lying around the middle of the range of temperatures are slightly higher than other ranges of values. Nevertheless, other temperature values are likely. Therefore, we would not constrain the parameters with a distribution like that in Figure 3.17.

Since 95 % of the models that meet the restriction requirement of both lines have a central pressure below 0.48 dyn cm^{-2}, we can judge that the central pressure is below this value. For other parameters, we have to find other lines which have stronger relations with those parameters to constrain them in the future.

As shown in Figure 3.18 and Figure 3.19, we can also generate the probability distribution of Lyman β and Lyman γ optical thicknesses after constraining the models by considering the observed integrated intensities. It also shows a biased distribution. Since 95 % of the models that meet the restriction requirement have Lyman β line optical thickness below 4800 and Lyman γ line optical thickness below 1000, we can constrain the Lyman β line optical thickness and the Lyman γ line optical thickness by these values. The optical thickness is an output parameter of the PRODOP code, and these figures give us an indication of what the expected optical thickness is in these two lines. This result demonstrates that extremely optically thick models for Lyman β and Lyman γ lines are strongly excluded by the observations.

In summary, this method using non-LTE modelling results to constrain plasma parameters from observations has the potential to be extended to more lines. This will give better constraints on prominence parameters.

3.4 Discussion

We have investigated the most important parameters in the 2023 April 15th event for the formation of the Lyman β line and the Lyman γ line. The most important parameters are central temperature, central pressure, column mass, and the temperature gradient in the prominence-to-corona transition region, which we can see from Figures 3.8–3.15. The correlation coefficient describes how strong the relations of these parameters are with the quantities we study and the elasticity coefficient describes how sensitive the quantities are to the relative changes of these parameters. The parameters' effects among the Lyman β line and the Lyman γ line are quite similar. We can interpret how these influences take place.

The temperature affects the distribution of different energy levels' populations which then

affects optical thickness.

The pressure affects the density and level populations of hydrogen atoms and the density of electrons, and therefore affects the collisional contribution and the integrated intensity. The pressure should also affect the optical thickness through the density, but in the context of this event, we can see that the effect is not so strong in Tables 3.2 and 3.3.

The column mass affects the integrated intensity and the collisional contribution. The column mass affects the radiation term $(1-\varepsilon)\bar{J}$ in the expression of the source function (Eq. 3.1). When we change the column mass, the density of particles does not change much. The total intensity of the radiation field in a particular direction would have a positive correlation with column mass (larger volume). Therefore, the change in the column mass can affect the collisional contribution. Through source function, the column mass can affect the integrated intensity indirectly.

The value of gamma (corresponding to the steepness of the temperature gradient in the PCTR) affects the integrated intensity and the collisional contribution. When gamma is high, it means the temperature changes more quickly in the PCTR, which means the high-temperature part of prominence is less extended. Therefore, it impacts the temperature profile inside the prominence, and thus affects the integrated intensity and the collisional contribution to the source function.

3.5 Concluding Remarks

By comparing observed Lyman line intensities with the results of non-LTE modelling, this study extends our analysis presented in Chapter 2 of the first dedicated observation of an off-limb prominence by the Spectral Imaging of the Coronal Environment (SPICE) which took place on April 15, 2023. The prominence was observed a few hours before its eruption. We used a 1D non-LTE radiative transfer model (PRODOP) to investigate how different physical parameters affect the formation of the Lyman β and Lyman γ lines of hydrogen. The incident radiation for these lines was constrained and re-scaled using the SPICE full-disc mosaic observation from November 13, 2023, providing a more realistic boundary condition for the radiative transfer calculations.

We introduced parallel coordinate plots as an effective tool for visualizing multi-parameter relationships with different properties. To demonstrate the relevance of this toolkit, we confirmed the well-known correlation between Hα intensity and emission measure, but also revealed an increase of Hα intensity with temperature which is not discussed in previous studies. We also use the parallel coordinate plot and the elasticity coefficient to further compare relations among different parameters. The emission measure has the strongest relation with Hα intensity, and the Hα intensity is much more sensitive to the emission measure's relative change than other parameters.

With respect to the SPICE prominence observations discussed in Chapter 2 and summarised here, our results further show that central temperature, central pressure, column mass, and PCTR temperature gradient are important parameters for the formation of the Lyman β and Lyman γ lines. In addition, one can also use the relations between these parameters and the observed integrated intensities to constrain the parameter ranges. As a result, we find that the central pressure of this prominence should be below 0.48 dyn/cm^2, Lyman β line optical thickness should be below 4800 and Lyman γ line optical thickness should be below 1000.

This chapter thus bridges the observational analysis presented in Chapter 2 with the physical interpretation enabled by non-LTE radiative transfer modelling. While Chapter 2 revealed the diagnostic potential of SPICE Lyman lines and highlighted the limitations of observational data alone in constraining key plasma parameters, the present chapter demonstrates how modelling can break this by establishing quantitative relationships between observable line properties and underlying physical conditions. The parameter constraints obtained here (particularly for central pressure and optical thickness) provide the first step toward a comprehensive characterisation of pre-eruptive prominence conditions. Building upon this foundation, the next chapter will extend this methodology to generate parameter maps. This approach will enable constraints on prominence parameters and allow us to investigate their distributions by maps.

Chapter 4

Prominence Plasma Parameters Maps

In this chapter, we will introduce prominence plasma parameters maps inferred from Lyman β and Lyman γ observations and Non-LTE modelling. We will create models which simultaneously give a reasonable match with the observed intensities in both lines. Unlike previous approaches, our method uses contribution functions to guide the optimisation of temperature and pressure profiles. Our approach enables a physically constrained and consistent match to both spectral lines.

Most contents of this chapter (i.e. text, tables and figures) come from Zhang et al. (2026c, submitted) and are written or created by me unless otherwise stated. I developed the method to create parameter maps. Nicolas Labrosse gave opinions about contents of figures and texts to improve the quality of the paper. Therese A. Kucera and Susanna Parenti also gave useful comments to improve the paper and make it more readable. Therese A. Kucera made the flow chart in this chapter much clearer to explain the whole process.

Solar prominences are structures of cool and dense plasma suspended within the hot solar corona. They are pivotal to understanding the dynamics of the solar atmosphere. They are frequently associated with coronal mass ejections (CMEs), which can significantly influence space weather (Parenti, 2014a). Investigating the physical conditions within these structures, such as their temperature, pressure, column mass, and velocity, is crucial to advancing our understanding of solar physics and enhancing space weather forecasting.

The determination of these fundamental prominence parameters is primarily based on spectroscopic diagnostics. Temperatures of optically thin plasma, like the prominence-corona transition region (PCTR) and solar jets, can be estimated using Differential Emission Measure (DEM) or filter–ratio techniques with instruments such as SOHO/SUMER or Hinode/XRT (e.g., Parenti, 2014a; Mulay et al., 2017). The electron density within prominences core can be inferred from diagnostics such as Thomson scattering measurements by instruments like LASCO (e.g., Susino et al., 2019), and the ratio of the Na I D_2 5890 Å and Sr II 4078 Å lines(Wiehr et al., 2016; Stellmacher and Wiehr, 2017). Accurately interpreting diagnostics within the non-local thermodynamic equilibrium (non-LTE) environment of prominences often requires the use of non-LTE

radiative transfer modelling for specific spectral lines (e.g., Labrosse et al., 2010; Parenti, 2014a; Labrosse, 2015; Heinzel, 2015). Early work, such as that by Vernazza et al. (1981), laid the groundwork for understanding radiative transfer in the solar atmosphere, emphasizing the diagnostic power of hydrogen lines. Gunár et al. (2008) demonstrated that a multi-thread model, incorporating small line-of-sight velocities for each thread, can explain the observed asymmetries in Lyman line profiles. Schwartz et al. (2015) employed a statistical comparison between synthetic and observed profiles to constrain key parameters of prominence fine structures, such as column mass and central temperature. The synthetic profiles in these studies were generated using two-dimensional (2D) multi-thread non-LTE models, which assume magnetohydrostatic (MHS) equilibrium and include a PCTR. The PRODOP code, used in this study, is a 1D non-LTE radiative transfer code specifically designed for hydrogen, calcium, helium and magnesium lines in solar prominences and includes consideration of Doppler dimming/brightening effect (Gouttebroze and Heinzel, 2002; Labrosse et al., 2007; Levens and Labrosse, 2019).

The hydrogen Lyman lines (transitions to the ground state, n=1) serve as powerful diagnostics for prominence plasma. These extreme ultraviolet (EUV) lines are particularly sensitive to plasma properties due to their formation across various optical depths within the prominence. The Lyman photons discussed here mainly interact with neutral hydrogen through resonant bound–bound absorption rather than direct ionisation of ground-state hydrogen, since the Lyman β and Lyman γ photon energies are below the hydrogen ionisation threshold. Ionisation and recombination are instead included in the NLTE statistical equilibrium equations through the bound–free transitions, so the coupling between Lyman line radiation and the neutral/ionised hydrogen populations is treated within the radiative transfer model.

While Lyman α provides a fundamental diagnostic, higher members of the series, such as Lyman β and Lyman γ, offer complementary insights. These higher Lyman lines are formed higher up in the atmosphere compared to Lyman α, thereby probing varying thermodynamic conditions ranging from the cool, dense core of the prominence to the hotter PCTR region (Vial et al., 2007; Heinzel et al., 2001). The ratio of Lyman α to Lyman β intensity has been shown to be sensitive to physical and geometrical properties of the fine structure and mass motions within prominences (Vial et al., 2007; Gunár et al., 2010). Recent studies have further highlighted the diagnostic potential of multi-wavelength and multi-species observations, such as simultaneous analysis of Hα and Mg II lines, to constrain temperature, microturbulence, and optical thickness in quiescent prominences through 1D non-LTE inversions (Barczynski et al., 2021; Jejčič et al., 2022). Such approaches are also being extended to eruptive prominences observed by instruments like Metis/Solar Orbiter, which combine visible-light and UV diagnostics (Heinzel et al., 2023; Jejčič et al., 2022). The formation of Lyman β and Lyman γ lines is sensitive to parameters such as temperature, pressure, and column mass based on previous research in Zhang et al. (2026a) (chapter 2) and Zhang et al. (2026b) (chapter 3), and also Gouttebroze et al. (1993); Heinzel et al. (1994). By analysing these lines with non-LTE radiative transfer models, we have

the potential to infer variation of these physical properties across prominence structures.

Furthermore, combined observations in Hα and white-light during solar eclipses have enabled the mapping of electron density, effective thickness, and temperature in quiescent prominences, revealing gradients in ionisation structure due to incident radiation (Jejčič et al., 2014). These multi-wavelength diagnostics provide a crucial observational foundation for validating and refining non-LTE models of prominence plasma.

In Chapter 2 (Zhang et al., 2026a), we presented the first comprehensive analysis of the Solar Orbiter/SPICE off-limb prominence observation of 15 April 2023 (SPICE Consortium et al., 2020), focusing on the spatial and temporal evolution of the Lyman β and Lyman γ line profiles during the pre-eruptive and eruptive phases. By comparing the integrated intensity and line width distributions in prominence, disc, and coronal regions, Chapter 2 (Zhang et al., 2026a) revealed variations indicative of dynamic changes in density, temperature, and optical thickness, and introduced a geometric method to derive radial velocities of eruptive filaments from paired Hα images. However, the study also demonstrated that observational diagnostics alone cannot uniquely constrain the underlying physical conditions of the prominence plasma, motivating detailed non-LTE radiative transfer modelling. In chapter 3 (Zhang et al., 2026b), we performed detailed 1D non-LTE radiative-transfer modelling (PRODOP) with incident radiation constrained using a SPICE full-disc mosaic, to investigate how key physical parameters control the formation of the Lyman β and Lyman γ lines. Chapter 3 (Zhang et al., 2026b) introduced the parallel coordinate plot and the elasticity coefficient analysis to explore multi-parameter relations and sensitivities, confirmed the strong relation between Hα intensity and emission measure (and revealed an additional temperature dependence of Hα intensity), and demonstrated that central temperature, central pressure, column mass and the PCTR temperature gradient are primary factors shaping the emergent Lyman profiles. By combining the observed intensities with the modelling, chapter 3 (Zhang et al., 2026b) further provides a technique to constrain the central pressure of prominence parameter with an upper limit ~ 0.48 dyn cm^{-2}. Together, Chapter 2 and 3 provide the empirical and theoretical foundation for the analysis presented in this Chapter.

In the present study we use data from the first dedicated off-limb prominence observation performed by the SPICE instrument aboard Solar Orbiter on April 15, 2023. Our primary objective is to derive key plasma parameters, such as temperature, pressure, and column mass, within the observed prominence region by the Lyman β and Lyman γ lines observation. By applying a 1D non-LTE radiative transfer code to compare computed intensities with observed SPICE integrated intensities, we aim to construct detailed parameter maps of the prominence. The analysis of the pre-eruptive phase of the prominence will provide valuable insights into the thermodynamic and dynamic properties that set the stage for solar eruptions, thereby contributing to our understanding of solar activity and its implications for space weather.

4.1 Observations

SPICE has contributed directly to Solar Orbiter's objective of investigating coronal mass ejection (CME) initiation by performing coordinated prominence observations during 10-hour campaigns conducted near perihelion. In the prominence observation on April 15, 2023, we used limb-pointing geometries, allowing the combination of SPICE's spectroscopic diagnostics with high-resolution imaging from the Extreme Ultraviolet Imager (EUI). We have SPICE observation during 01:03–14:58 UT, 15 April 2023, and use pre-eruption rasters from 07:03 UT to 08:09 UT to analyse the event in this Chapter.

we use SPICE data version 5.0 to analyse the event (DOI:10.48326/idoc.medoc.spice.5.0). Analysis of the SPICE data suggests the prominence spanned an altitude range of approximately 20000 km $\sim$ 60000 km (Chapter 2; Zhang et al., 2026a).

4.2 Prominence model atmosphere

In Figure 4.1, we show the process adopted here to construct prominence models that are close to the observed integrated intensities of both Lyman β and the Lyman γ line. The general concept is that we identify the best matched models of the observed integrated intensities of both Lyman β and the Lyman γ line and select the one with the lower χ^2 for the Lyman β and Lyman γ observed intensities. After that, we slightly adjust the model using the other model that has the best match with the other line to make it closer to the observed integrated intensities of both Lyman β and the Lyman γ line. We will generate new models that can be potentially the best match to observed integrated intensities of both Lyman β and the Lyman γ line based on different possible coefficient sets. We will calculate new models and find the best coefficient set that can give a lowest average χ^2 value for all pixels. There is inevitably some degeneracy in this procedure, because different combinations of plasma parameters can produce similar Lyman β and Lyman γ integrated intensities. Therefore, the resulting model should not be interpreted as a unique solution for each pixel. However, the method is not a local gradient-based optimisation starting from a single initial model. Instead, it starts from a set of random models covering the allowed parameter space and tests a finite set of possible coefficient combinations. The final coefficient set is selected by comparing the resulting model intensities with the observations over all pixels.

As a first approach, we divide the intensity map of the Lyman β and the Lyman γ line in the prominence region (the red box region in Figure 3.1) into 9 regions to test our method more efficiently. Figure 4.2 shows the mean intensity for each of these regions.

We generate 1000 random models based on our estimate of parameters' ranges in Table 4.1. These ranges are from chapter 3 (Zhang et al., 2026b). We use the Spectral Imaging of the Coronal Environment (SPICE) full-disc mosaic from November 13, 2023 to constrain the in-

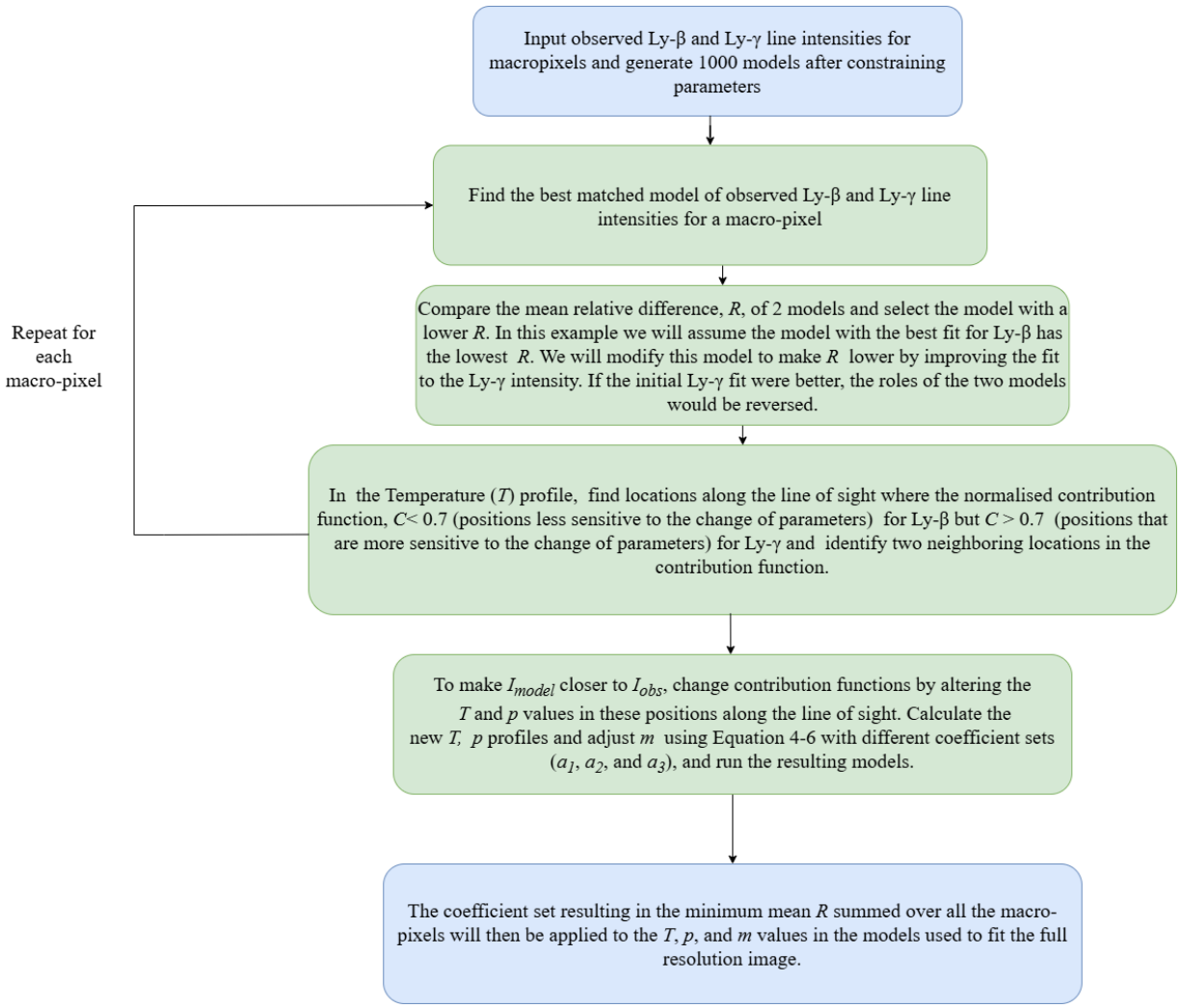

Figure 4.1: The process to construct initial set of prominence models that are close to observations of the Lyman β and Lyman γ lines (Figure from Zhang et al (2026c, submitted)).

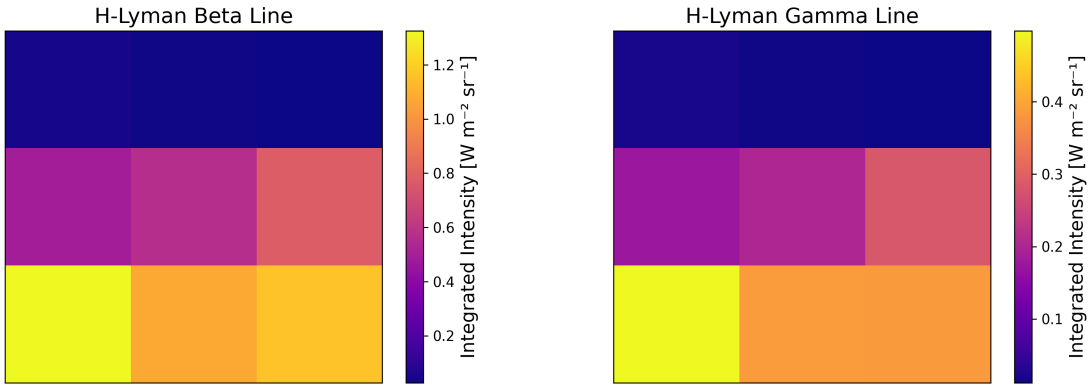

Figure 4.2: The 9-pixel intensity map of the Lyman β and the Lyman γ line in the prominence region (the red box region in Figure 3.1). For each pixel, the intensity is the mean intensity of that region (Figure from Zhang et al (2026c, submitted)).

Table 4.1: The parameter ranges for different variables.

Parameter	Range
Central Temperature	5000 K $\sim$ 15000 K
Surface Temperature	100000 K
Central Pressure	0.01 dyn cm^{-2} $\sim$ 0.48 dyn cm^{-2}
Surface Pressure	0.01 dyn cm^{-2}
Column Mass	1.4×10^{-7} g cm^{-2} $\sim$ 1.4×10^{-5} g cm^{-2}
Γ (Temperature Gradient)	2 $\sim$ 10
Altitude	20000 km $\sim$ 60000 km
Radial Velocity	0 km s^{-1} $\sim$ 40 km s^{-1}
Microturbulent Velocity	5 km s^{-1}

cident radiation (the same as chapter 3 (Zhang et al., 2026b)). We fix the surface temperature because moderate changes of it would not affect the result much. We fix the surface pressure at 0.01 dyn cm^{-2}, which is a representative value for the low pressure outer boundary of PCTR prominence. The microturbulent velocity is fixed at 5 km s^{-1}, which is also a representative value for prominence plasma. Our procedure to obtain the model with the closest intensity to both Lyman β and Lyman γ lines is:

(1) For each pixel, we find model A and model B to prepare for the construction of a new model. Model A is the model that has the closest Lyman β intensity with observation among the 1000 random models. Model B is the model that has the closest Lyman γ intensity with observation among the 1000 random models. The comparison of best matched intensity map and observation for the red box region in Figure 3.1 is shown in Figure 4.3. The calculated intensity maps match quite well with the observation. This is because we have constrained the range of values for the central pressure based on our results from chapter 3 (Zhang et al., 2026b), based on our observation that the elasticity coefficient between the integrated intensity and the central pressure is high. This constraint is important because central pressure strongly affects the Lyman-line integrated intensities. Without this constraint, many random models would fall outside the observed intensity range, so fewer models would be available to match each observed pixel. The matched maps would then have lower effective detail, and some of the spatial structures visible in Figure 4.3 could disappear. Therefore, the pressure constraint makes the model grid more representative of the observed prominence and improves the reliability of the subsequent model construction.

As a result, the calculated integrated intensities of our 1000 models fall in the range of integrated intensities in the observation. But in this step, in the lower panels of Figure 4.3, pixels in the same position of the Lyman β intensity map and the Lyman γ intensity map are actually from different models with different plasma parameters. We need to construct new models which can match observations of both Lyman β and Lyman γ lines simultaneously;

(2) In this step, we will construct new temperature profiles, new pressure profiles, and set column mass for new models. From our previous results in chapter 3 (Zhang et al., 2026b), we know that temperature, pressure, and column mass are key parameters of Lyman β and Lyman γ

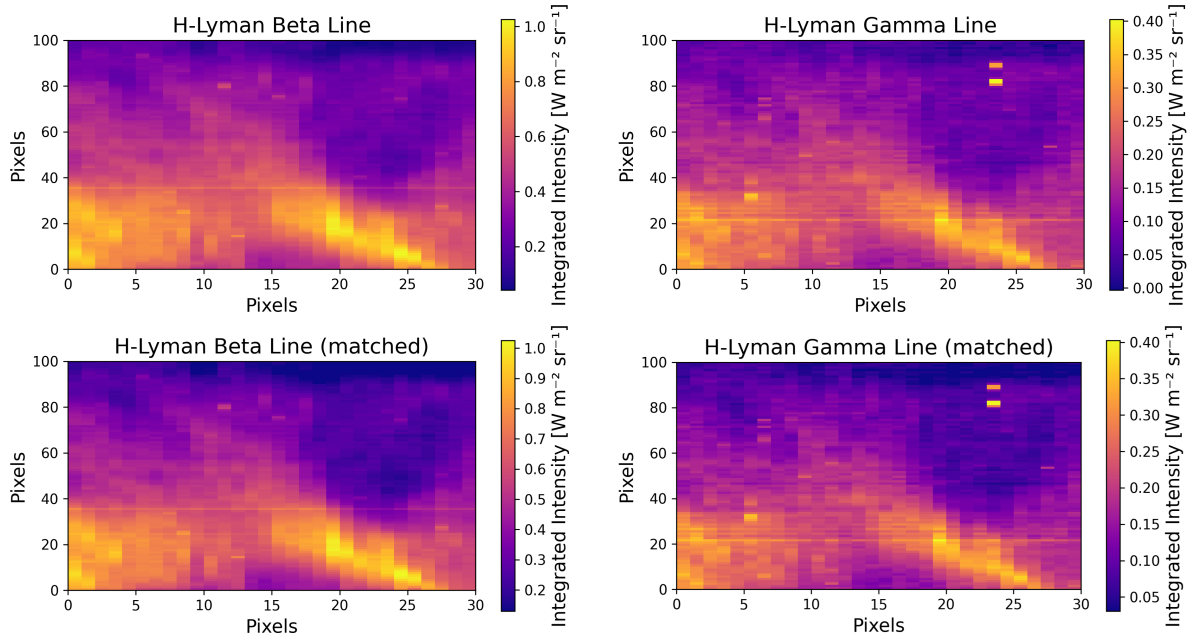

Figure 4.3: Comparison of best matched intensity map and observation for the red box region in Figure 3.1. The upper panels are observational maps and the lower panels are best matched synthetic maps. In the lower panels, pixels in the same position of the Lyman β intensity map and the Lyman γ intensity map are actually from different models (Figure from Zhang et al (2026c, submitted)).

line formation for the prominence event in April 15, 2023. Therefore, we focus on constructing these three parameters to match the observation. The new temperature and pressure profiles from the prominence surface to the prominence centre (the green line in Figure 4.4) are obtained by following steps:

1. we calculate the χ^2 value of Lyman β and Lyman γ observed intensity (I_{β_obs}, I_{γ_obs}) and calculated intensity (I_{β_model}, I_{γ_model}) for each pixel in model A and model B by Equation 4.1.

$$\chi^2 = \left(\frac{I_{\beta,\mathrm{obs}} - I_{\beta,\mathrm{model}}}{\sigma_\beta}\right)^2 + \left(\frac{I_{\gamma,\mathrm{obs}} - I_{\gamma,\mathrm{model}}}{\sigma_\gamma}\right)^2. \tag{4.1}$$

   For each pixel, We will identify the smaller χ^2 model (model A or model B) and build a new model to make χ^2 of this pixel lower in the following steps based on this model;

2. We retrieve the contribution functions (C) for the Lyman β line (Model A) and the Lyman γ line (Model B) as a function of position from prominence surface to prominence centre, and normalize them by their respective maxima. The contribution function describes how a given location inside the prominence contributes to the line intensity and it is an output of the model. The contribution function is expressed as in Equation 4.2 (Carlsson and

Stein, 1997), where C is the contribution function of the spectral line under consideration, S is the source function, τ is the optical depth, and χ is the absorption coefficient:

$$C = S\exp(-\tau)\,\chi \tag{4.2}$$

The integrated intensity can be expressed as the integral over position in the slab (z) of the contribution function:

$$I = \int C(z)dz = \int S(z)\,e^{-\tau(z)}\chi(z)\;dz \tag{4.3}$$

The contribution function thus represents the local contribution of each layer to the emergent intensity, and depends upon the source function $S(z)$, the monochromatic opacity per unit length $\chi(z)$, and the exponential attenuation factor $e^{-\tau(z)}$ accounting for absorption along the line of sight.

In Figure 1.8, we can see that, in the PRODOP code, the prominence is modelled as a 1D slab oriented vertically above the solar surface, incorporating the prominence-corona transition region (PCTR). In Figure 4.4, for each panel, the left side of X-axis corresponds to the prominence surface and the right side of X-axis to the prominence centre (note that our prominence model atmospheres are symmetrical and thus only one half of the model is shown).

3. For each pixel, we will find positions where we want to modify within the slab using temperature and pressure profiles based on χ^2 of Model A and B. For the model with the smaller χ^2, one of the lines (Lyman β or Lyman γ) is already well matched but the other line is not, so we avoid modifying positions of new temperature and pressure profiles where changes would significantly affect the intensity of the well matched line. The line which is not well matched is the target of further adjustment, so we modify temperature and pressure profiles where the intensity of this line is most sensitive. At positions with a high value of contribution function, the change of parameters would make the intensity change significantly; while, at positions with low value of contribution function, it would not. Therefore, at locations where the normalized contribution function is below 0.7 (positions that are less sensitive to the change of parameters) for the smaller χ^2 model but above 0.7 (positions that are more sensitive to the change of parameters) for the larger χ^2 model, we assign the temperature and pressure from the smaller χ^2 model, denoted as T_1 and p_1. We aim to further reduce χ^2 of the model. We then examine the contribution functions for the larger χ^2 model. If the larger χ^2 model is model A, we check the Lyman β line; if the larger χ^2 model is model B, we check the Lyman γ line. The temperature and pressure at the location where the contribution function reaches its maximum is denoted as $T_{\max}$ and $p_{\max}$.

4. We will construct new temperature and pressure profiles and set column mass for new models in this step. New temperature and pressure profiles will produce better match intensity with observations. We check values of two neighbour positions of T_1 and p_1 in the temperature or pressure profile of the smaller χ^2 model. In the smaller χ^2 model, we check the calculated intensity of either the Lyman β line or Lyman γ line, whichever is the worst match. If the calculated intensity is smaller than observed intensity of that line, we need to increase contribution functions, and the neighbouring value of T_1 (or p_1), which can provide $|T - T_{\max}|$ or $|p - p_{\max}|$ lower than $|T_1 - T_{\max}|$ or $|p_1 - p_{\max}|$, is denoted as T_2 (or p_2); if the calculated intensity is larger than observed intensity of that line, we need to decrease contribution functions, and the neighbouring value of T_1 (or p_1), which can provide $|T - T_{\max}|$ or $|p - p_{\max}|$ larger than $|T_1 - T_{\max}|$ or $|p_1 - p_{\max}|$, is denoted as T_2 (or p_2).

   The temperature and pressure profiles of a new model is calculated by Equations 4.4 and 4.5, i.e. a linear combination of T_1 and T_2 (or p_1 and p_2).

$$T_{\text{new}} = T_1 + a_1 \cdot (T_2 - T_1) \tag{4.4}$$

$$p_{\text{new}} = p_1 + a_2 \cdot (p_2 - p_1) \tag{4.5}$$

   We will repeat the same calculation for all positions that satisfy the condition in the T and p profiles. Since we check neighbour values that are from original T and p profiles, so the order of calculation would not affect results.

   We restrict the coefficients a_1 and a_2 in Equations 4.4 and 4.5 to the range $0 - 1/2$. This choice ensures that the resulting temperature (or pressure) profiles remain closer to T_1 (or p_1), which belong to the temperature or pressure profile with a smaller χ^2. At the same time, the coefficients are not allowed to be negative, because this shifts T_{new} away from the desired model that has temperature and pressure profiles close to both model A and model B. The smaller χ^2 model is already the best matched model of the Lyman β line or the Lyman γ line. We choose to modify values where the normalised contribution function values (model A, Lyman β line; model B, Lyman γ line) are below 0.7 for the smaller χ^2 model and higher than 0.7 for the larger χ^2 model, because we want to reduce the change to the smaller χ^2 model and increase the change to the larger χ^2 model. If there is no neighbouring value which satisfy the condition, then $a_1 = a_2 = 0$.

   In this step, the values of a_1 and a_2 have not been determined. We test them by steps of 1/6: 0, 1/6, 1/3, 1/2. We calculate a new value for the column mass of the new model using Eq. 4.6, as column mass is also an important parameter for the formation of both Lyman β and Lyman γ (Chapter 3; Zhang et al., 2026b). In Eq. 4.6, m_1 is the column mass of the

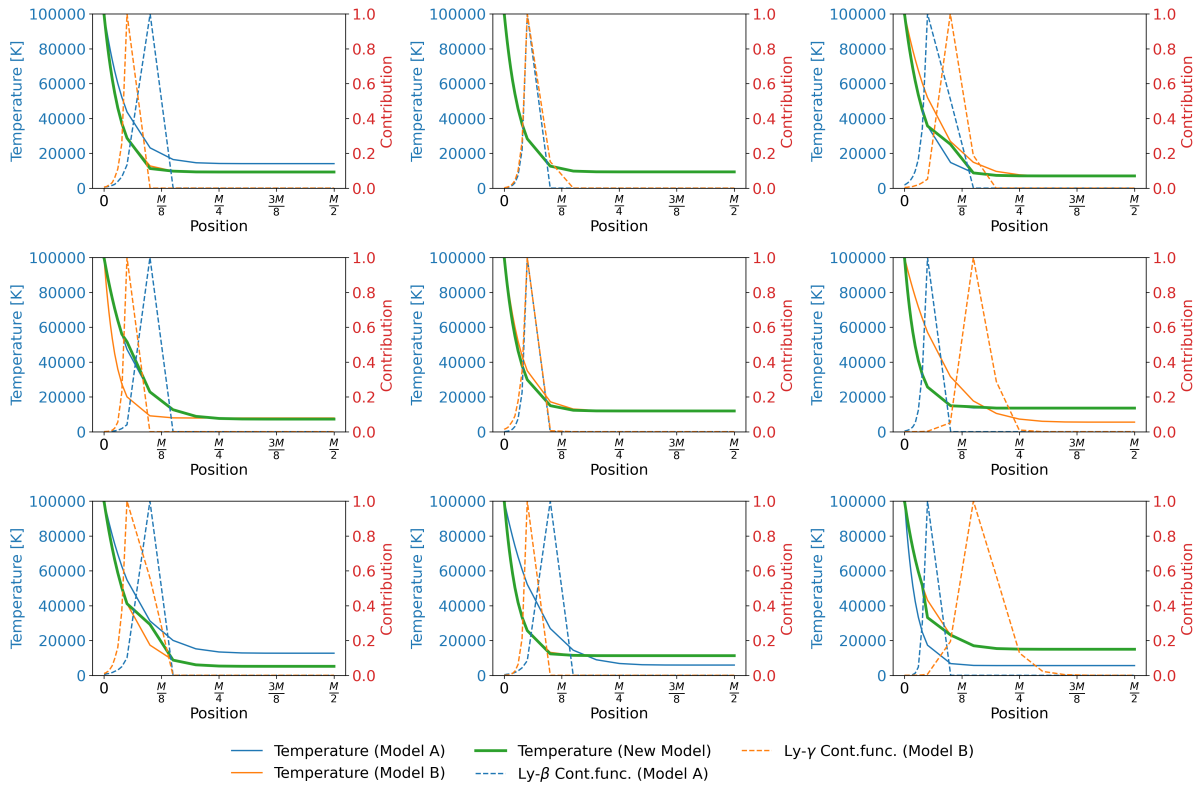

Figure 4.4: Temperature profiles of Model A and Model B and contribution functions of Model A for the Lyman β line and Model B for the Lyman γ line. The 9 panels correspond to 9 pixels in Figure 4.2. The solid lines are temperature profiles and the dashed lines are contribution functions. The blue lines are Model A and the orange lines are Model B. The green line is the temperature profile of the new model we construct. M is the column mass of the model, which is along the direction of the line of sight in Figure 1.8. Contribution functions are normalized by the maximum. In this figure, $a_1 = a_2 = 1/2$ (Figure from Zhang et al (2026c, submitted)).

smaller χ^2 model and m_2 is the column mass of the other model. a_3 varies from -1/2 to 1/2. We do not consider values larger than 1/2 or lower than -1/2 because this will make either the Lyman β and Lyman γ line intensity change a lot from original intensity of a model. We also test different values of a_3 by an interval of 1/6: -1/2, -1/3, -1/6, 0, 1/6, 1/3, 1/2. In practice, we do not need to test all values since the new column mass $m_{\rm new}$ would be below 0 with some values of a_3 below 0. We discard these values directly. We use interval 1/6 after considering both the running time of the code and accuracy of the result and find a balance. The result would be more accurate when the interval is smaller, but the running time would be shorter when the interval is larger;

Column mass primarily controls the overall density scale and geometrical thickness of the model atmosphere. For this reason, varying the column mass within a wider range does not immediately force the local plasma conditions to deviate strongly from those of Models A and B but it changes the amount of emission. By contrast, the temperature and pressure have a much more direct influence on the formation of the Lyman lines; therefore the coefficients a_1 and a_2 must be restricted to a narrower range to avoid a large change in integrated intensity of both Lyman β and Lyman γ lines. This is why the allowed interval for a_3 in Eq. 4.6 is chosen to be broader than that for a_1 and a_2.

$$m_{\rm new} = m_1 + a_3 \cdot (m_2 - m_1) \tag{4.6}$$

In Figure 4.5, we can take the lower-right macro-pixel in Figure 4.4 as an example. In this macro-pixel, after comparing χ^2 of model A and model B, we find that model B is the model with smaller χ^2, so we proceed using this model. Then, we will try to construct new temperature and pressure profiles to make χ^2 lower. We will find locations where the normalized contribution function is below 0.7 for model B but above 0.7 for model A. As shown in Figure 4.5, there is only one position which satisfies the condition in this macro-pixel (For other macro-pixels, positions which satisfies the condition can be more or can be zero). We assign the temperature from model B in that position, denoted as T_1. From this figure, we can see that T_{max} of model A is lower than T_1. In model B, the Lyman γ line matches the observations well while Lyman β does not. We also check that the calculated intensity of Lyman β is less than the observed intensity of Lyman β. We need to make T_1 closer to T_{max} to increase contribution function in that position so as to increase the calculated intensity of Lyman β. So, from two neighbour positions of T_1, we choose to the right as T_2. We obtain T_{new} by Equation 4.4. In the example, $a_1 = a_2 = 1/2$, this is just one of the values we will test. For the pressure profile, we will also calculate the new one by the same method.

(3) In this step, we will find the best coefficient set by running models constructed in step 2. We calculate the line intensity for models generated by Step 2. These models are combination of

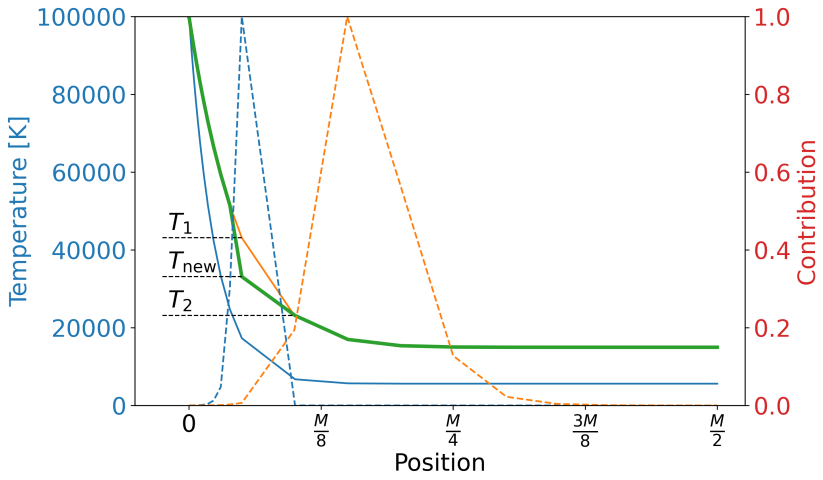

Figure 4.5: The lower-right panel of Figure 4.4 showing the details of the changes in the temperature profile (Figure from Zhang et al (2026c, submitted)).

different values of a_1, a_2 and a_3. We compare the calculated intensity with the observed intensity by χ^2_{avg} value for all 9 pixels by Equation 4.7. In Equation 4.7, N_{Pix} is the number of pixels. We will find the model with the least χ^2_{avg} value with the observed intensity. This is the model that we ultimately select as it simultaneously has the closest Lyman β and Lyman γ intensity with observation.

$$\chi^2_{\text{avg}} = \frac{1}{N_{Pix}} \sum_{i=1}^{N_{Pix}} \left[\left(\frac{I_{\beta,\text{obs},i} - I_{\beta,\text{model},i}}{\sigma_{\beta,i}} \right)^2 + \left(\frac{I_{\gamma,\text{obs},i} - I_{\gamma,\text{model},i}}{\sigma_{\gamma,i}} \right)^2 \right]. \tag{4.7}$$

For the red box region in Figure 3.1, the final results of our method are:

$$a_1 = 0, a_2 = 0, a_3 = 0$$

$$R_{avg} = \frac{1}{2N_{Pix}} \sum \left(\frac{|I_{\beta_obs} - I_{\beta_model}|}{I_{\beta_obs}} + \frac{|I_{\gamma_obs} - I_{\gamma_model}|}{I_{\gamma_obs}} \right) \tag{4.8}$$

This coefficient set gives a R_{avg} of 5 % between models and observations for the 9-pixel intensity map. R_{avg} is calculated by Equation 4.8. The model calculations were run on a machine with an Intel Core i7-10875H processor at 2.3 GHz. The running time of the code is about 4 h (1576 models have been calculated). The coefficient set seems to show that the construction of new temperature and pressure profiles is not necessary because all the results comes from the smaller . We think there are reasons for this result. One is that the PRODOP code can already match the Lyman β and Lyman γ intensities with observations quite well simultaneously. Another reason is that the Lyman β and Lyman γ intensities are actually quite sensitive to the change of parameters like temperature, pressure and column mass. The interval of 1/6 for each

coefficient may be too large: a smaller interval could lead to a slightly different coefficient set. Nevertheless, the R_{avg} of 5 % between models and observations is good enough for our purpose, and the selected models are adequate. We can conclude that in this particular context, the selected coefficient set is the best one. The steps that we have taken to select these coefficients will be important when we extend the method to other lines that have different line formation mechanisms.

We also calculate the R_{avg} value between the calculated intensity and original intensity map by the same coefficient set based on Equation 4.8. The result is 8 %, which is quite close to the result of the 9-pixel intensity map. The 9-pixel intensity map is a good approach to find the best coefficient set, as the running time prevents the use of the original intensity map to compute the coefficient set. The comparison of calculated intensity by the best coefficient set and observation for the red box region in Figure 3.1 is shown in Figure 4.6. From this figure, we can see that the calculated integrated intensity maps are quite close to observations for both lines.

The difference between Figures 4.3 and 4.6 is that, in Figure 4.3, the calculated Lyman β and Lyman γ intensities at the same spatial position generally originate from different models: Model A for Lyman β and Model B for Lyman γ. In Figure 4.6, both intensities at each spatial position are calculated from the same model. Since the best coefficient set is $a_1 = a_2 = a_3 = 0$, no interpolation of the temperature profile, pressure profile, or column mass is applied. The final model at each pixel is therefore the smaller χ^2 model, either Model A or Model B.

4.3 Parameter maps

We obtain the plasma parameters for the models generated by the best coefficient set. For the most important parameters in the Lyman β and Lyman γ line formation, we present parameter maps in Figure 4.7.

The pixel-to-pixel variations in Figure 4.7 should not be interpreted directly as spatially resolved prominence microstructure. Each pixel is inverted independently, without considering neighbouring pixels. In addition, different combinations of plasma parameters can reproduce similar Lyman β and Lyman γ integrated intensities. The small-scale variations in the maps therefore reflect the degeneracy of the model grid. We consequently focus on the broad parameter ranges and large scale spatial trends rather than on individual pixels.

We also note that column mass is not equivalent to local number density. It is an integrated quantity, and depends on both density and geometrical thickness along the line of sight. Moreover, the mean pressure and mean temperature are averages over the column mass coordinate. Although the local quantities satisfy $p = nk_{\mathrm{B}}T$, in general $\overline{p} \neq k_{\mathrm{B}}\overline{n}\,\overline{T}$. Therefore, the ranges of column mass and mean temperature cannot be multiplied directly to predict the range of mean pressure.

In Table 4.2, we summary ranges of parameter maps. The variation from pixel to pixel in

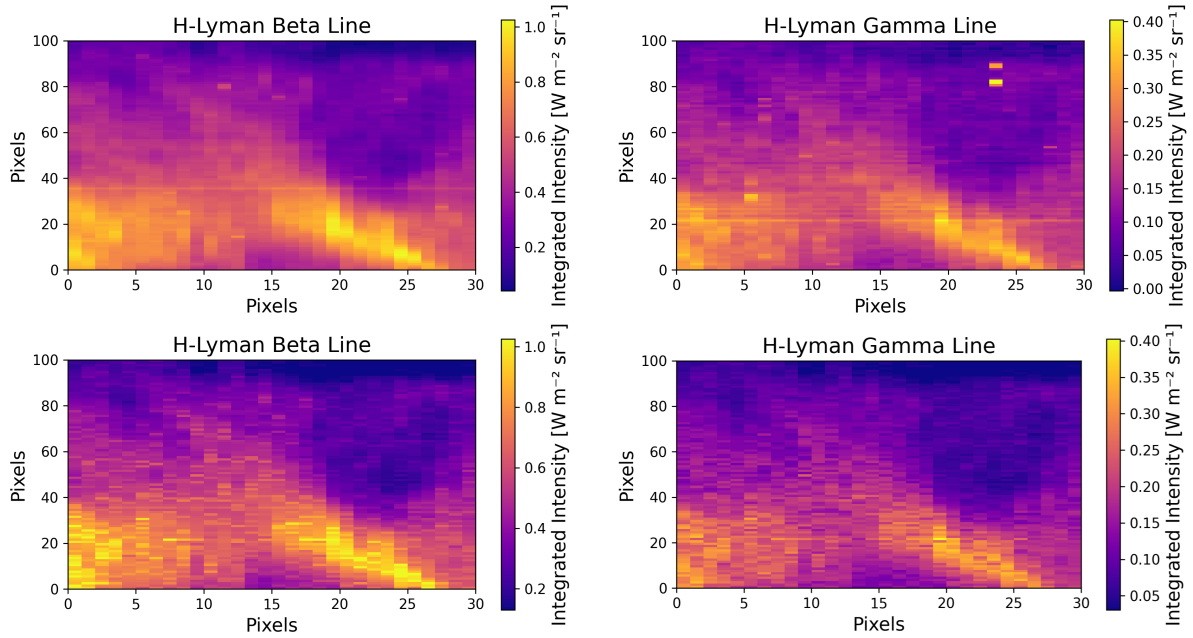

Figure 4.6: The comparison of calculated intensity by the best coefficient set and observation for the red box region in Figure 3.1. The upper panels are observational maps and the lower panels are synthetic maps. In the lower panels, pixels in the same position of the Lyman β intensity map and the Lyman γ intensity map are from same models (Figure from Zhang et al (2026c, submitted)).

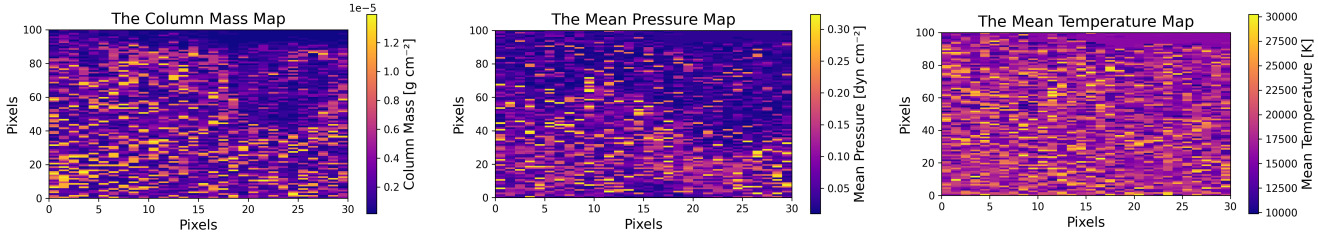

Figure 4.7: Parameter maps for the most important parameters in the Lyman β and Lyman γ line formation (Figure from Zhang et al (2026c, submitted)).

Table 4.2: Ranges of parameter maps provided by the best coefficient set

Parameter	Range
Column Mass [$\mathrm{g\,cm^{-2}}$]	$1.6\times10^{-7}\sim1.4\times10^{-5}$
Mean Pressure [$\mathrm{dyn\,cm^{-2}}$]	$0.01\sim0.32$
Mean Temperature [K]	$9885\sim30238$

parameter maps is due to the uncertainty associated with the degeneracy of the solutions. The estimation of uncertainty of this method requires some other works and they will be presented in the coming paper Zhang et al. (2026c, submitted). Different sets of parameters can result in the same integrated intensities in some lines. For instance, high pressure and low temperature, or low pressure and high temperature, can lead to the same integrated intensity of Lyman β line. If we focus on a region that has similar Lyman β intensity in Figure 4.6 and in Figure 4.7, we can verify this. The parameter values are within the ranges quoted by Parenti (2014a). These values are also consistent with the typical plasma parameters for quiescent prominences summarized in Table 1 by Labrosse et al. (2010). We can compare structures in Figure 4.6 with Figure 4.7. For the column mass map and the mean pressure map, we can see that the low column mass regions and the low mean pressure parts are roughly low intensity parts in Figure 4.6 and the high column mass parts and high mean pressure parts are roughly high intensity parts.

We choose to study mean pressure and mean temperature because they present a useful overall picture of the prominence. In chapter 3 (Zhang et al., 2026b), we study the effect of central temperature and central pressure with integrated intensity. Since we fix the surface temperature and surface pressure, the mean pressure and mean temperature are directly related to central temperature and central pressure. Therefore, they have similar relationships with integrated intensity. For the mean temperature map, the structures are not so obvious, and we can only distinguish the upper-right part. There are two reasons for this. One is that the Lyman β and Lyman γ line intensities are not so sensitive to mean temperature compared with column mass and mean pressure (Chapter 3; Zhang et al., 2026b). The difference of the Lyman β and Lyman γ line intensities in the red box region is not large enough to show the difference in mean temperature in this region. This is consistent with the understanding from non-LTE prominence modelling that different spectral lines exhibit varying sensitivities to specific plasma parameters (Labrosse et al., 2010). To obtain parameter maps with more detailed structures, we need to use spectral lines whose intensities have larger correlation coefficients and elasticity coefficients with each parameter. This will be one of our future works.

The maps presented in Figure 4.7 help us to understand the distribution of the parameters that were shown to have the most effect on the calculated Lyman β and Lyman γ intensities. The non-LTE calculations also allow us to study the distribution of other relevant quantities. For example, in the left panel of Figure 4.8, the electron density map shows structures similar to those in the Lyman β and Lyman γ observations. The derived electron densities lie towards the lower end of the values generally reported for prominences. Each map value represents the electron density averaged across the entire slab along the line-of-sight direction shown in Figure 1.8, rather than the local density in the cool prominence core. The average therefore includes the hotter and less dense PCTR layers.

We can also produce intensity maps for other lines. In the right panel of Figure 4.8, we show the computed Hα intensity map, which presents structures very similar to those seen

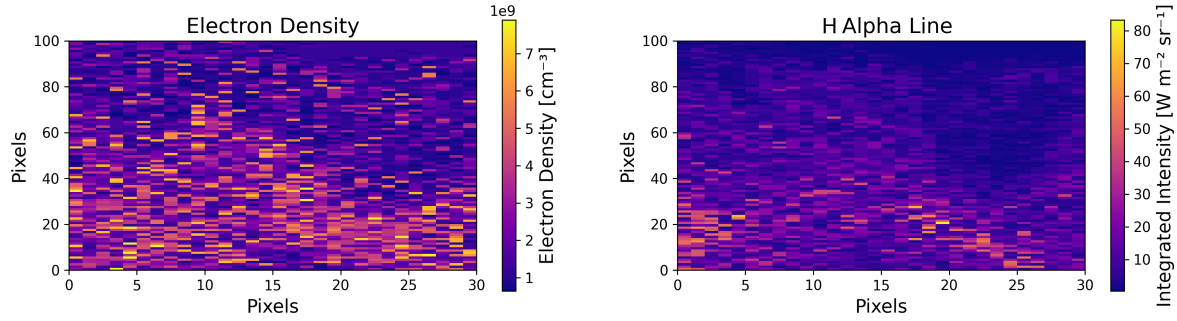

Figure 4.8: The electron density map and Hα intensity map as examples of other maps we can produce (Figure from Zhang et al (2026c, submitted)).

in the Lyman β and Lyman γ line observations. The Hα intensity is sensitive to the amount of cool hydrogen plasma along the line of sight and is therefore related to the column mass distribution. Regions with larger column mass generally contain more emitting material and tend to produce stronger Hα emission. However, this relationship can also be affected by the temperature, pressure, and optical thickness of the plasma. The visibility of Hα intensity map is good compared with other parameter maps, and the structure is quite close to the synthetic Lyman β and Lyman γ intensity maps with the best coefficient set in Figure 4.6. We do not have observational data of Hα line from similar LOS for this event to compare with. The calculated Hα intensities are not large, e.g. compared with another observation in Labrosse et al. (2022); the prominence discussed here would likely appear as a faint prominence. This allows us to generate synthetic maps for various observables (intensity, width) for spectral lines that aren't available in the observation. If a spacecraft has a good angle to observe some phenomena in the Sun but it lacks some spectral lines to do analysis or compare with other observations, this method will be useful.

4.4 Concluding Remarks

In this study, we developed a novel modelling approach to derive the plasma parameters of solar prominences based on SPICE observations from the Solar Orbiter mission. Using the first dedicated off-limb prominence raster obtained on 15 April 2023, we devised a model-constructing tool that combines the diagnostic potential of the Lyman β and Lyman γ lines. By comparing the observed and synthetic intensities through a random-model sampling and refinement process, we achieved a average χ^2 value of approximately 8% between the modelled and observed intensity maps. This relative difference is acceptable in view of the uncertainties inherent to observations (particularly the radiometric calibration) and to the models (e.g. incident radia-

tion). This demonstrates that the proposed method can reliably reproduce the observed radiative properties of the prominence within reasonable computational time.

The parameter maps derived from the best-fit models reveal the spatial distributions of temperature, pressure, column mass, and other key quantities governing the formation of the Lyman lines. Among them, the column mass and pressure structures exhibit strong correspondence with the observed intensity morphology, implying that local variations in mass and gas pressure play dominant roles in shaping the radiative emission pattern of the prominence. The method thus provides a quantitative bridge between spectroscopic diagnostics and plasma modelling, enabling the visualization of internal prominence structures that are otherwise difficult to infer directly from observation.

Chapter 5

Prominence parameters and He II 304 emission

In this chapter, we will introduce the analysis of eruptive prominence plasma parameters' effects on the He II 304 Å Line with Solar Orbiter EUI Observations. We will use EUI/FSI 304 Å and EUVI-A 171/195 Å imaging to characterise the morphology and temporal evolution of this prominence during the eruption, and apply filter-ratio techniques to estimate plasma temperatures. We also use parallel coordinate plots to analyse how plasma parameters affect properties of He II 304 Å line. After that, we will explore how collisional excitation and scattering play roles in the formation of He II 304 Å line.

Most contents of this chapter (i.e. text, tables and figures) come from Zhang et al. (2026d, submitted) and is written or created by me unless otherwise stated. The first, third, and fourth paragraph of Section 5.2 are written by Sargam Mulay. The last paragraph of of Section 5.3.3 is written by Nicolas Labrosse. Sargam Mulay gave me support with the filter-ratio technique to help me find the temperature ranges of this prominence event. I constrained other parameters' ranges and generated 200 random models to explore what affects intensity change of He II 304 Å with altitude and how. I also used the parallel coordinate plot to find the key parameters in the formation of He II 304 Å line. Nicolas Labrosse gave opinions about contents of figures and texts to improve the quality of the paper. He also helped to explain the physical mechanism of large values of the radiative term in this event. Susanna Parenti and Therese A. Kucera also gave comments on an earlier version of this work.

The study by Mierla et al. (2022) on prominence kinematics and radiative properties based on an observation obtained on February 15, 2022, by the Extreme Ultraviolet Imager (EUI; Rochus et al. 2020) on board Solar Orbiter Müller et al. (2020) provides a foundation for focusing on line formation and determining whether the observed He II 304 Å emission primarily originates from resonant scattering or collisional excitation. Mierla et al. (2022) conjecture that the 304 Å line in this eruptive prominence is due to collisional excitation rather than to resonant scattering, but a concrete conclusion is not reached. This is the key question we want to explore in this chapter.

In this study, we analyse the same prominence eruption event. Specifically, we investigated the mechanisms behind the formation of the He II 304 Å line during the eruption and how plasma diagnostics could enhance our understanding of the dynamics involved.

Previous studies have laid the essential groundwork for understanding the formation of the He II 304 Å line in solar prominences. Labrosse and Gouttebroze (2001) presented non-local thermodynamic equilibrium (non-LTE) modelling of the Helium spectrum in isothermal isobaric static prominences, demonstrating how line intensities are influenced by variations in temperature, pressure, and microturbulence. This was then extended in Labrosse and Gouttebroze (2004) to show how the introduction of a prominence-to-corona transition region impacts the energy level populations within the helium atom via the coupling between statistical equilibrium and radiative transfer equations. Labrosse et al. (2007) advanced this work by examining the Doppler dimming effect in moving prominences, highlighting how radial mass motion influences the He II 304 Å line. Gouttebroze and Labrosse (2009) extended these models with a cylindrical-thread approach, incorporating two-dimensional structural variations that provide a refined understanding of intensity distributions within prominences.

Wang et al. (1998) provided early observational evidence of prominences exhibiting distinct morphological differences in Hα and He II 304 Å, challenging the assumption that these lines trace similar structures. Schiralli (2014) has revealed important differences between Hα and He II 304 Å observations, showing that while Hα provides detail in cooler prominence cores, 304 Å line emission better captures the structure, including hotter transition regions. However, the lower spatial resolution of the 304 Å observations limits direct comparisons of the fine structures seen in the two lines. Labrosse et al. (2011) further examined He II 256.32 Å with Hinode/EIS data, confirming its formation predominantly via resonant scattering in the prominence-to-corona transition region (PCTR). Labrosse and McGlinchey (2012) applied diagnostics of Doppler effects to prominence eruptions observed at 304 Å, confirming that Doppler shifts provide critical information on prominence plasma conditions during eruptions. Labrosse and Rodger (2016) introduced multi-thread models that simulate the complex interactions within prominence fine structures, demonstrating how the multi-thread structure affects the helium line shape and intensities, and temperature gradients strongly impact the Helium spectrum. Together, these studies offer a framework for interpreting He II line formation.

5.1 Observations

A prominence eruption was observed in the He II 304 Å passband by EUI/FSI telescope aboard Solar Orbiter on February 15-16, 2022. This is the first observed eruption in the He II 304 Å emission that is above 6 $R_\odot$ (Mierla et al., 2022). We also have EUVI-A observation in 171 Å, 195 Å and 284 Å channels.

We used images from the EUVI-A 171 and 195 Å channels to study the prominence eruption

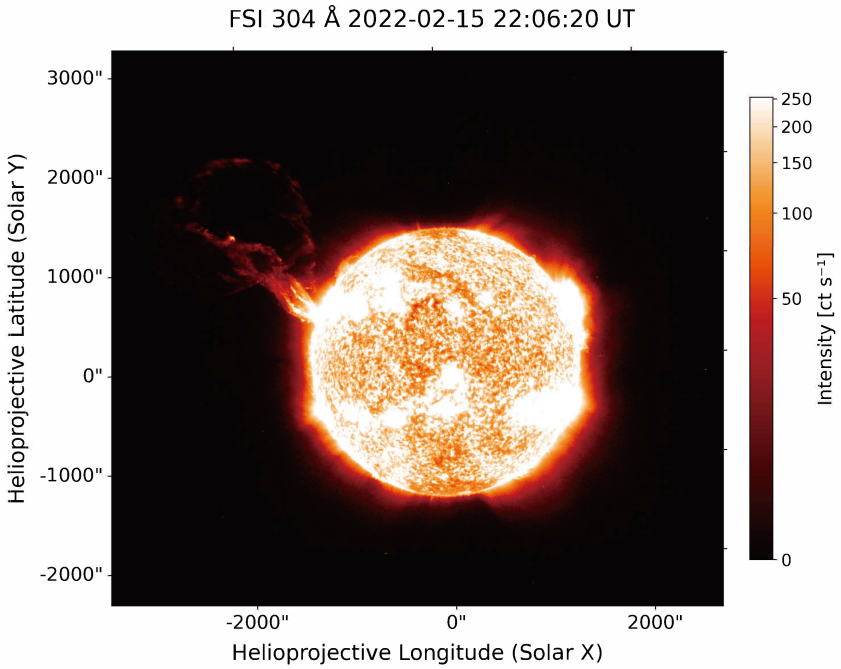

Figure 5.1: The full disc image of the Sun with the prominence eruption observed on February 15, 2022, using EUI/FSI 304 Åchannel (Figure from Zhang et al. (2026d, submitted)).

that occurred on February 15, 2022. The EUVI level 0.5 data were downloaded and converted to level 1 using the solarsoft (SSW; Freeland and Handy 1998) routine[1] `sechhi_prep.pro`. We obtained the EUVI images with the intensity units of DN and normalised them using the exposure time (units = DN/s/pix). These images were used further for temperature diagnostics using the filter ratio method (see section 5.2).

Figure 5.1 shows a full disc image of the Sun along with a prominence eruption observed in the 304 Å channel of EUI/FSI on February 15, 2022. We adjusted the intensity scale in this image to reveal the faint EUV emission from the prominence eruption. This adjustment made the disc emission appear brighter.

EUI observes the sun in multiple channels. Of particular interest to this project is the 304 Å channel. The 304 Å channel is sensitive to cooler plasma in the transition region between the solar chromosphere and corona, with emission lines originating from singly-ionised helium (He II). The 304 Å line has demonstrated high sensitivity to the radial movement of the solar prominence. This is due to its formation primarily occurring through the scattering of incident radiation from the Sun (Labrosse and McGlinchey, 2012). It provides information on the dynamics of

[1] `https://stereo-ssc.nascom.nasa.gov/publications/CMAD/secchi/STEREO\_SECCHI\_Prep\_CMAD\_20211206.pdf`

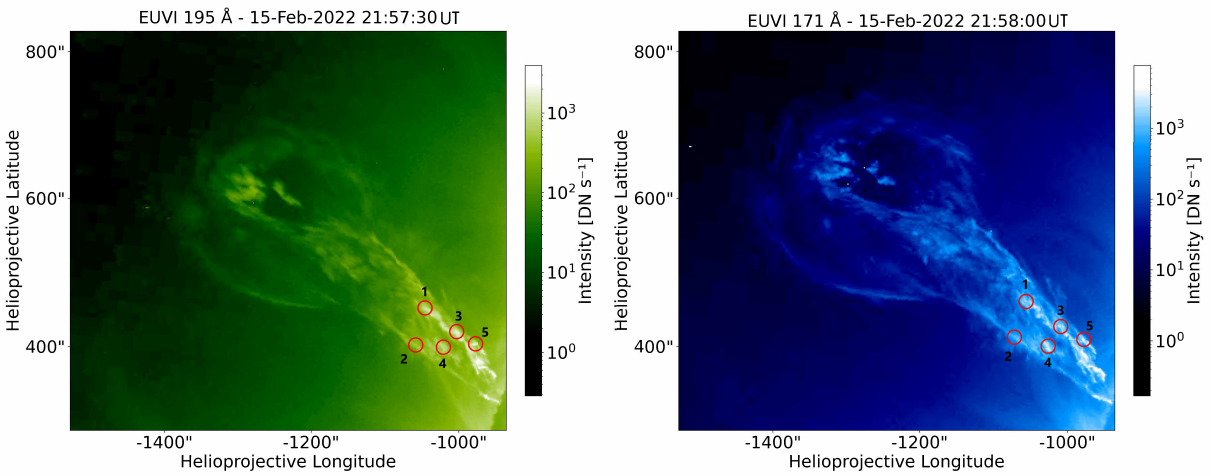

Figure 5.2: The prominence observed by EUVI-A in the 171 Å and 195 Å channels. The five red circles are the five features we tracked (Figure from Zhang et al. (2026d, submitted)).

prominences, filaments, and other features on the solar disc (Mierla et al., 2022). Such observations help us better understand the mechanisms responsible for heating the corona, accelerating the solar wind, and driving space weather phenomena.

5.2 Filter-ratio analysis

Plasma diagnostic techniques, such as the filter-ratio method (Del Zanna et al., 2011; Mulay et al., 2017), have been used to study plasma temperature during various dynamic events in the solar atmosphere. Particularly, broadband filters from the Atmospheric Imaging Assembly (AIA; Lemen et al. 2012) instrument onboard Solar Dynamics Observatory (SDO) and X-ray Telescope (XRT; Golub et al. 2007) onboard Hinode satellite (Kosugi et al., 2007) have been extensively exploited. This method involves studying emitted radiation using two broadband filters from the spacecraft and comparing the intensity ratios recorded at each pixel with the corresponding ratios of the temperature response function of those filters.

For the February 15, 2022, prominence eruption event, the field of view of AIA is relatively small. It is not possible to track the prominence eruption up to a high altitude (6 $R_{\odot}$). Moreover, the prominence is behind the limb from the viewpoint of AIA, and we could not use these images to study the temperature using the filter ratio technique. Instead, we focused on near simultaneous images from the 171 Å and 195 Å channels of STEREO EUVI-A, where the prominence eruption was nicely captured. The images are shown in Fig. 5.2. We studied the evolution of the prominence at various heights and used the observed intensity (in units of DN/s/pix) recorded in these filters to analyse the temperature of the erupting prominence. We make several assumptions when applying the filter-ratio analysis to the EUVI-A 171 Å and 195 Å channels. First,

we assume that the plasma is optically thin in the range of wavelengths used in this analysis, so that the emission from the plasma at a given wavelength should not be significantly absorbed or scattered by the plasma itself, allowing the observed intensity to be directly related to the amount of emitting material along the line of sight. This assumption aligns with the typical characteristics of PCTR regions. Second, to simplify the analysis, we assume an isothermal temperature distribution for prominence structures along the line of sight. Third, we assume a constant temperature over time within each feature during the brief observation period (21:57:30 $\sim$ 21:58:00 UT) because of the small differences in the observation times between the 171 Å and 195 Å channels. This is reasonable since temperature variations are generally small over short timescales. Finally, we acknowledge minor alignment variances due to manual tracking, though careful frame-by-frame adjustments mitigate this risk. There are several assumptions for using this analysis, which may be strong. But it is the only way we can do to constrain the temperature range for this prominence event.

The temperature response function (in DN s^{-1} pix^{-1} cm^5 units) for the 171 Å and 195 Å channels of EUVI-A are calculated using the CHIANTI atomic database version 11.0.2 (Dufresne et al., 2024), electron number density, N_e of 1×10^{10} cm^{-3}, and coronal abundances. We used the effective area[2] for these filters from SSW. We followed a similar procedure (see Appendix of Del Zanna et al. 2011) used to calculate temperature responses for the AIA filters to calculate those for the STEREO EUVI filters. Figure 5.3 (left panel) shows the temperature response function for the 171 Å, 195 Å and 284 Å channels, and the ratio of the temperature responses for the 195/171 filters is shown in the right panel.

The temperature responses of these three filters show multiple peaks across a wide temperature range, indicating their multithermal nature. The ratio of the responses is not a single-valued function (like XRT filter ratio - see Fig. A3 in Mulay et al. 2017), so we carefully considered the limitations in interpreting the temperature information from this filter ratio analysis.

The peaks in the filter temperature responses indicate that the photons in the EUVI 171 Å and 195 Å channels are emitted mostly from the PCTR region and by the surrounding coronal plasma, which should be optically thin. These filters are suitable for the filter-ratio analysis of the erupting prominence region. We chose five features along the prominence, shown with red circles in Fig. 5.2. We manually identified and tracked these features from 22:00 to 22:10 UT. The features were identified in consecutive images from spatial continuity, direction of motion, and similarity in morphology relative to the surrounding prominence structure. We also assumed that the temperatures of the features we track are constant across the domain and over time to apply the filter-ratio method.

To find the actual variation in intensity, we used images recorded at 21:00 UT before the eruption and subtracted the background intensity from each pixel in the images taken during the

[2] https://stereo-ssc.nascom.nasa.gov/publications/CMAD/secchi/STEREO_SECCHI_EUVI_CMAD_20211206.pdf

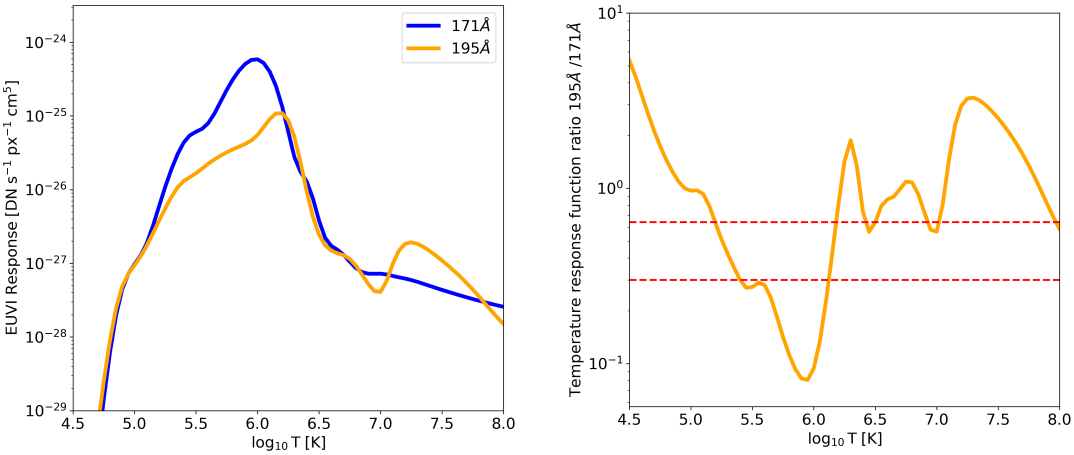

Figure 5.3: Left panel: The STEREO EUVI-A temperature response functions for the 171 Å, 195 Å and 284 Å channels. They are calculated using the effective area from SSW and the CHIANTI atomic database version 11.0.2. Right panel: The ratio of temperature response functions for the EUVI 195 Å and 171 Å channels. The two red dashed lines are the minimum and maximum ratios in Table 5.1 (Figure from Zhang et al. (2026d, submitted)).

Table 5.1: The observed intensity ratios of 195 Å/171 Å filters for five features along the eruptive prominence.

Feature	Intensity of 171 Å DN/s		Intensity of 195 Å DN/s		195/171 Å intensity ratio	log temperature [K] (MK)
	before BS	after BS	before BS	after BS	after BS	
1	1650	1493	1098	961	0.64	5.20 (0.16), 6.18 (1.51), 6.43 (2.67), 6.50 (3.15), 6.93 (8.53), 7.02 (10.35), 7.97 (93.75)
2	904	736	517	348	0.47	5.27 (0.19), 6.16 (1.43)
3	3024	2817	1755	1532	0.54	5.24 (0.17), 6.17 (1.47)
4	2462	2215	896	661	0.30	5.40 (0.25), 6.12 (1.31)
5	3297	2980	1730	1340	0.45	5.29 (0.19), 6.15 (1.43)

Notes - Intensity values are given before and after background subtraction (BS). We choose intensity values at the center of circles in Figure 5.2. The features 1-5 are labelled in decreasing order of distance from the limb.

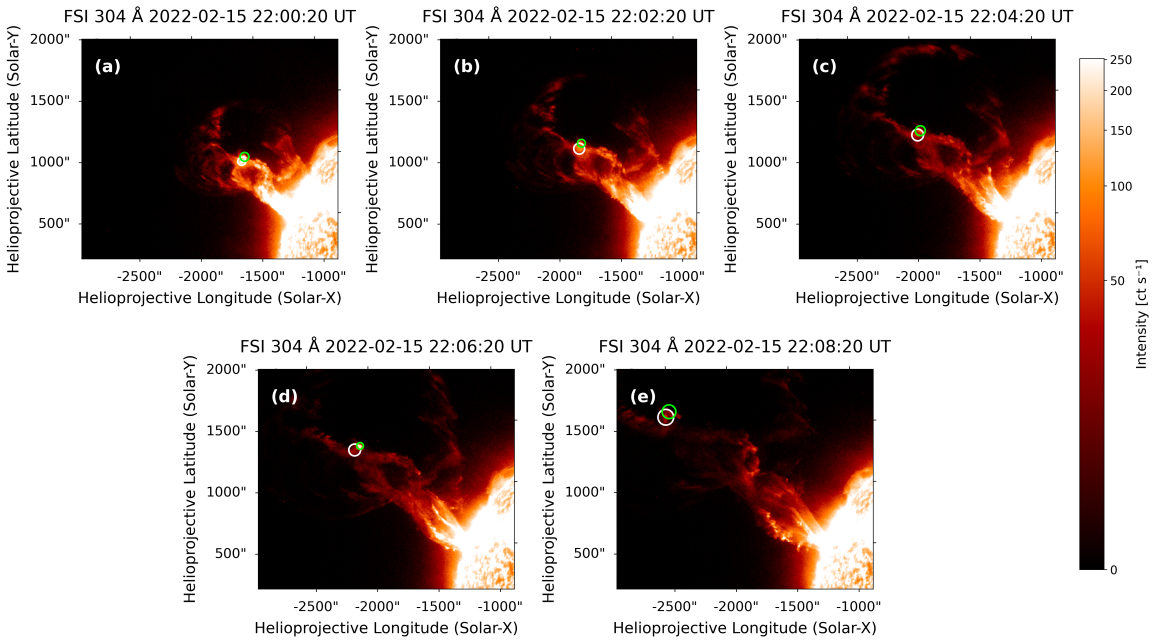

Figure 5.4: Evolution of the prominence eruption as seen by FSI at 304 Å showing the two features being tracked (Figure from Zhang et al. (2026d, submitted)).

prominence eruption: $I = I_{\text{eruption}} - I_{\text{background}}$. Table 5.1 summarises the intensity recorded for two filters before and after subtracting the background. The calibrated EUVI-A data used in this analysis do not provide formal intensity uncertainties. Moreover, the emission of these two lines from these two lines is also not negligible. We are therefore unable to determine the uncertainty ranges of the intensities of 171 Å and 195 Å lines. The background-subtracted ratios should consequently be regarded as approximate estimates.

We obtained the minimum (maximum) intensity ratio of 0.30 (0.64) for five features. We plotted these minimum and maximum intensity ratio values as red dashed lines in Fig. 5.3 to narrow down the range of ratio and temperature values (log T [K] = 5.20~5.40 (0.16~0.25 MK), and 6.12~6.18 (1.31~1.51 MK) and a few more values in the higher temperature range) we should consider. The temperature range of log T [K] = 5.20~5.40 (0.16~0.25 MK) is more appropriate for the features along the eruptive prominence we are studying in this chapter.

5.3 Results

5.3.1 Intensity change of 304 Å line with altitude

We have explored how a feature's intensity varies with altitude during the eruption process in this event. We have tracked two bright regions (indicated by grey and green circles in Fig. 5.4) in FSI 304 Å passband. These features were identified as localised intensity enhancements that

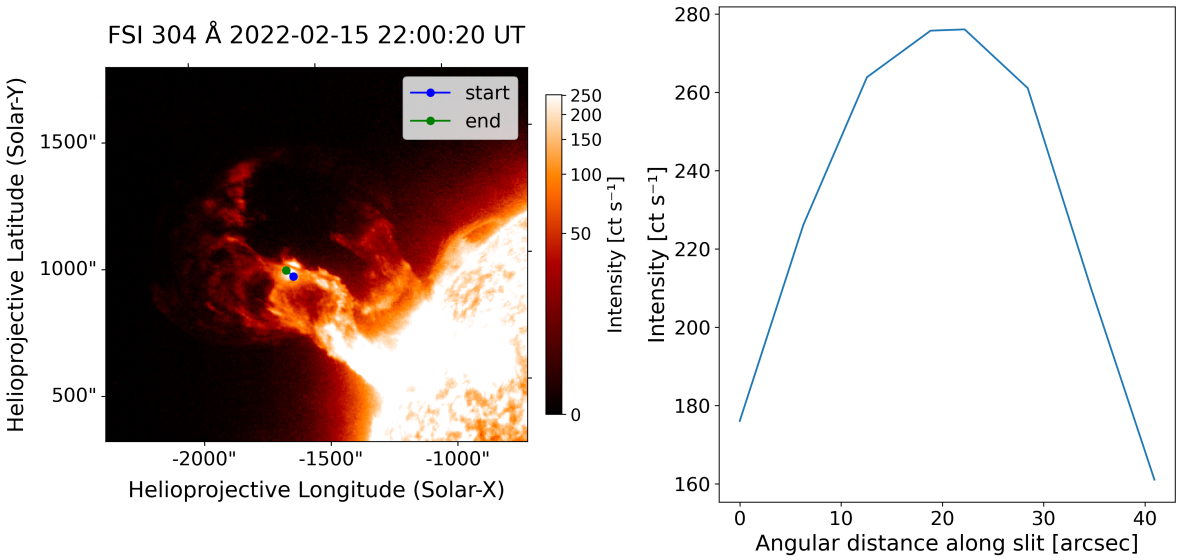

Figure 5.5: An example of the tracked feature in FSI 304 Å at 22:00 UT, Feb 15th, 2022. The right image is the intensity profile along the cut in the left image (Figure from Zhang et al. (2026d, submitted)).

could be followed between consecutive images based on their spatial continuity, direction of apparent motion, and broadly similar morphology. However, they should not be interpreted as uniquely identifiable plasma motions. The observed displacement may represent plasma motions, or the evolution of the magnetic structures, and the available observations do not allow these possibilities to be distinguished. The cadence of the FSI data in the 304 Å passband was around 2 minutes. The 304 Å passband of EUVI has a cadence of around 3 minutes. Therefore, we use FSI data to track features. The radius of the circles is proportional to the size of the visual edges of the features: if the circle becomes smaller, the feature becomes more concentrated in plasma density; if the circle becomes larger, the feature becomes more dispersed. After tracking the two features, we trace a diagonal cut through the bright region and obtain an intensity profile along that cut. Figure 5.5 shows an example of the tracked feature in FSI 304 Å passband at 22:00 UT, February 15, 2022. The left panel shows the start and the end of a diagonal cut of a feature; the right panel shows the intensity profile along the cut from the start to the end. To reduce the uncertainty in the diagonal cut of the features, we calculate the mean intensity along the diagonal line after removing 15% of the data on the left side of the intensity profile and 15% from the right side. The 15% threshold was selected empirically through inspection of the intensity profiles.

In Fig. 5.6, we can see that the intensity of the two features decreases quickly until they reach an altitude of 2.4 R_s. Above that, Feature 1 changes slowly, whereas the intensity of Feature 2 suddenly increases at around 2.4 R_s and reaches the peak at 2.6 R_s. The randomly generated models shown in Figure 5.6 are not intended to reproduce the observed intensity

evolution of either feature. Instead, they are used to identify systematic dependencies of the He II 304 Å intensity on column mass and Γ. The figure also shows that no clear dependence of the calculated intensity on altitude is found over the studied range. Therefore, the observed intensity changes cannot be explained by altitude. By contrast, the model intensity shows clearer correlations with column mass and Γ.

The high intensity value occurs at 22:06:20 UT in Fig. 5.4. We can see that the circle for Feature 2 is quite small compared with other panels, which means Feature 2 is more concentrated at this time. This change may be related to a temporary variation in the density or line-of-sight distribution of the emitting plasma. Plasma motions could redistribute material within the feature, while an MHD wave could, in principle, modify the local density and emissivity without producing substantial net mass transport. However, no clear periodic or propagating signature is identified in the available observations, and therefore the underlying mechanism cannot be determined from the intensity and morphological changes alone.

There could also be material changes inside and outside the circles. These material changes would affect the intensity we observe in Fig. 5.6. When some material moves into the circle, the intensity increase; when some material moves out of the circle, the intensity decreases. Although material motions across the circular boundaries cannot be excluded, the positions, projected areas, and overall morphologies of the two features remain broadly similar during the analysed period. This suggests that large scale material motions across the boundaries are unlikely to be the dominant cause of the observed intensity variations, although they may still contribute to them.

We generate 200 random PCTR models to compare with the observation, as shown in Table 5.2. The purpose of these models is not to sample all possible combinations of the multidimensional parameter space exhaustively. Instead, the parallel coordinate plots are used to examine the qualitative relationship between each individual input parameter, represented by a separate axis, and the selected line property represented by the colour scale. They are not used to infer the full relationships among all input parameters. As discussed previously, tests with 1000 randomly generated models produced the same trends as the 200 models sample, while mainly increasing the density of lines in the plots. We therefore adopted 200 models as a compromise between identifying these qualitative trends and computational cost. The choice of the altitude depends on data, in the range $2 \sim 3.5\ R_S$. In section 5.2, we refined the temperature range as $\log_{10}(T)\,[K]$ = 5.20~5.40 (0.16~0.25 MK) using the filter ratio technique. We constrained the temperature range using observations of the 171 Å and 195 Å lines, which are emitted primarily from a thin PCTR region. Therefore, we adopt this range as the surface temperature range. Our derived temperature range is roughly consistent with the findings of Parenti et al. (2012), who showed that the 171 Å band in prominences is dominated by Fe IX emission from plasma at temperatures $> 4 \times 10^5$ K ($\log_{10}(T)\,[K] > 5.6$), and that such emission arises from the PCTR.

We obtain the range of radial velocity by tracking several features, and we identify the

Table 5.2: The parameter ranges for different variables.

Parameter	Range
Central Temperature	8000 K $\sim$ 15000 K
Surface Temperature	158500 K $\sim$ 251000 K
Central Pressure	0.001 dyn cm^{-2} $\sim$ 1.0 dyn cm^{-2}
Surface Pressure	0.001 dyn cm^{-2} $\sim$ 0.1 dyn cm^{-2}
Column Mass	1.0×10^{-7} g cm^{-2} $\sim$ 1.0×10^{-5} g cm^{-2}
Γ	2 $\sim$ 10
Altitude	1392680 km $\sim$ 2437190 km
Radial Velocity	500 km s^{-1} $\sim$ 2500 km s^{-1}
Microturbulent Velocity	5 km s^{-1}

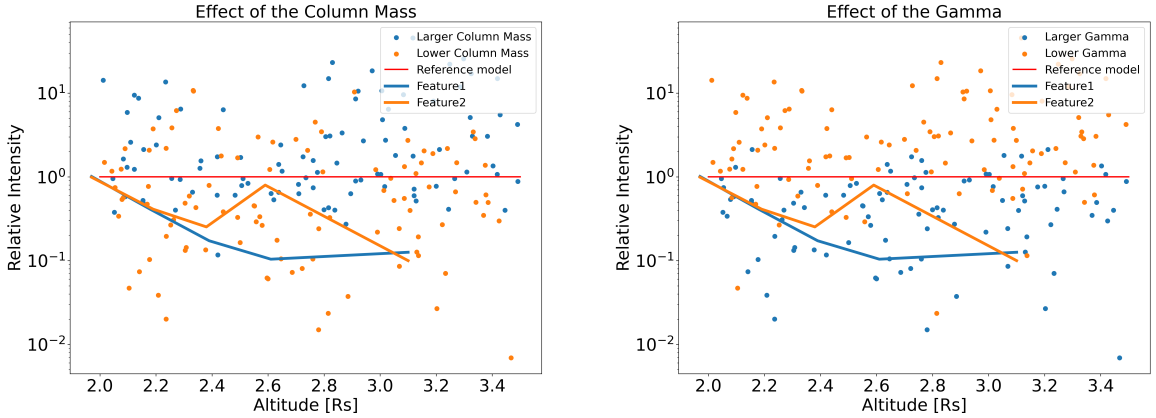

Figure 5.6: The change in the relative intensity for features 1 and 2 with altitude. The points correspond to 200 random models. The orange and blue lines show intensity variation with altitude for the two features tracked over time by the observation. The relative intensity of the two features is normalised by their intensity at $R_S = 1.97$. The red lines are connected by reference models that have fixed values of parameters except altitude. The values of parameters have been set as the median of their ranges. The relative intensity of random models and reference models is normalised by the reference model at $R_S = 2$ (Figure from Zhang et al. (2026d, submitted)).

range of altitude from the image. The range of radial velocity we obtained is 1180 km s^{-1} $\sim$ 2200 km s^{-1}, which is similar to Mierla et al. (2022). The uncertainty of the result is about 120 km s^{-1}, which comes from the uncertainty of the location of features. The range of altitude we obtained is 2.0 R_S $\sim$ 3.5 R_S. For other parameters, we choose the usual ranges that are expected in a prominence event from Labrosse and McGlinchey (2012).

In Fig. 5.6, we study the change in relative intensity with altitude. To better compare with observations, we define a series of reference models and use relative intensity to track the trend of intensity changes through altitude. The reference models have values of parameters that are set to the median of their ranges, except for the altitude, as shown in Table 5.3. The reference models of different altitudes are connected as a red line in Figure 5.6.

We can see that the relative intensity nearly has no change with altitude for reference models that have fixed values of parameters except altitude (the red line). Therefore, the change in in-

Table 5.3: The reference model parameters.

Parameter	Value
Central Temperature	11500 K
Surface Temperature	204750 K
Central Pressure	0.50 dyn cm^{-2}
Surface Pressure	0.05 dyn cm^{-2}
Column Mass	5.05×10^{-6} g cm^{-2}
Γ	6
Radial Velocity	1500 km s^{-1}
Microturbulent Velocity	5 km s^{-1}

tensity with altitude in the observations is likely to be caused by the change in other parameters. The geometrical dilution of the incident solar radiation is included in the calculations, so the illumination from the solar disc and transition region should decrease with increasing altitude. However, at the high radial velocity adopted for the reference models, direct resonant scattering of the incident He II 304 Å radiation is already strongly reduced by Doppler dimming. The additional effect of geometrical dilution over the considered altitude range therefore produces only a negligible change in the emergent intensity.

In Fig. 5.6, among the brighter models, 64 % of them have larger column mass, 85 % of them have lower gamma; among the dimmer models, 63 % of them have lower column mass, 78 % of them have larger gamma. This suggests that column mass and gamma play important roles in the change of intensity with altitude, which could explain the intensity changes of the two features (orange and blue lines) in Fig. 5.6.

5.3.2 Analysis of parameters' effect by parallel coordinate plots

We use the method of the parallel coordinate plot to analyse the prominence plasma parameters' effects on quantities related to the formation of the 304 Å line. A parallel coordinate plot is a method for visualising relationships in multivariate data. Parallel coordinate plots have proven effective for understanding complex spatiotemporal datasets, particularly when spatial, temporal, and attribute-based relationships are crucial (Edsall, 2003). With this method, we can see a parameter's effect more easily without setting other parameters into a specific range. We can also simultaneously display and compare values and relationships of multiple variables.

This approach has been successfully applied in our previous studies to investigate the formation of the hydrogen Lyman lines in solar prominences. In chapter 3 (Zhang et al., 2026b), we used parallel coordinate plots to analyse the effects of different parameters of Lyman β and Lyman γ lines, such as temperature, pressure, column mass, and slab thickness. This provided a framework to interpret the SPICE observations presented in chapter 2 (Zhang et al., 2026a). Those studies demonstrated that the method is particularly useful for identifying dominant parameters and exploring relations among them. Building on this earlier work, we apply the same

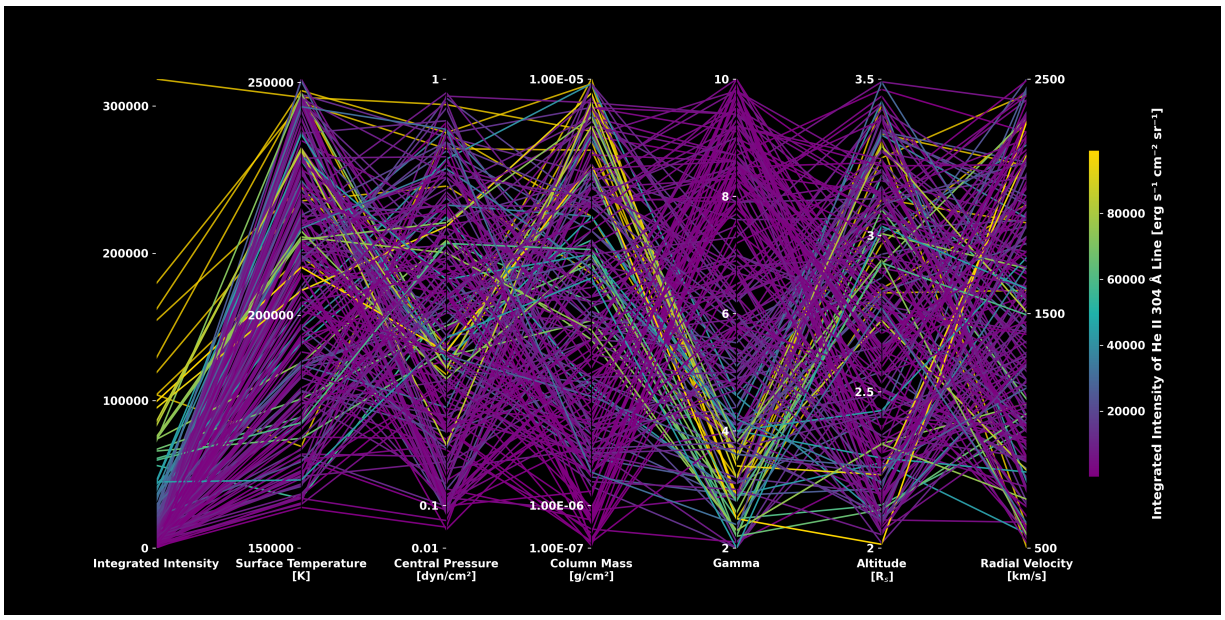

Figure 5.7: The parallel coordinate plot of 6 parameters with the integrated intensity of 304 Å line (Figure from Zhang et al. (2026d, submitted)).

methodology to the He II 304 Å line, exploring helium-line formation processes in prominence plasmas.

To analyse the FSI observations of this event, we ran 200 random PCTR models. The event has observational constraints for surface temperature (from filter-ratio analysis), altitude, and radial velocity.

In a parallel coordinate plot like Fig. 5.7, if we see a diversity of colours on different value ranges when we focus on one parameter's axis, this means the parameter does not have much effect; on the other hand, if we see a certain colour concentrating on a certain value range, this means the parameter has some effect. The effect is more significant when the the range of values over which a certain colour concentrates is narrow. It is also possible to use correlation coefficients to quantify these relationships. We have noted more obvious effects on a parallel coordinate plot when the corresponding correlation coefficient is larger than 0.3. Hence, when a correlation coefficient between, e.g., one of the plasma parameters and one characteristic of the 304 Å line is larger than 0.3, we will consider that parameter as an important parameter in this case.

We explore what parameters are important for the integrated intensity and the optical thickness of the 304 Å line. In Fig. 5.7, we can see that the most important parameters of the integrated intensity of the 304 Å line are column mass and gamma, which have correlation coefficients with the integrated intensity of 0.36 and -0.51, respectively. In Fig. 5.8, we can see that the most important parameter of the optical thickness of the 304 Å line is column mass, which has a correlation coefficient with optical thickness of 0.75. Correlation coefficients of key parameters for the He II 304 Å line are listed in Table 5.4.

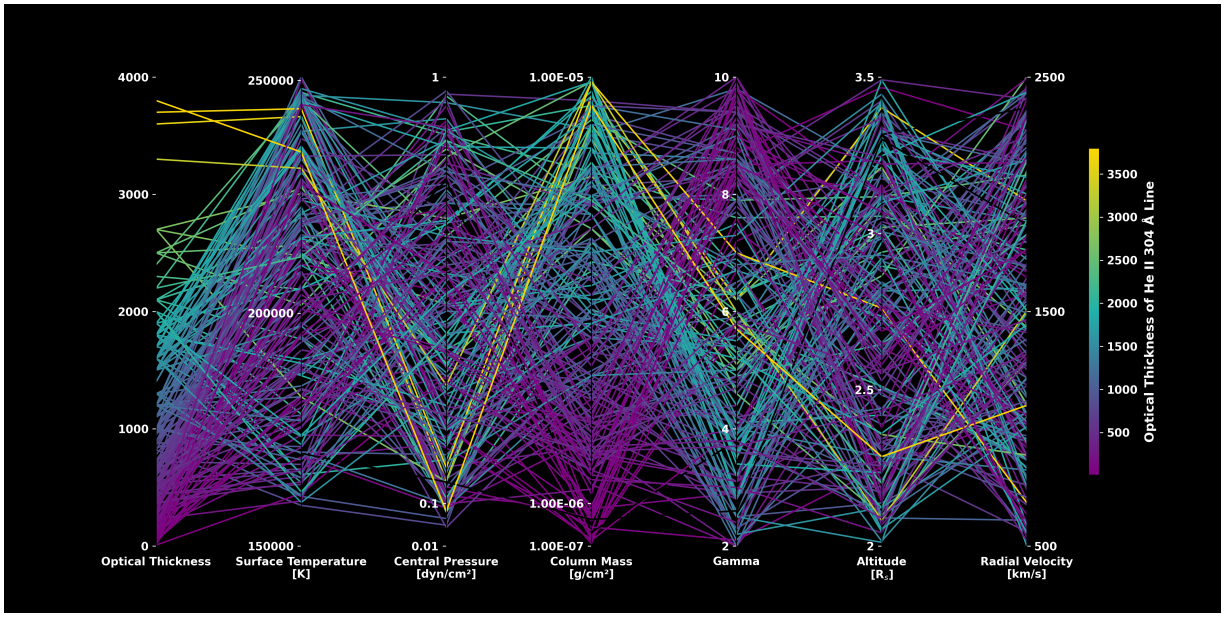

Figure 5.8: The parallel coordinate plot of 6 parameters with the optical thickness of 304 Å line (Figure from Zhang et al. (2026d, submitted)).

Table 5.4: Correlation coefficients for He II 304 Å line properties

Property	Key Parameters	Correlation Coefficient
Integrated Intensity	Column mass	0.36
	Gamma	-0.51
Collisional term	Central pressure	0.45
	Column mass	0.31
	Gamma	-0.56
Radiative term	Column mass	0.36
	Gamma	-0.55
Optical Thickness	Column mass	0.75

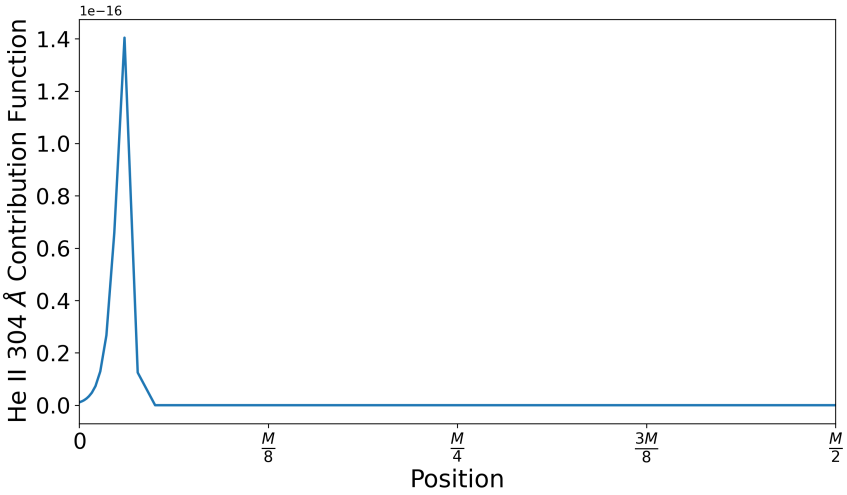

Figure 5.9: An example of the contribution function of 304 Å line along the slab.

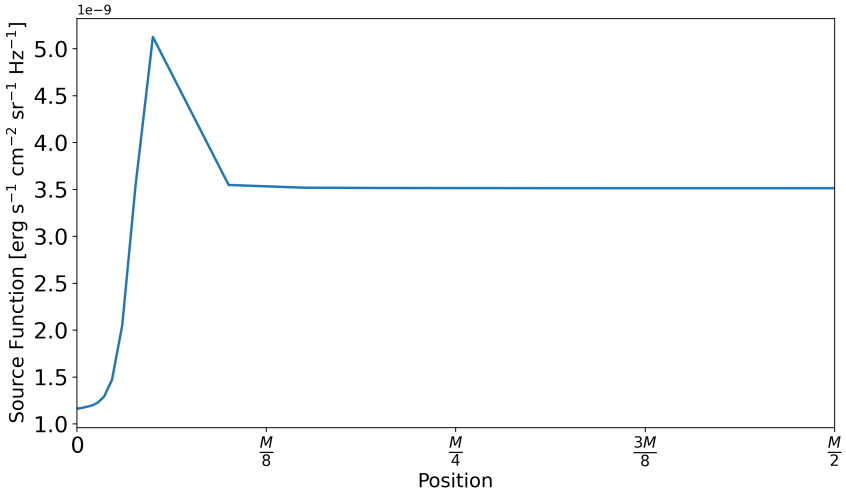

Figure 5.10: An example of the source function of 304 Å line along the slab.

To study how collisional excitation and radiative processes contribute to the He II 304 Å line formation, we generate Figs. 5.11 and 5.12 to study the contributions of the collisional term and radiative term of the 304 Å line. We use the collisional term and radiative term from the source function given by equation 3.1 (Labrosse et al., 2006). We consider the values of the collisional and radiative terms taken at the position where the contribution function of the He II 304 Å line peaks. An example of the shape of the contribution function of 304 Å line along the slab is showed in Figure 5.9. An example of the shape of the source function of 304 Å line along the slab is also showed in Figure 5.10.

In Fig. 5.11, we can see that none of the six parameters considered in this study has a significant effect on the collisional term. All 200 random models lead to collisional terms that are lower than $4.0 \times 10^{-10}\,\mathrm{erg\,s^{-1}\,cm^{-2}\,sr^{-1}\,Hz^{-1}}$. Figure 5.11 shows that the most important parameters to determine the collisional term in the formation of the 304 Å line are central pres-

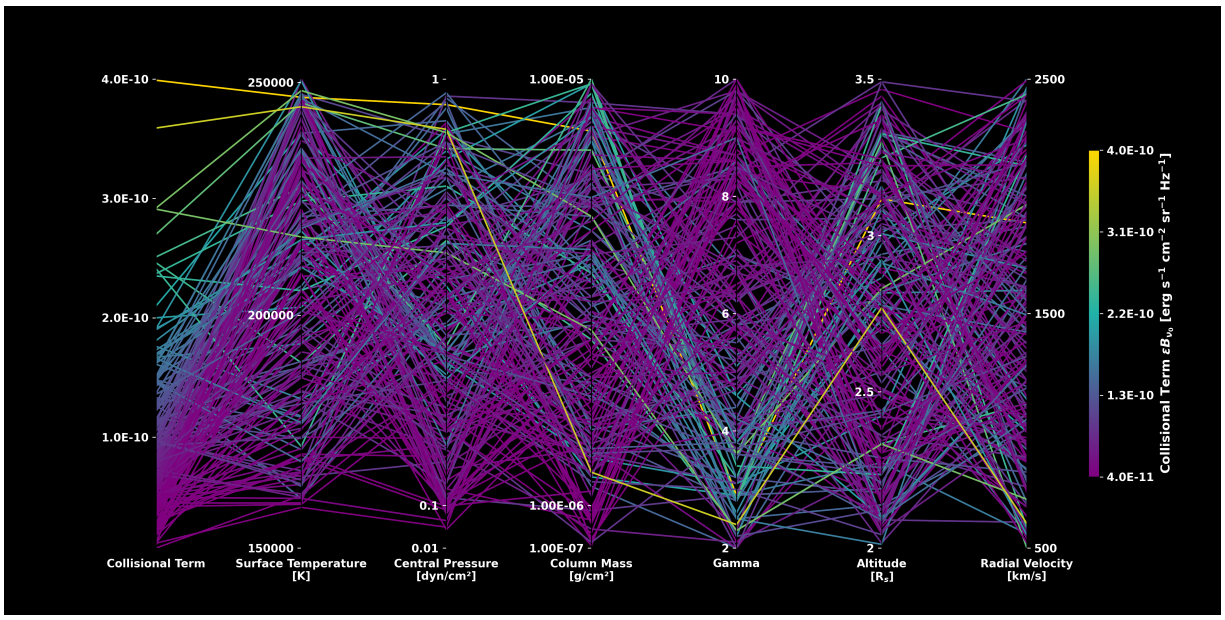

Figure 5.11: The parallel coordinate plot of 6 parameters with the collisional term of 304 Å line (Figure from Zhang et al. (2026d, submitted)).

sure, column mass and gamma, which have correlation coefficients (between parameters and the collisional term) of 0.45, 0.31 and -0.56. Figure 5.12 shows that the most important parameters to determine the radiative term in the formation of the 304 Å line are column mass and gamma, which have correlation coefficients (between parameters and the radiative term) of 0.36 and -0.55. Among the 200 random models, most of them have radiative terms from $1.0 \times 10^{-10}\,\mathrm{erg\,s^{-1}\,cm^{-2}\,sr^{-1}\,Hz^{-1}}$ to $3.0 \times 10^{-8}\,\mathrm{erg\,s^{-1}\,cm^{-2}\,sr^{-1}\,Hz^{-1}}$. This result shows that the radiative term is dominant in the formation of the He II 304 Å line for the range of model parameters considered here.

5.3.3 Discussion

Effect of model parameters on the He II 304 Å line

We have analysed the most important parameters or the February 15, 2022, event in relation to the formation of the He II 304 Å line. To summarise, we found that the integrated intensity of the He II 304 Å line is mainly determined by the column mass and by gamma (corresponding to the temperature gradient in the PCTR). The optical thickness of the line is mostly affected by the column mass. The radiative term in the source function is mostly affected by column mass and gamma. The collisional term in the source function is mostly affected by central pressure, column mass and gamma.

The column mass affects the integrated intensity, the radiative term and the optical thickness. The column mass affects radiation rates, which enter the radiative term of the expression of the source function (Eq. 3.1). $\bar{J}$ is the mean intensity of the radiation field. When we vary the

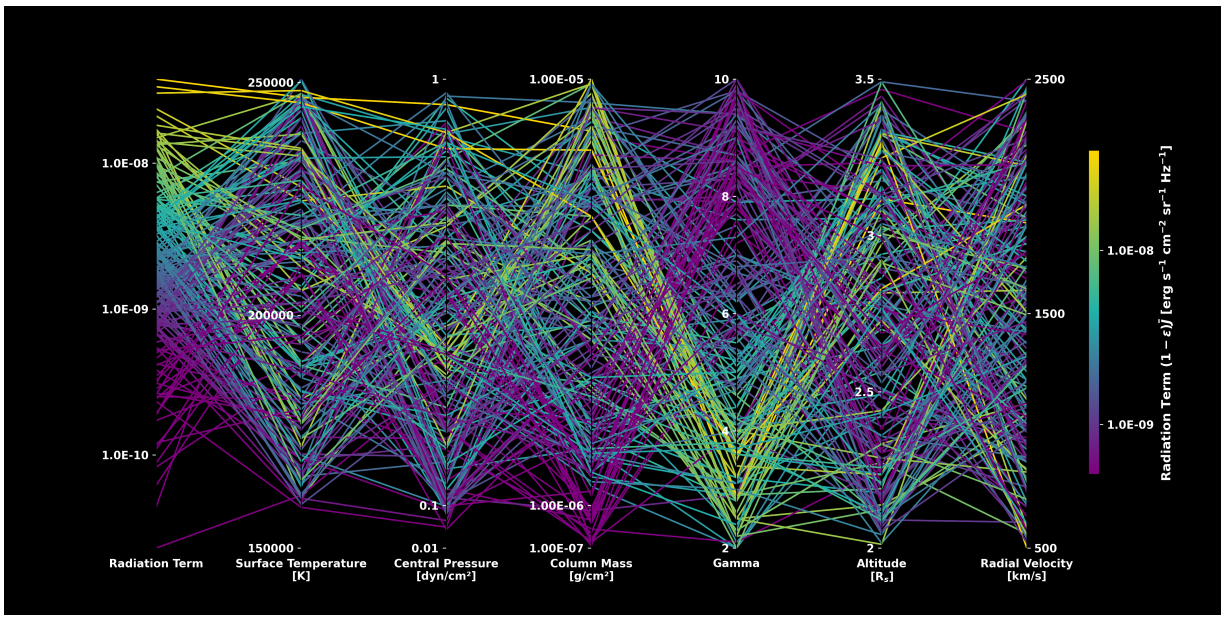

Figure 5.12: The parallel coordinate plot of 6 parameters with the radiative term of 304 Å line (Figure from Zhang et al. (2026d, submitted)).

column mass while keeping the other parameters fixed, the density of particles does not change much. Thus, the total intensity of the radiation field positively correlated with column mass. Through the source function, the column mass can indirectly affect the integrated intensity.

The value of gamma (which corresponds to the steepness and extent of the PCTR) affects both the integrated intensity and the radiative term. When gamma is high, it means that the temperature changes more quickly in the PCTR, which means the high temperature part of the prominence is less extended. Conversely, a smaller gamma produces a more extended PCTR, so that a larger amount of plasma lies within the temperature range in which the He II 304 Å line is efficiently formed. This directly impacts the integrated intensity. The temperature structure affects the amount of plasma that efficiently participates in radiative processes. Therefore, gamma also affects the radiative term.

The pressure affects the density of helium ions and electrons, and therefore affects the collisional term.

The surface temperature, altitude and radial velocity have no significant effects compared with other parameters in the parameters' ranges we have refined.

In this study, we have assumed that the observed emission in the 304 Å passband is entirely due to He II. However, Si XI at 303.32 Å which forms at $\sim$ 1.5 MK, as well as other ions such as O V, Ca XVIII and Fe XVIII also contribute to the observed 304 Å line. In off-limb observations, the emission of those lines can be comparable to the He II 304 Å signal, especially over the diffuse hot corona (Antolin et al., 2024). Antolin et al. (2024) presented several methods to separate the cool and hot components within the AIA 304 Å passband, showing that the hot contribution can be significant and that its removal improves the contrast of cool structures such

as coronal rain and prominences.

Although our present analysis does not explicitly correct for this hot contamination, its presence could affect the absolute intensity levels we derive. We acknowledge that this is an important limitation, because the hot contribution may itself vary with altitude and may also be modified by absorption by the prominence plasma. We examined the possibility of applying an AIA based decomposition. However, in the AIA view, the erupting prominence is substantially affected by line-of-sight overlap with unrelated foreground structures. It is therefore not possible to obtain a reliable estimate of the hot 304 Å component associated specifically with the erupting prominence from these observations.

Consequently, the analysis of the relative variation of the 304 Å intensity with altitude should be interpreted with this limitation in mind. Nevertheless, the parallel coordinate plots independently show the same dependence of He II 304 Å intensity on column mass and the steepness of the temperature gradient. The consistency between the two analyses provides independent support for the robustness of these qualitative conclusions.

However, future analysis of 304 Å line study could benefit from applying similar decomposition techniques to isolate the pure He II 304 Å component, especially when studying off-limb eruptive prominences.

Formation of the He II 304 Å line

Our findings can be compared with the earlier work of Labrosse and McGlinchey (2012), who investigated the formation of the He II 304 Å line in eruptive prominences using SDO/AIA observations and non-LTE radiative transfer modelling. Labrosse and McGlinchey (2012) demonstrated that the computed intensity of the 304 Å line may either decrease or increase with radial velocity depending on the local plasma conditions, particularly the column mass and temperature of the prominence plasma. They highlighted that an increase in column mass during an eruption could counteract the Doppler dimming effect and even lead to an overall brightening of the line with velocity.

In the present study, we extend this analysis by systematically exploring the effects on the parameters using a set of 200 random PCTR models and parallel coordinate plots to visualise multivariate relationships. We confirm that column mass plays a critical role in determining the integrated intensity, the collsional term, the radiative term, and the optical thickness of the He II 304 Å line. Furthermore, we identify additional key parameters, central pressure and steepness of the temperature gradient (Γ), which significantly influence the line formation in this event.

In our study, radial velocity is not an important parameter, which is different from Labrosse and McGlinchey (2012). This is because the radial velocity values in our study are quite large in comparison to Labrosse and McGlinchey (2012), which leads the incident photons at 304 Å to be out of resonance with the He II ions. To illustrate this effect more explicitly, we computed an additional set of 26 models in which all parameters were fixed to the median values of their

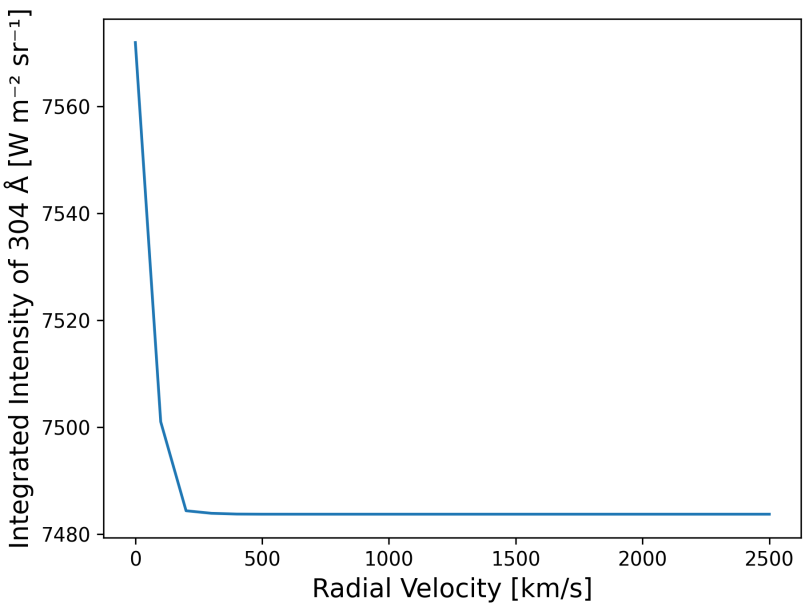

Figure 5.13: Integrated intensity of the He II 304 Å line as a function of radial velocity for 26 models. In this test, all model parameters were fixed to the median values of their adopted ranges, except for the radial velocity, which was varied from 0 to 2500 km s^{-1}. (Figure from Zhang et al. (2026d, submitted)).

adopted ranges, while the radial velocity alone was varied from 0 to 2500 km s^{-1}. The resulting integrated intensity of the 304 Å line is shown in Figure 5.13. The figure shows that the radial velocity has a clear effect at low velocities, mainly below about 250 km s^{-1}, where the integrated intensity decreases rapidly. At higher velocities, however, the intensity becomes nearly constant, indicating that the resonant scattering contribution has already been strongly reduced and that further increases in radial velocity produce only minor changes.

An additional limitation of the present interpretation is that the models assume statistical equilibrium and do not include non-equilibrium ionisation of helium. Golding et al. (2017) showed, using radiation-MHD modelling of the dynamic quiet-Sun atmosphere, that non-equilibrium helium ionisation is primarily responsible for the enhanced intensity of the He II 304 Å line. When the atmospheric conditions change on timescales shorter than the helium ionisation and recombination timescales, the ionisation state retains a memory of the previous thermal conditions. Consequently, He II may remain abundant and produce significant 304 Å emission in plasma at temperatures of the order of 10^4 K, and the concept of a equilibrium formation temperature near 10^5 K may no longer be appropriate.

Such non-equilibrium effects could modify the He II and He III populations, the line opacity, and the relative magnitudes of the collisional and radiative components derived from our equilibrium models.

The quantitative results of Golding et al. (2017) cannot be applied directly to the present event because their simulations describe the dynamic quiet Sun chromosphere rather than a high

altitude eruptive prominence. A rigorous assessment would require time dependent non-LTE radiative transfer modelling coupled to the thermal history and dynamics of the erupting plasma, which is beyond the scope of the present static model grid. The results here should therefore be interpreted as conditional on the statistical equilibrium assumption.

Mierla et al. (2022) conjecture that the 304 Å line in this eruptive prominence is due to collisional excitation rather than to resonant scattering. The high altitude of the prominence will indeed lead to a strong dilution of the incident radiation, and the large radial velocity limits the efficiency of resonant scattering of incident photons by He II ions due to the Doppler dimming effect. It is therefore reasonable to conclude that resonant scattering of the incident radiation cannot explain the emission observed.

However, our study shows that, in the source function, the collisional term is negligible and that radiative processes dominate the formation of the He II 304 Å line over the range of model parameters considered here to interpret EUI eruptive prominence observations. We conclude that the emission in the He II 304 Å line in this fast-moving, high-altitude eruptive prominence is radiatively controlled, namely via radiative recombination of He III followed by cascades populating the He II $n = 2$ state followed eventually by spontaneous emission in 304 Å. This is supported by the fact that at the high temperatures we have identified in the region of formation of the line (in the PCTR close to the prominence surface), helium is mostly fully ionised – there aren't enough He II ions in the ground state to be collisionally excited.

To further verify this, we examined the helium populations of reference models in different energy levels. All five reference models covering altitudes from 2.0 to 3.5 $R_\odot$, have nearly identical helium populations. The mean number densities through the slab are 3.67×10^7 cm^{-3}, 7.30×10^7 cm^{-3}, and 7.90×10^7 cm^{-3} for He I, He II, and He III, respectively, corresponding to 19%, 39%, and 42%. The population of the ground state He II ions in slab surface is 1.51×10^5 cm^{-3}, while the population of He III ions in slab surface is 7.67×10^7 cm^{-3}. This is consistent with our explanation.

5.4 Concluding Remarks

In this study, we analysed the eruption of a solar prominence observed by the EUI instrument aboard Solar Orbiter in the He II 304 Å line, focusing on various physical parameters such as temperature, radial velocity, and altitude. A filter-ratio analysis using the 171 Å and 195 Å channels of STEREO/EUVI-A allows us to constrain the temperature of the eruptive prominence around log T [K] = 5.20~5.40. We also constrain the radial velocity in the range 1180~2200 km s^{-1} by tracking different features in the eruption. By analysing various parameters and generating 200 random non-LTE PCTR models, we investigated how these parameters influence the formation of the He II 304 Å line.

We compared our results with Labrosse and McGlinchey (2012). We confirm that column

mass is an important factor in the formation of the He II 304 Å line. The effect of radial velocity is not visible in our study, which is due to the high radial velocity values we observed. Our results suggest that central pressure, column mass and the steepness of the temperature profile (Γ) are key factors affecting the He II 304 Å line's formation in this event, as indicated by their strong correlations with integrated intensity, radiative term and optical thickness. The study also revealed the impact of column mass and gamma on intensity variation with altitude during the eruption, which displays how physical conditions within the prominence change with altitude.

Our study also shows that at temperatures of a few 10^5 K, He II 304 Å emission in a high-altitude, outward-moving prominence is no longer produced by resonant scattering of solar radiation. As shown in Figure 5.13, the integrated intensity decreases rapidly as the radial velocity increases from 0 to approximately 250 km s^{-1}, but remains nearly constant at higher velocities. This behaviour indicates that, over the 500–2500 km s^{-1} range of radial velocity adopted in the main model grid, the incident 304 Å radiation has already been shifted largely out of resonance. Instead, it is produced predominantly by radiative recombination of He III followed by cascades into the $n = 2$ level. Radiative rates dominate over collisional destruction rates. Thus, the emission remains radiatively dominated, but the dominant radiative process has shifted from scattering of the incident radiation (in the case of low-lying, relatively quiescent or slowly moving prominences) to photoionisation followed by recombination. This is different from the conjecture in Mierla et al. (2022).

While this analysis provides significant insights into prominence dynamics and the He II 304 Å line's formation, it is limited by the lack of calibrated intensities. In future work, we will combine the work of chapter 2 (Zhang et al., 2026a), chapter 3 (Zhang et al., 2026b), chapter 4 (Zhang et al., 2026c, submitted)), and this chapter to analyse hydrogen and helium lines observed simultaneously in the same event, e.g. by SPICE and EUI.

Chapter 6

Conclusions

This thesis has presented a comprehensive investigation of solar prominences, combining observational analysis with non-LTE radiative transfer modelling to probe the physical conditions of plasma structures. Using data from the Solar Orbiter mission, particularly the SPICE spectrometer and EUI imager, supported by STEREO/EUVI and GONG Hα, we have analysed two distinct prominence events: a prominence observed on 15 April 2023 in the pre-eruptive and eruptive phases, and a fast-moving, high-altitude eruptive prominence observed on 15 February 2022. Through a combination of spectral line diagnostics, multi-parameter analyses, and model construction techniques, we have significantly advanced our understanding of the thermodynamic and dynamic properties of prominences and the mechanisms governing line formations.

Chapter 1 established the essential physical framework for the thesis. We reviewed the fundamental properties of solar prominences, including their thermodynamic parameters, magnetic field structure, and morphological classification, and described fine-scale structures and dynamical phenomena such as counterstreaming flows and oscillations. The chapter also provided a detailed overview of radiative transfer theory, introducing the statistical equilibrium equations and the importance of partial frequency redistribution. Finally, we introduced the key instrumentation used throughout the thesis: SPICE and EUI on Solar Orbiter, STEREO/EUVI, and the GONG Hα network. This introduction provides the necessary foundation for the observational and modelling work presented in subsequent chapters.

Chapter 2 presented the first dedicated off-limb prominence observation by SPICE on 15 April 2023, focusing on the Lyman β and Lyman γ lines. We analysed the integrated intensities, line widths, and line profiles during both the pre-eruptive and eruptive phases. The integrated intensity ratio of Lyman β to Lyman γ remained roughly constant at about 2.5 in both disc and prominence regions, indicating similar radiative transfer conditions and suggesting that both lines are formed primarily through resonance scattering of chromospheric radiation. During the eruption, the Lyman β integrated intensity in one prominence region increased substantially, occasionally exceeding the disc intensity, indicating enhanced heating, increased hydrogen density, or compression. Line width analysis using the quantile method revealed intrinsic widths

of 0.10 nm (Lyman β) and 0.16 nm (Lyman γ) in the pre-eruption prominence, similar to disc values, while during the eruption line widths narrowed significantly (intrinsic width $\sim$0.05 nm for Lyman β). We also developed a novel method to estimate radial velocities from 2D image sequences, using Hα and EUVI-A observations to derive an upper limit of $\sim$40 km s^{-1} for the radial velocity before 10:00 UT. This chapter demonstrated the diagnostic potential of SPICE Lyman lines for probing prominence plasma conditions while also highlighting the limitations of observational data alone in uniquely constraining physical parameters.

Chapter 3 extended the observational analysis by applying the 1D non-LTE radiative transfer code PRODOP to investigate how key plasma parameters control the formation of the Lyman β and Lyman γ lines in the pre-eruptive prominence observed on 15 April 2023. The incident radiation was constrained using a SPICE full-disc mosaic observation from November 2023, providing realistic boundary conditions. To analyse the complex multi-parameter relationships, we introduced parallel coordinate plots and elasticity coefficients. Parallel coordinate plots enabled efficient visualisation of how multiple parameters simultaneously affect line properties, allowing identification of dominant parameters and non-linear relationships without the need for many separate figures. Elasticity coefficients quantified the sensitivity of line properties to relative changes in each parameter. The analysis revealed that for both Lyman β and Lyman γ lines, the integrated intensity was most strongly influenced by central pressure, column mass, and the temperature gradient parameter γ. Higher central pressure and larger column mass increased integrated intensity, while steeper temperature gradients decreased it. The collisional and radiative terms in the source function were comparable, indicating that both processes are important for Lyman line formation in this pre-eruptive prominence. Optical thickness was primarily controlled by central temperature and column mass. By combining the observed integrated intensities with the modelling results, we constrained the central pressure of the prominence to be below 0.48 dyn, cm^{-2}, and the Lyman β and Lyman γ optical thicknesses to be below 4800 and 1000, respectively. This chapter bridged the observational analysis with physical interpretation, demonstrating how non-LTE modelling can help to constrain plasma parameters in observational data.

Chapter 4 developed a novel modelling approach to construct detailed parameter maps of the prominence from the Lyman β and Lyman γ observations. We devised a model-constructing tool that combined the diagnostic potential of both lines by generating 1000 random models, selecting the best matches for each line individually, and then modifying the temperature and pressure profiles using the contribution functions of each line to simultaneously achieve a good match for both lines. The method used linear combinations of the temperature and pressure profiles from the two best-matched models, with coefficients varied systematically to minimise the mean relative difference between synthetic and observed intensities. After optimisation, we achieved a mean relative difference of approximately 8% between the modelled and observed intensity maps, which is acceptable given the uncertainties inherent to observations and models.

The resulting parameter maps revealed the spatial distributions of column mass, mean pressure, and mean temperature across the prominence region. The column mass and pressure structures exhibited strong correspondence with the observed intensity morphology, implying that local variations in mass and pressure play dominant roles in shaping the radiative emission pattern. The mean temperature map showed less distinct structure, consistent with the lower sensitivity of Lyman lines to temperature compared to pressure and column mass. As an additional application, we generated synthetic maps of electron density and Hα intensity, demonstrating the potential of this technique to produce simulated observations of lines that were not directly measured.

Chapter 5 focused on the He II 304 Å line observed during the fast, high-altitude prominence eruption on 15 February 2022 by EUI/FSI. We used filter-ratio analysis with STEREO/EUVI-A 171 Å and 195 Å channels to constrain the temperature of the eruptive prominence to $\log T\ [\mathrm{K}] = 5.2$–$5.6$, and tracked features in the EUI images to determine radial velocities in the range 1180–2200 km s^{-1}. We generated 200 random non-LTE PCTR models with the PRODOP code, focusing on the formation of the He II 304 Å line. Parallel coordinate plots showed that the integrated intensity of the 304 Å line was primarily controlled by column mass and the temperature gradient parameter Γ, while the optical thickness was dominated by column mass. Critically, the collisional term in the source function showed no significant correlation with any parameter and remained very small, whereas the radiative term was strongly influenced by central pressure, column mass, and Γ. This indicates that radiative processes dominate the formation of the He II 304 Å line in this eruptive prominence, contrary to the conjecture in earlier work by Mierla et al. (2022) that collisional excitation might be dominant. We interpret this as emission from radiative recombination of He III followed by cascades populating the He II $n = 2$ level, rather than resonant scattering of incident radiation, which is suppressed by the high altitude (strong dilution) and large radial velocity (Doppler dimming) as shown in Figure 5.13. This conclusion resolves a key question regarding the formation mechanism of the 304 Å line in fast-moving, high-altitude prominences.

While this thesis has made significant progress in understanding solar prominences through multi-wavelength observations and non-LTE modelling, several avenues remain for future exploration. The approach of parameter maps construction in Chapter 4 can be extended to include additional spectral lines or line ratios, improving the sensitivity to specific physical parameters. Future work will optimise the selection of diagnostic lines to enhance spatial detail in parameter maps. This methodology will open a pathway towards comprehensive multi-line prominence diagnostics using SPICE, IRIS and future EUV spectroscopic datasets.

The parallel coordinate plot and elasticity coefficient framework introduced in this thesis proved powerful for visualising and quantifying multi-parameters relationships. This approach could be applied more broadly to other astrophysical plasmas where complex radiative transfer and multi-parameters are involved. The method provides an intuitive way to identify which

parameters most strongly influence observable quantities and how sensitive they are to the properties we study.

The discovery that He II 304 Å emission in fast-moving prominences is dominated by radiative recombination of He III followed by cascades populating the He II $n = 2$ level rather than resonant scattering has implications for interpreting future observations. While the analysis of the fast, high-altitude eruptive prominence provides significant insights into the prominence's dynamics and the He II 304 Å line's formation, it is limited by the lack of calibrated intensities. Future work should investigate whether this mechanism is general for high-speed eruption, and how it affects the diagnostics of the 304 Å passband.

The two prominence events studied in this thesis, a eruptive prominence with low radial velocity and a fast, high-altitude eruptive prominence, represent different cases. In a future work, we will combine the work of Zhang et al. (2026a), Zhang et al. (2026b), Zhang et al. (2026c, submitted) and Zhang et al. (2026d, submitted) to analyse hydrogen and helium lines observed simultaneously in the same event, e.g. by SPICE and EUI.

Bibliography

T Amari, JF Luciani, Z Mikic, and J Linker. A twisted flux rope model for coronal mass ejections and two-ribbon flares. *The Astrophysical Journal Letters*, 529(1):L49–L52, 2000.

Mark Anderson, T Appourchaux, Frédéric Auchère, R Aznar Cuadrado, J Barbay, F Baudin, S Beardsley, Karine Bocchialini, B Borgo, D Bruzzi, et al. The solar orbiter spice instrument-an extreme uv imaging spectrometer. *Astronomy & Astrophysics*, 642:A14, 2020.

SK Antiochos, CR DeVore, and JA Klimchuk. A model for solar coronal mass ejections. *The Astrophysical Journal*, 510(1):485–493, 1999.

Patrick Antolin, Frédéric Auchère, Ethan Winch, Elie Soubrié, and Ramón Oliver. Decomposing the aia 304 å channel into its cool and hot components. *Solar Physics*, 299(7):94, 2024.

U Anzer, P Heinzel, and F Fárnik. Prominences on the limb: Diagnostics with uv–euv lines and the soft x-ray continuum. *Solar Physics*, 242(1):43–52, 2007.

Ulrich Anzer and Peter Heinzel. The energy balance in solar prominences. *Astronomy and Astrophysics, v. 349, p. 974-984 (1999)*, 349:974–984, 1999.

D Banerjee, Robert Erdelyi, Ramon Oliver, and Eoghan O'Shea. Present and future observing trends in atmospheric magnetoseismology. *Solar Physics*, 246(1):3–29, 2007.

Krzysztof Barczynski, Brigitte Schmieder, Aaron W. Peat, Nicolas Labrosse, Pierre Mein, and Nicole Mein. Spectro-imagery of an active tornado-like prominence: Formation and evolution. *Astronomy & Astrophysics*, 653:A94, September 2021. doi: 10.1051/0004-6361/202140976.

Thomas E Berger, Richard A Shine, Gregory L Slater, Theodore D Tarbell, Alan M Title, Takenori J Okamoto, Kiyoshi Ichimoto, Yukio Katsukawa, Yoshinori Suematsu, Saku Tsuneta, et al. Hinode sot observations of solar quiescent prominence dynamics. *The Astrophysical Journal Letters*, 676(1):L89–L92, 2008.

Thomas E Berger, Gregory Slater, Neal Hurlburt, Richard Shine, Theodore Tarbell, Bruce W Lites, Takenori J Okamoto, Kiyoshi Ichimoto, Yukio Katsukawa, Tetsuya Magara, et al. Qui-

escent prominence dynamics observed with the hinode solar optical telescope. i. turbulent upflow plumes. *The Astrophysical Journal*, 716(2):1288, 2010.

Mats Carlsson and Robert F Stein. Formation of solar calcium h and k bright grains. *The Astrophysical Journal*, 481(1):500, 1997.

D Cirigliano, J-C Vial, and M Rovira. Prominence–corona transition region plasma diagnostics from soho observations. *Solar Physics*, 223(1):95–118, 2004.

W. Curdt, P. Brekke, U. Feldman, K. Wilhelm, B. N. Dwivedi, U. Schühle, and P. Lemaire. The SUMER spectral atlas of solar-disk features. *Astronomy & Astrophysics*, 375:591–613, August 2001. doi: 10.1051/0004-6361:20010833.

Cornelius De Jager. Structure and dynamics of the solar atmosphere. In *Astrophysics III: The Solar System/Astrophysik III: Das Sonnensystem*, pages 80–362. Springer, 2012.

G. Del Zanna, B. O'Dwyer, and H. E. Mason. SDO AIA and Hinode EIS observations of "warm" loops. *Astronomy & Astrophysics*, 535:A46, November 2011. doi: 10.1051/0004-6361/201117470.

P Démoulin and JC Vial. Structural characteristics of eruptive prominences. *Solar physics*, 141 (2):289–301, 1992.

Carsten Denker and Alexandra Tritschler. Mini-filaments-small-scale analogues of solar eruptive events? In *Cosmic Magnetic Fields: From Planets, to Stars and Galaxies*, volume 259, pages 223–224, 2009.

Jaroslav Dudík, Guillaume Aulanier, Brigitte Schmieder, M Zapiór, and Petr Heinzel. Magnetic topology of bubbles in quiescent prominences. *The Astrophysical Journal*, 761(1):9, 2012.

RP Dufresne, G Del Zanna, PR Young, KP Dere, E Deliporanidou, WT Barnes, and E Landi. Chianti—an atomic database for emission lines—paper. xviii. version 11, advanced ionization equilibrium models: density and charge transfer effects. *The Astrophysical Journal*, 974(1): 71, 2024.

H Ebadi, J-C Vial, and A Ajabshirizadeh. The he ii lines in the lyman series profiles of solar prominences. *Solar Physics*, 257(1):91–98, 2009.

Robert M Edsall. The parallel coordinate plot in action: design and use for geographic visualization. *Computational Statistics & Data Analysis*, 43(4):605–619, 2003.

Oddbjørn Engvold. Observational aspects of prominence oscillations. *Proceedings of the International Astronomical Union*, 3(S247):152–157, 2007.

Oddbjørn Engvold. Description and classification of prominences. In *Solar prominences*, pages 31–60. Springer, 2014.

Oddbjørn Engvold, Hans Jakobsson, Einar Tandberg-Hanssen, Joe B Gurman, and Daniel Moses. On the nature of prominence absorption and emission in highly ionized iron and in neutral hydrogen. *Solar Physics*, 202(2):293–308, 2001.

Andrzej Fludra, M Caldwell, A Giunta, T Grundy, Steven Guest, S Leeks, S Sidher, Frédéric Auchère, Mats Carlsson, D Hassler, et al. First observations from the spice euv spectrometer on solar orbiter. *Astronomy & Astrophysics*, 656:A38, 2021.

TG Forbes and PA Isenberg. A catastrophe mechanism for coronal mass ejections. *Astrophysical Journal, Part 1 (ISSN 0004-637X), vol. 373, May 20, 1991, p. 294-307.*, 373:294–307, 1991.

Peter Foukal. Morphological relationships in the chromospheric hα fine structure. *Solar Physics*, 19(1):59–71, 1971.

S. L. Freeland and B. N. Handy. Data Analysis with the SolarSoft System. *Solar Physics*, 182 (2):497–500, October 1998. doi: 10.1023/A:1005038224881.

J Fuller, SE Gibson, G De Toma, and Y Fan. Observing the unobservable? modeling coronal cavity densities. *The Astrophysical Journal*, 678(1):515, 2008.

V Gaizauskas. Filament channels: Essential ingredients for filament formation. In *International Astronomical Union Colloquium*, volume 167, pages 257–264. Cambridge University Press, 1998.

Yong Ge, Sanping Li, V Chris Lakhan, and Arko Lucieer. Exploring uncertainty in remotely sensed data with parallel coordinate plots. *International Journal of Applied Earth Observation and Geoinformation*, 11(6):413–422, 2009.

TP Golding, Jorrit Leenaarts, and M Carlsson. Formation of the helium extreme-uv resonance lines. *Astronomy & Astrophysics*, 597:A102, 2017.

L. Golub, E. DeLuca, G. Austin, J. Bookbinder, D. Caldwell, P. Cheimets, J. Cirtain, M. Cosmo, P. Reid, A. Sette, M. Weber, T. Sakao, R. Kano, K. Shibasaki, H. Hara, S. Tsuneta, K. Kumagai, T. Tamura, M. Shimojo, J. McCracken, J. Carpenter, H. Haight, R. Siler, E. Wright, J. Tucker, H. Rutledge, M. Barbera, G. Peres, and S. Varisco. The X-Ray Telescope (XRT) for the Hinode Mission. *Solar Physics*, 243(1):63–86, June 2007. doi: 10.1007/s11207-007-0182-1.

P. Gouttebroze and P. Heinzel. Calcium to hydrogen line ratios in solar prominences. *Astronomy & Astrophysics*, 385:273–280, April 2002. doi: 10.1051/0004-6361:20020142.

P Gouttebroze and N Labrosse. A ready-made code for the computation of prominence nlte models. *Solar Physics*, 196(2):349–355, 2000.

P. Gouttebroze and N. Labrosse. Radiative transfer in cylindrical threads with incident radiation. VI. A hydrogen plus helium system. *Astronomy & Astrophysics*, 503(3):663–671, September 2009. doi: 10.1051/0004-6361/200811483.

P Gouttebroze, P Heinzel, and JC Vial. The hydrogen spectrum of model prominences. *Astronomy and Astrophysics Supplement Series (ISSN 0365-0138), vol. 99, no. 3, p. 513-543.*, 99: 513–543, 1993.

Victor V Grechnev, Arkadiy M Uralov, Vasily G Zandanov, Nikolai Y Baranov, and Kiyoto Shibasaki. Observations of prominence eruptions with two radioheliographs, ssrt, and norh. *Publications of the Astronomical Society of Japan*, 58(1):69–84, 2006.

S. Gunár, P. Heinzel, U. Anzer, and B. Schmieder. On Lyman-line asymmetries in quiescent prominences. *Astronomy & Astrophysics*, 490:307–313, October 2008. doi: 10.1051/0004-6361:200809885.

S Gunár, P Schwartz, J Koza, and P Heinzel. Quiet-sun hydrogen lyman-α line profile derived from soho/sumer solar-disk observations. *Astronomy & Astrophysics*, 644:A109, 2020.

Stanislav Gunár, P Schwartz, Brigitte Schmieder, Petr Heinzel, and U Anzer. Statistical comparison of the observed and synthetic hydrogen lyman line profiles in solar prominences. *Astronomy & Astrophysics*, 514:A43, 2010.

S Rifai Habbal, Miloslav Druckmüller, Huw Morgan, Isabelle Scholl, Vojtech Rušin, Adrian Daw, Judd Johnson, and Martina Arndt. Total solar eclipse observations of hot prominence shrouds. *The Astrophysical Journal*, 719(2):1362, 2010.

George E Hale. The spectrohelioscope and its work. *Astrophysical Journal, vol. 70, p. 265*, 70: 265, 1929.

J. W. Harvey, F. Hill, R. P. Hubbard, J. R. Kennedy, J. W. Leibacher, J. A. Pintar, P. A. Gilman, R. W. Noyes, A. M. Title, J. Toomre, and et al. The global oscillation network group (GONG) project. *Science*, 272:1284–1286, May 1996. doi: 10.1126/science.272.5266.1284.

T. Hasegawa, C. Q. Noda, T. Shimizu, and M. Carlsson. On the Formation of Lyman β and the O i 1027 and 1028 Å Spectral Lines. *The Astrophysical Journal*, 900:34, August 2020. doi: 10.3847/1538-4357/aba434.

P Heinzel, P Gouttebroze, and J-C Vial. Theoretical correlations between prominence plasma parameters and the emitted radiation. *Astronomy and Astrophysics (ISSN 0004-6361), vol. 292, no. 2, p. 656-668*, 292:656–668, 1994.

P. Heinzel, B. Schmieder, J.-C. Vial, and P. Kotrč. SOHO/SUMER observations and analysis of the hydrogen Lyman spectrum in solar prominences. *Astronomy & Astrophysics*, 370: 281–297, May 2001. doi: 10.1051/0004-6361:20010219.

Petr Heinzel. Radiative transfer in solar prominences. In *Solar prominences*, pages 103–130. Springer, 2014.

Petr Heinzel. Radiative Transfer in Solar Prominences. In Jean-Claude Vial and Oddbjørn Engvold, editors, *Solar Prominences*, volume 415 of *Astrophysics and Space Science Library*, page 103, January 2015. doi: 10.1007/978-3-319-10416-4_5.

Petr Heinzel, Sonja Jejčič, Jiří Štěpán, Roberto Susino, Vincenzo Andretta, Giuliana Russano, Silvano Fineschi, Marco Romoli, Alessandro Bemporad, Arkadiusz Berlicki, et al. First metis detection of the helium d3 line polarization in a large eruptive prominence. *The Astrophysical Journal Letters*, 957(1):L10, 2023.

Tadashi Hirayama. Modern observations of solar prominences. *Solar physics*, 100(1):415–434, 1985.

R. A. Howard, J. D. Moses, A. Vourlidas, J. S. Newmark, D. G. Socker, S. P. Plunkett, C. M. Korendyke, J. W. Cook, A. Hurley, J. M. Davila, W. T. Thompson, O. C. St Cyr, E. Mentzell, K. Mehalick, J. R. Lemen, J. P. Wuelser, D. W. Duncan, T. D. Tarbell, C. J. Wolfson, A. Moore, R. A. Harrison, N. R. Waltham, J. Lang, C. J. Davis, C. J. Eyles, H. Mapson-Menard, G. M. Simnett, J. P. Halain, J. M. Defise, E. Mazy, P. Rochus, R. Mercier, M. F. Ravet, F. Delmotte, F. Auchere, J. P. Delaboudiniere, V. Bothmer, W. Deutsch, D. Wang, N. Rich, S. Cooper, V. Stephens, G. Maahs, R. Baugh, D. McMullin, and T. Carter. Sun Earth Connection Coronal and Heliospheric Investigation (SECCHI). *Space Science Reviews*, 136 (1-4):67–115, April 2008. doi: 10.1007/s11214-008-9341-4.

H Isobe, D Tripathi, A Asai, and R Jain. Large-amplitude oscillation of an erupting filament as seen in euv, hα, and microwave observations. *Solar Physics*, 246(1):89–99, 2007.

TJ Janssens. Long term observations of the hα chromospheric network. *Solar Physics*, 11(2): 222–242, 1970.

S Jejčič, P Heinzel, M Zapiór, M Druckmüller, S Gunár, and P Kotrč. Multi-wavelength eclipse observations of a quiescent prominence. *Solar Physics*, 289(7):2487–2501, 2014.

Sonja Jejčič, Petr Heinzel, Brigitte Schmieder, Stanislav Gunár, Pierre Mein, Nicole Mein, and Guiping Ruan. Non-lte inversion of prominence spectroscopic observations in hα and mg ii h&k lines. *The Astrophysical Journal*, 932(1):3, 2022.

Michael L Kaiser, TA Kucera, JM Davila, OC St Cyr, Madhulika Guhathakurta, and Eric Christian. The stereo mission: An introduction. *Space Science Reviews*, 136:5–16, 2008.

Graham Stewart Kerr, Paulo JA Simões, Jiong Qiu, and Lyndsay Fletcher. Iris observations of the mg ii h and k lines during a solar flare. *Astronomy & Astrophysics*, 582:A50, 2015.

T. Kosugi, K. Matsuzaki, T. Sakao, T. Shimizu, Y. Sone, S. Tachikawa, T. Hashimoto, K. Minesugi, A. Ohnishi, T. Yamada, S. Tsuneta, H. Hara, K. Ichimoto, Y. Suematsu, M. Shimojo, T. Watanabe, S. Shimada, J. M. Davis, L. D. Hill, J. K. Owens, A. M. Title, J. L. Culhane, L. K. Harra, G. A. Doschek, and L. Golub. The Hinode (Solar-B) Mission: An Overview. *Solar Physics*, 243(1):3–17, June 2007. doi: 10.1007/s11207-007-9014-6.

TA Kucera, SE Gibson, DJ Schmit, E Landi, and D Tripathi. Temperature and extreme-ultraviolet intensity in a coronal prominence cavity and streamer. *The Astrophysical Journal*, 757(1):73, 2012.

Terry A. Kucera. Derivations and Observations of Prominence Bulk Motions and Mass. In Jean-Claude Vial and Oddbjørn Engvold, editors, *Solar Prominences*, volume 415 of *Astrophysics and Space Science Library*, page 79, January 2015. doi: 10.1007/978-3-319-10416-4_4.

N. Labrosse and P. Gouttebroze. Formation of helium spectrum in solar quiescent prominences. *Astronomy & Astrophysics*, 380:323–340, December 2001. doi: 10.1051/0004-6361:20011395.

N. Labrosse and P. Gouttebroze. Non-LTE Radiative Transfer in Model Prominences. I. Integrated Intensities of He I Triplet Lines. *The Astrophysical Journal*, 617(1):614–622, December 2004. doi: 10.1086/425168.

N. Labrosse and K. McGlinchey. Plasma diagnostic in eruptive prominences from SDO/AIA observations at 304 Å. *Astronomy & Astrophysics*, 537:A100, January 2012. doi: 10.1051/0004-6361/201117801.

N. Labrosse and A. S. Rodger. Radiative transfer in cylindrical threads with incident radiation. VII. Multi-thread models. *Astronomy & Astrophysics*, 587:A113, March 2016. doi: 10.1051/0004-6361/201526897.

N. Labrosse, X. Li, and B. Li. On the Lyman α and β lines in solar coronal streamers. *Astronomy & Astrophysics*, 455(2):719–723, August 2006. doi: 10.1051/0004-6361:20065059.

N. Labrosse, P. Gouttebroze, and J.-C. Vial. Effect of motions in prominences on the helium resonance lines in the extreme ultraviolet. *Astronomy & Astrophysics*, 463:1171–1179, February 2007. doi: 10.1051/0004-6361:20066419.

N. Labrosse, J.-C. Vial, and P. Gouttebroze. Diagnostics of active and eruptive prominences through hydrogen and helium lines modelling. *Annales Geophysicae*, 26:2961–2965, October 2008. doi: 10.5194/angeo-26-2961-2008.

N. Labrosse, P. Heinzel, J. C. Vial, T. Kucera, S. Parenti, S. Gunár, B. Schmieder, and G. Kilper. Physics of Solar Prominences: I—Spectral Diagnostics and Non-LTE Modelling. *Space Science Reviews*, 151(4):243–332, April 2010. doi: 10.1007/s11214-010-9630-6.

N Labrosse, Petr Heinzel, J-C Vial, Therese Kucera, S Parenti, S Gunßr, Brigitte Schmieder, and G Kilper. Physics of solar prominences: I—spectral diagnostics and non-lte modelling. *Space Science Reviews*, 151(4):243–332, 2010.

N. Labrosse, B. Schmieder, P. Heinzel, and T. Watanabe. EUV lines observed with EIS/Hinode in a solar prominence. *Astronomy & Astrophysics*, 531:A69, July 2011. doi: 10.1051/0004-6361/201015064.

Nicolas Labrosse. Derivation of the Major Properties of Prominences Using NLTE Modelling. In Jean-Claude Vial and Oddbjørn Engvold, editors, *Solar Prominences*, volume 415 of *Astrophysics and Space Science Library*, page 131, January 2015. doi: 10.1007/978-3-319-10416-4_6.

Nicolas Labrosse, Andrew S Rodger, Krzysztof Radziszewski, Paweł Rudawy, Patrick Antolin, Lyndsay Fletcher, Peter J Levens, Aaron W Peat, Brigitte Schmieder, and Paulo JA Simoes. First high resolution interferometric observation of a solar prominence with alma. *Monthly Notices of the Royal Astronomical Society: Letters*, 513(1):L30–L34, 2022.

P Lemaire, J-C Vial, W Curdt, U Schühle, and TN Woods. The solar hydrogen lyman α to lyman β line ratio. *Astronomy & Astrophysics*, 542:L25, 2012.

James R. Lemen, Alan M. Title, David J. Akin, Paul F. Boerner, Catherine Chou, Jerry F. Drake, Dexter W. Duncan, Christopher G. Edwards, Frank M. Friedlaender, Gary F. Heyman, Neal E. Hurlburt, Noah L. Katz, Gary D. Kushner, Michael Levay, Russell W. Lindgren, Dnyanesh P. Mathur, Edward L. McFeaters, Sarah Mitchell, Roger A. Rehse, Carolus J. Schrijver, Larry A. Springer, Robert A. Stern, Theodore D. Tarbell, Jean-Pierre Wuelser, C. Jacob Wolfson, Carl Yanari, Jay A. Bookbinder, Peter N. Cheimets, David Caldwell, Edward E. Deluca, Richard Gates, Leon Golub, Sang Park, William A. Podgorski, Rock I. Bush, Philip H. Scherrer, Mark A. Gummin, Peter Smith, Gary Auker, Paul Jerram, Peter Pool, Regina Soufli, David L. Windt, Sarah Beardsley, Matthew Clapp, James Lang, and Nicholas Waltham. The Atmospheric Imaging Assembly (AIA) on the Solar Dynamics Observatory (SDO). *Solar Physics*, 275(1-2):17–40, January 2012. doi: 10.1007/s11207-011-9776-8.

JL Leroy. Observation of prominence magnetic fields. In *Dynamics and structure of quiescent solar prominences*, pages 77–113. Springer, 1989.

P. J. Levens and N. Labrosse. Modelling of Mg II lines in solar prominences. *Astronomy & Astrophysics*, 625:A30, May 2019. doi: 10.1051/0004-6361/201833132.

Y Lin, SF Martin, and O Engvold. Filament substructures and their interrelation. In *Subsurface and Atmospheric Influences on Solar Activity*, volume 383, page 235, 2008.

Yong Lin. Filament thread-like structures and their small-amplitude oscillations. *Space science reviews*, 158(2):237–266, 2011.

Yong Lin, OddbjØ rn Engvold, and Jun Elin Wiik. Counterstreaming in a large polar crown filament. *Solar Physics*, 216(1):109–120, 2003.

Jiajia Liu, Zhenjun Zhou, Yuming Wang, Rui Liu, Bin Wang, Chijian Liao, Chenglong Shen, Huinan Zheng, Bin Miao, Zhenpeng Su, et al. Slow magnetoacoustic waves observed above a quiet-sun region in a dark cavity. *The Astrophysical Journal Letters*, 758(2):L26, 2012a.

Q. Liu, C. Jiang, X. Feng, P. Zuo, and Y. Wang. Why are non-radial solar eruptions less frequent than radial ones? *Monthly Notices of the Royal Astronomical Society*, 533:L25, May 2024. doi: 10.1093/mnrasl/slae020.

Wei Liu, Thomas E Berger, and BC Low. First sdo/aia observation of solar prominence formation following an eruption: Magnetic dips and sustained condensation and drainage. *The Astrophysical Journal Letters*, 745(2):L21, 2012b.

William JS Lockyer. On the relationship between solar prominences and the forms of the corona. *Monthly Notices of the Royal Astronomical Society, Vol. 91, p. 797*, 91:797, 1931.

Duncan H Mackay, Victor Gaizauskas, and Anthony R Yeates. Where do solar filaments form?: Consequences for theoretical models. *Solar Physics*, 248(1):51–65, 2008.

Duncan Hendry Mackay, JT Karpen, Jose-Luis Ballester, Brigitte Schmieder, and Guillaume Aulanier. Physics of solar prominences: II—magnetic structure and dynamics. *Space Science Reviews*, 151(4):333–399, 2010.

John T Mariska, GA Doschek, and U Feldman. Extreme-ultraviolet limb spectra of a prominence observed from skylab. *Astrophysical Journal, Part 1, vol. 232, Sept. 15, 1979, p. 929-939.*, 232:929–939, 1979.

Sara F Martin. Filament chirality: A link between fine-scale and global patterns. In *International Astronomical Union Colloquium*, volume 167, pages 419–429. Cambridge University Press, 1998.

SF Martin, Y Lin, and O Engvold. A method of resolving the 180-degree ambiguity by employing the chirality of solar features. *Solar Physics*, 250(1):31–51, 2008.

P. I. McCauley, Y. N. Su, N. Schanche, K. E. Evans, C. Su, S. McKillop, and K. K. Reeves. Prominence and filament eruptions observed by the Solar Dynamics Observatory: Statistical

properties, kinematics, and online catalog. *Solar Physics*, 290:1703–1740, August 2015. doi: 10.1007/s11207-015-0699-7.

Donald Howard Menzel and John Wainwright Evans. *The behavior and classification of solar prominences*. Solar Department of Harvard College Observatory, Harvard Univ., 1953.

M. Mierla, A. N. Zhukov, D. Berghmans, S. Parenti, F. Auchère, P. Heinzel, D. B. Seaton, E. Palmerio, S. Jejčič, J. Janssens, E. Kraaikamp, B. Nicula, D. M. Long, L. A. Hayes, I. C. Jebaraj, D. C. Talpeanu, E. D'Huys, L. Dolla, S. Gissot, J. Magdalenić, L. Rodriguez, S. Shestov, K. Stegen, C. Verbeeck, C. Sasso, M. Romoli, and V. Andretta. Prominence eruption observed in He II 304 Å up to >6 $R_\odot$ by EUI/FSI aboard Solar Orbiter. *Astronomy & Astrophysics*, 662:L5, June 2022. doi: 10.1051/0004-6361/202244020.

R Molowny-Horas, E Wiehr, H Balthasar, R Oliver, and JL Ballester. Prominence doppler oscillations. *JOSO Annu. Rep., 1998*, pages 126–127, 1999.

Ronald L Moore, Alphonse C Sterling, Hugh S Hudson, and James R Lemen. Onset of the magnetic explosion in solar flares and coronal mass ejections. *The Astrophysical Journal*, 552(2):833–848, 2001.

Sargam M. Mulay, Giulio Del Zanna, and Helen Mason. Cool and hot emission in a recurring active region jet. *Astronomy & Astrophysics*, 606:A4, September 2017. doi: 10.1051/0004-6361/201730429.

D. Müller, O. C. St. Cyr, I. Zouganelis, H. R. Gilbert, R. Marsden, T. Nieves-Chinchilla, E. Antonucci, F. Auchère, D. Berghmans, T. S. Horbury, R. A. Howard, S. Krucker, M. Maksimovic, C. J. Owen, P. Rochus, J. Rodriguez-Pacheco, M. Romoli, S. K. Solanki, R. Bruno, M. Carlsson, A. Fludra, L. Harra, D. M. Hassler, S. Livi, P. Louarn, H. Peter, U. Schühle, L. Teriaca, J. C. del Toro Iniesta, R. F. Wimmer-Schweingruber, E. Marsch, M. Velli, A. De Groof, A. Walsh, and D. Williams. The Solar Orbiter mission. Science overview. *Astronomy & Astrophysics*, 642:A1, October 2020. doi: 10.1051/0004-6361/202038467.

Takenori J Okamoto, Saku Tsuneta, and Thomas E Berger. A rising cool column as a signature of helical flux emergence and formation of prominence and coronal cavity. *The Astrophysical Journal*, 719(1):583, 2010.

Ramón Oliver and José Luis Ballester. Oscillations in quiescent solar prominences observations and theory–(invited review). *Solar Physics*, 206(1):45–67, 2002.

Olga Panasenco, Sara F Martin, and Marco Velli. Apparent solar tornado-like prominences. *Solar Physics*, 289(2):603–622, 2014.

S Parenti and J-C Vial. Prominence and quiet-sun plasma parameters derived from fuv spectral emission. *Astronomy & Astrophysics*, 469(3):1109–1115, 2007.

S Parenti, J-C Vial, and P Lemaire. Prominence atlas in the sumer range 800–1250 å: I. observations, data reduction and preliminary results. *Solar Physics*, 220(1):61–80, 2004.

S Parenti, J-C Vial, and P Lemaire. Prominence atlas in the sumer range 800–1250 å-ii. line profile properties and ions identifications. *Astronomy & Astrophysics*, 443(2):679–684, 2005.

Susanna Parenti. Solar prominences: observations. *Living Reviews in Solar Physics*, 11(1):1, 2014a.

Susanna Parenti. Spectral diagnostics of cool prominence and pctr optically thin plasmas. In *Solar Prominences*, pages 61–77. Springer, 2014b.

Susanna Parenti, Brigitte Schmieder, Petr Heinzel, and Leon Golub. On the nature of prominence emission observed by sdo/aia. *The Astrophysical Journal*, 754(1):66, 2012.

Aaron W. Peat, Christopher M. J. Osborne, and Petr Heinzel. Doppler dimming and brightening effects in solar prominences. *Monthly Notices of the Royal Astronomical Society: Letters*, 533(1):L19–L24, 2024. doi: 10.1093/mnrasl/slae055.

Edison Pettit. Characteristic features of solar prominences. *Astrophysical Journal, vol. 76, p. 9*, 76:9, 1932.

JE Plowman, DM Hassler, F Auchère, R Aznar Cuadrado, A Fludra, S Mandal, and H Peter. Spice point spread function correction: General framework and capability demonstration. *Astronomy & Astrophysics*, 678:A52, 2023.

JE Plowman, DM Hassler, ME Molnar, AK Shrivastav, T Varesano, F Auchère, A Fludra, TA Kucera, TJ Wang, and Y Zhu. A new method of deriving doppler velocities for solar orbiter spice. *arXiv preprint arXiv:2508.09121*, 2025.

P. Rochus, F. Auchère, D. Berghmans, L. Harra, W. Schmutz, U. Schühle, P. Addison, T. Appourchaux, R. Aznar Cuadrado, D. Baker, J. Barbay, D. Bates, A. BenMoussa, M. Bergmann, C. Beurthe, B. Borgo, K. Bonte, M. Bouzit, L. Bradley, V. Büchel, E. Buchlin, J. Büchner, F. Cabé, L. Cadiergues, M. Chaigneau, B. Chares, C. Choque Cortez, P. Coker, M. Condamin, S. Coumar, W. Curdt, J. Cutler, D. Davies, G. Davison, J. M. Defise, G. Del Zanna, F. Delmotte, V. Delouille, L. Dolla, C. Dumesnil, F. Dürig, R. Enge, S. François, J. J. Fourmond, J. M. Gillis, B. Giordanengo, S. Gissot, L. M. Green, N. Guerreiro, A. Guilbaud, M. Gyo, M. Haberreiter, A. Hafiz, M. Hailey, J. P. Halain, J. Hansotte, C. Hecquet, K. Heerlein, M. L. Hellin, S. Hemsley, A. Hermans, V. Hervier, J. F. Hochedez, Y. Houbrechts, K. Ihsan, L. Jacques, A. Jérôme, J. Jones, M. Kahle, T. Kennedy, M. Klaproth, M. Kolleck, S. Koller, E. Kotsialos, E. Kraaikamp, P. Langer, A. Lawrenson, J. C. Le Clech', C. Lenaerts, S. Liebecq, D. Linder, D. M. Long, B. Mampaey, D. Markiewicz-Innes, B. Marquet, E. Marsch, S. Matthews, E. Mazy, A. Mazzoli, S. Meining, E. Meltchakov, R. Mercier,

S. Meyer, M. Monecke, F. Monfort, G. Morinaud, F. Moron, L. Mountney, R. Müller, B. Nicula, S. Parenti, H. Peter, D. Pfiffner, A. Philippon, I. Phillips, J. Y. Plesseria, E. Pylyser, F. Rabecki, M. F. Ravet-Krill, J. Rebellato, E. Renotte, L. Rodriguez, S. Roose, J. Rosin, L. Rossi, P. Roth, F. Rouesnel, M. Roulliay, A. Rousseau, K. Ruane, J. Scanlan, P. Schlatter, D. B. Seaton, K. Silliman, S. Smit, P. J. Smith, S. K. Solanki, M. Spescha, A. Spencer, K. Stegen, Y. Stockman, N. Szwec, C. Tamiatto, J. Tandy, L. Teriaca, C. Theobald, I. Tychon, L. van Driel-Gesztelyi, C. Verbeeck, J. C. Vial, S. Werner, M. J. West, D. Westwood, T. Wiegelmann, G. Willis, B. Winter, A. Zerr, X. Zhang, and A. N. Zhukov. The Solar Orbiter EUI instrument: The Extreme Ultraviolet Imager. *Astronomy & Astrophysics*, 642:A8, October 2020. doi: 10.1051/0004-6361/201936663.

Guiping Ruan, Brigitte Schmieder, Pierre Mein, Nicole Mein, Nicolas Labrosse, Stanislav Gunar, and Yao Chen. On the dynamic nature of a quiescent prominence observed by iris and msdp spectrographs. *The Astrophysical Journal*, 865(2):123, 2018.

S Sahal-Bréchot, M Malinovsky, and V Bommier. The polarization of the o vi 1032 a line as a probe for measuring the coronal vector magnetic field via the hanle effect. *Astronomy and Astrophysics (ISSN 0004-6361), vol. 168, no. 1-2, Nov. 1986, p. 284-300.*, 168:284–300, 1986.

Jonathan Luke Schiralli. A comparison of solar prominence data between H alpha and EUV (He II-304 Angstrom). Master's thesis, University of North Dakota, May 2014.

Carolus J Schrijver. Catastrophic cooling and high-speed downflow in quiescent solar coronal loops observed with trace. *Solar Physics*, 198(2):325–345, 2001.

Pavol Schwartz, Stanislav Gunar, and Werner Curdt. Non-lte modelling of prominence fine structures using hydrogen lyman-line profiles. *Astronomy & Astrophysics*, 577:A92, 2015.

Sara F Smith. The formation, structure and changes in filaments in active regions. In *Symposium-International Astronomical Union*, volume 35, pages 267–279. Cambridge University Press, 1968.

SPICE Consortium, M. Anderson, T. Appourchaux, F. Auchère, R. Aznar Cuadrado, J. Barbay, F. Baudin, S. Beardsley, K. Bocchialini, B. Borgo, D. Bruzzi, E. Buchlin, G. Burton, V. Büchel, M. Caldwell, S. Caminade, M. Carlsson, W. Curdt, J. Davenne, J. Davila, C. E. Deforest, G. Del Zanna, D. Drummond, J. Dubau, C. Dumesnil, G. Dunn, P. Eccleston, A. Fludra, T. Fredvik, A. Gabriel, A. Giunta, A. Gottwald, D. Griffin, T. Grundy, S. Guest, M. Gyo, M. Haberreiter, V. Hansteen, R. Harrison, D. M. Hassler, S. V. H. Haugan, C. Howe, M. Janvier, R. Klein, S. Koller, T. A. Kucera, D. Kouliche, E. Marsch, A. Marshall, G. Marshall, S. A. Matthews, C. McQuirk, S. Meining, C. Mercier, N. Morris, T. Morse, G. Munro, S. Parenti, C. Pastor-Santos, H. Peter, D. Pfiffner, P. Phelan, A. Philippon, A. Richards, K. Rogers,

C. Sawyer, P. Schlatter, W. Schmutz, U. Schühle, B. Shaughnessy, S. Sidher, S. K. Solanki, R. Speight, M. Spescha, N. Szwec, C. Tamiatto, L. Teriaca, W. Thompson, I. Tosh, S. Tustain, J. C. Vial, B. Walls, N. Waltham, R. Wimmer-Schweingruber, S. Woodward, P. Young, A. de Groof, A. Pacros, D. Williams, and D. Müller. The Solar Orbiter SPICE instrument. An extreme UV imaging spectrometer. *Astronomy & Astrophysics*, 642:A14, October 2020. doi: 10.1051/0004-6361/201935574.

G. Stellmacher and E. Wiehr. On the origin of the Balmer and Lyman emission lines in solar prominences. *Astronomy & Astrophysics*, 489:773–776, September 2008. doi: 10.1051/0004-6361:200810030.

Goetz Stellmacher and Eberhard Wiehr. The na i and sr ii resonance lines in solar prominences. *Solar Physics*, 292(7):83, 2017.

Alphonse C Sterling and Ronald L Moore. Evidence for gradual external reconnection before explosive eruption of a solar filament. *The Astrophysical Journal*, 602(2):1024–1036, 2004.

Yingna Su. *Magnetic shear in two-ribbon solar flares*. PhD thesis, Purple Mountain Observatory Nanjing, 2007.

ROBERTO Susino, Alessandro Bemporad, P Heinzel, S Jejcic, U Anzer, and E Dzifcáková. Determination of the physical properties of an erupting prominence from soho/lasco and uvcs observations. *IL NUOVO CIMENTO*, 100(37):42, 2019.

Frances Tang. Quiescent prominences-where are they formed? *Solar physics*, 107(2):233–237, 1987.

H. Tian, W. Curdt, E. Marsch, and U. Schühle. Hydrogen Lyman-α and Lyman-β spectral radiance profiles in the quiet Sun. *Astronomy & Astrophysics*, 504:239–248, September 2009. doi: 10.1051/0004-6361/200912374.

A. M. Uralov, V. V. Grechnev, and H. S. Hudson. Initial localization and kinematic characteristics of the structural components of a coronal mass ejection. *Journal of Geophysical Research (Space Physics)*, 110(A5):A05104, May 2005. doi: 10.1029/2004JA010951.

AM Uralov, SV Lesovoi, VG Zandanov, and VV Grechnev. Dual-filament initiation of a coronal mass ejection: Observations and model. *Solar Physics*, 208(1):69–90, 2002.

AM Uralov, VV Grechnev, and HS Hudson. Initial localization and kinematic characteristics of the structural components of a coronal mass ejection. *Journal of Geophysical Research: Space Physics*, 110(A5), 2005.

J. E. Vernazza, E. H. Avrett, and R. Loeser. Structure of the solar chromosphere. III-Models of the EUV brightness components of the quiet-sun. *The Astrophysical Journal Supplement Series*, 45:635–725, April 1981. doi: 10.1086/190731.

J-C Vial, H Ebadi, and A Ajabshirizadeh. The ly α and ly β profiles in solar prominences and prominence fine structure. *Solar Physics*, 246:327–338, 2007.

JC Vial. Optically thick lines in a quiescent prominence-profiles of lyman-alpha, lyman-beta/hi/, k and h/mg ii/, and k and h/ca ii/lines with the oso 8 lpsp instrument. *Astrophysical Journal, Part 1, vol. 253, Feb. 1, 1982, p. 330-352. Research supported by the Centre National d'Etudes Spatiales.*, 253:330–352, 1982.

Jean-Claude Vial. Historical background and introduction. In *Solar Prominences*, pages 1–29. Springer, 2014.

Jean-Claude Vial and Oddbjørn Engvold, editors. *Solar Prominences*, volume 415 of *Astrophysics and Space Science Library*, January 2015. doi: 10.1007/978-3-319-10416-4.

Zdeněk. Švestka. Varieties of Coronal Mass Ejections and Their Relation to Flares. *Space Science Reviews*, 95:135–146, January 2001. doi: 10.1023/A:1005225208925.

Haimin Wang, Jongchul Chae, Joseph B. Gurman, and Therese A. Kucera. Comparison of Prominences in Hα and He II 304 Å. *Solar Physics*, 183(1):91–96, November 1998. doi: 10.1023/A:1005010504873.

H. P. Warren, J. T. Mariska, and K. Wilhelm. High-resolution observations of the solar hydrogen Lyman lines in the quiet sun with the SUMER instrument on SOHO. *The Astrophysical Journal Supplement Series*, 119:105, September 1998. doi: 10.1086/313155.

KG Widing, U Feldman, and AK Bhatia. The extreme-ultraviolet spectrum (300-630 a) of an erupting prominence observed from skylab. *Astrophysical Journal, Part 1 (ISSN 0004-637X), vol. 308, Sept. 15, 1986, p. 982-992. NASA-supported research.*, 308:982–992, 1986.

E Wiehr, G Stellmacher, and M Bianda. The electron density in a quiescent prominence. *Central European Astrophysical Bulletin*, 40:79–85, 2016.

Jean-Pierre Wuelser, James R Lemen, Theodore D Tarbell, C Jacob Wolfson, Joseph C Cannon, Brock A Carpenter, Dexter W Duncan, Glenn S Gradwohl, Syndie B Meyer, Augustus S Moore, et al. Euvi: the stereo-secchi extreme ultraviolet imager. In *Telescopes and instrumentation for solar astrophysics*, volume 5171, pages 111–122. SPIE, 2004.

Chun Xia, PF Chen, Rony Keppens, and Allard Jan van Marle. Formation of solar filaments by steady and nonsteady chromospheric heating. *The Astrophysical Journal*, 737(1):27, 2011.

Peter R Young, Andrew R Inglis, Graham S Kerr, Therese A Kucera, and Daniel F Ryan. Fe xviii and fe xx forbidden lines observed by solar orbiter/spice. *The Astrophysical Journal*, 986(1):64, 2025.

J. Zhang, K. P. Dere, R. A. Howard, M. R. Kundu, and S. M. White. On the Temporal Relationship between Coronal Mass Ejections and Flares. *The Astrophysical Journal*, 559:452, September 2001. doi: 10.1086/322405.

P. Zhang. Prominences and their eruptions as observed with the IRIS mission and ancillary instruments. *Ph.D. Thesis*, 2019.

Yong Zhang, Nicolas Labrosse, Susanna Parenti, and Therese A. Kucera. Analysis of Lyman β and Lyman γ lines in a pre-eruptive and eruptive prominence with Solar Orbiter SPICE observations. *Monthly Notices of the Royal Astronomical Society*, 546(3):stag104, March 2026a. doi: 10.1093/mnras/stag104.

Yong Zhang, Nicolas Labrosse, Susanna Parenti, and Therese A. Kucera. Non-LTE analysis of pre-eruptive prominence plasma parameters' effects on the Lyman β and Lyman γ lines with Solar Orbiter SPICE observations. *Monthly Notices of the Royal Astronomical Society*, 546 (4):stag222, March 2026b. doi: 10.1093/mnras/stag222.

H Zirin. The solar atmosphere (waltham. *Mass.: Blaisdell Publishing*, 1966.

H Zirin. Astrophysics ofthe sun. *Cambridge Univ. 1OOO˜-2*, 1988.

JB Zirker, O Engvold, and SF Martin. Counter-streaming gas flows in solar prominences as evidence for vertical magnetic fields. *Nature*, 396(6710):440–441, 1998.